Sergio Yesid Gómez González

PROCESSING AND CHARACTERIZATION OF OXYGEN ELECTRODE AND ELECTROLYTE IN REVERSIBLE SOLID OXIDE FUEL CELLS

Thesis presented to the Graduate Program in Materials Science and Engineering of the Federal University of Santa Catarina, as a requirement for obtaining the PhD title in Materials Science and Engineering

Advisors
Dachamir Hotza/UFSC
Kjell Wiik/NTNU

Florianópolis
2015

González, Sergio
PROCESSING AND CHARACTERIZATION OF OXYGEN ELECTRODE AND ELECTROLYTE IN REVERSIBLE SOLID OXIDE FUEL CELLS/
Sergio González ; orientador, Dachamir Hotza ; coorientador, Kjell Wiik. - Florianópolis, SC, 2015.
134 p.
Tese (doutorado) - Universidade Federal de Santa
Catarina, Centro Tecnológico. Programa de Pós-Graduação em Ciência e Engenharia de Materiais.

Inclui referências

1. Ciência e Engenharia de Materiais. 2. Células de óxido sólido reversíveis . 3. Síntese de materiais para aplicação em célular e membranas . 4. Modelagem e estudo de sinterização . I. Hotza, Dachamir. II. Wiik, Kjell. III. Universidade Federal de Santa Catarina. Programa de PósGraduação em Ciência e Engenharia de Materiais. IV. Título.

Sergio Yesid Gómez González

PROCESSING AND CHARACTERIZATION OF OXYGEN ELECTRODE AND ELECTROLYTE IN REVERSIBLE SOLID OXIDE FUEL CELLS

This thesis was presented to obtain the Title of PhD in Materials Science and Engineering, and approved in its final version by the Graduate Program in Materials Science and Engineering of the Federal University of Santa Catarina

Florianópolis, March 2015.

_____
Prof. Antônio Pedro Novaes de Oliveira, Dr.
Program Dean

Examiners:

_____
Prof. Dachamir Hotza, Dr.
Advisor
Federal University of Santa Catarina

_____
Prof. Aloisio Nelmo Klein, Dr.
Federal University of Santa Catarina

_____
Prof. Carlos Renato Rambo, Dr.
Federal University of Santa Catarina

_____
Daniel Enrique Garcia, Dr.
Federal University of Santa Catarina

_____
Prof. Jairo Arturo Escobar, Dr.
Los Andes University

_____
Hansu Birol, Dr.
CSEM Brasil

To my parents,
family and soulmate

ACKNOWLEDGMENTS

My biggest and sincere thanks to:

First and foremost, my main supervisor, Professor Dachamir Hotza. His knowledge, enthusiasm and feedback have been vital for this work, mainly for his endless dedication. I could truly not have asked for a better supervisor. He gave me freedom to work independently, yet always knew when to give me a push in the right direction.

My supervisor in Norway, Professor Kjell Wiik, for welcoming me to visit his research group for one year at the Norwegian University of Science and Technology. His vast knowledge in electroceramics and interest in my work was greatly appreciated, I am grateful for the excellent guidance I received through our weekly meetings during my stay, his advice, feedback and comments during the writing process were invaluable.

The research council of Norway, CNPQ and CAPES for funding this project.

The inorganic and ceramic materials group at NTNU and the ceramic materials group at UFSC, especially to the Professor Tor Grande, Dr. Vegar Øygarden, Dr. Ørjan Fossmark Lohne, and Dr. Jonas Gurauskis. I learnt a lot from their contributions and discussions.

My previous advisors at Los Andes University, Professor Jairo Escobar and Oscar Alvarez, which gave to me the research start-guidelines and opened the first of so many doors.

The examiners: Prof. Klein, Prof. Rambo, Prof. Escobar, Dr. García and Dr. Birol, for the comments and suggestions to improve my work.

My parents Benjamin Gómez and Gladys González, for their help, support, care, encouragement and example.

My closest friends during my doctoral studies: Alejandro, Cato, Dan, Jaime, Juan, Julian, Mariana, Nicolas, Renzo, Sara, Tatiana, and Veronica, for the shared moments and support, but mainly for their good humor.

My dear Karina. Because every day with her is special and brings out the best in me!

Last but not least, to God…

“Student: Dr. Einstein, aren't these the same questions as last year's [physics] final exam?

Dr. Einstein: Yes, but this year the answers are different.”

(Albert Einstein)

RESUMO

As células a combustível de óxido sólido (SOFC) são células para conversão de hidrogênio em energia elétrica, altamente eficientes e limpas, já que produzem eletricidade, calor, e unicamente agua como gás de exhaustão do processo eletroquímico. A célula eletrolítica de óxido sólido (SOEC) corresponde à operação inversa da SOFC. Células a combustível de óxido sólido reversíveis (RSOFC) são dispositivos para produzir energia e armazená-la empregando hidrogênio como portador da energia, atuando de forma reversível como células combustível ou eletrolisador. Um breve análise econômico mostra RSOFC como una alternativa viável para sistemas híbridos de energias renováveis. O estado-da-arte dos materiais dos componentes da célula foi analisado e discutido em detalhe, comparando pontos comuns desenvolvidos neste trabalho. Materiais como Perovskitas, fases Ruddlesden-Popper e Perovskitas Duplas mostram-se como potencialmente mais eficientes em comparação com o material mais utilizado para eletrodos de oxigênio, manganita de estrôncio lantânio (LSM). Uma microestrutura nanocristalina pode melhorar propriedades chave, por exemplo para o eletrólito mais utilizado, zircônia estabilizada com yttria (YSZ), pode-se obter um aumento do >95% em condutividade iônica comparando tamanhos de grão de 300 nm e 2.15 μm. Para atingir as estructuras nanocristalinas, devem-se usar pós com tamanhos de partícula pequenos e técnicas de sinterização que inibam o crescimento de grão.

Fases Ruddlesden-Popper como as baseadas em $La_2NiO_{4+\delta}$, apresentam alta permeabilidade ao oxigênio, e condutividade iônica entre outras propriedades vantajosas para RSOFC. Neste trabalho é reportada a síntese e as propriedades de transporte de oxigênio para um material novo ($La_{2-y}Sr_yNi_{1-x}Mo_xO_{4+\delta}$, $0.0 \leq y \leq 0.4$ e $0.0 \leq x \leq 0.1$). A análise das fases revelou um limite de solubilidade baixo de Mo no sítio B da estrutura $A_2BO_{4+\delta}$. O material $La_{1.8}Sr_{0.2}Ni_{0.95}Mo_{0.05}O_{4+\delta}$ (LSMN) fase pura foi sintetizado com sucesso. Amostras de LSMN foram conformadas por compressão isostática e sinterizadas a 1500ºC durante 4 h. As densidades atingidas foram maiores do que 95% e o tamanho de grão foi de 14±8 μm. Um modelo simples de defeitos foi usado para explicar o comportamento da condutividade elétrica. O coeficiente de superfície (k_{chem}) e os coeficientes de difusão (D_{chem}) em termos de temperatura e PO_2 foram avaliados por relaxamento da condutividade elétrica (ECR) e comparados a materiais semelhantes, mostrando que dopagem no sitio B

de $La_2NiO_{4+\delta}$ com Mo, pode melhorar as propriedades de transporte de oxigênio.
Para melhorar a condutividade iônica, e desejável manufaturar o eletrólito com pós de pequeno tamanho e planejar a sinterização com os perfis de tempo-temperatura, para obter microestruturas com tamanhos de grão menores. Há falta de modelos que possam prever as densidades atingidas durante sinterização. Neste trabalho foi desenvolvido um modelo para predizer a densificação, como função da temperatura, tempo e tamanho de partícula. O modelo foi capaz de predizer densidades atingidas em diferentes condições de sinterização. A sinterização acarreta densificação e crescimento de tamanho de grão simultaneamente, particularmente para materiais nanocristalinos. Atualmente, métodos como spark plasma sintering (SPS), prensagem a quente (HP), sinterização em duas etapas (TSS) e queima rápida (FF) são empregados para inibir o crescimento de grão enquanto é mantida alta densificação. Neste trabalho, foi comparado experimentalmente FF e sinterização convencional (RH), em compactos de yttria estabilizada com zircônia (3YSZ e 8YSZ). Foram feitos experimentos em um forno tubular com taxas de aquecimento de ~500 °C/min (FF) e 10ºC/min (RH), analisando a mudança contínua da densidade dos compactos e a distribuição de tamanhos de grão da estrutura densa. As amostras sinterizadas pela rota convencional apresentam maior crescimento de grão por um fator de ~4 e ~2 respeito do tamanho dos pós. Por outro lado, as amostras sinterizadas pela rota de queima rápida suprimiram o crescimento com um fator de ~1 para os dois materiais. Esses resultados indicam que altas taxas de aquecimento minimizam o crescimento de tamanho de grão.

Palavras-chave: SOFC, SOEC, RSOFC, Fast Firing, YSZ, Sinterização, Modelagem.
.

ABSTRACT

Solid oxide fuel cells (SOFC) are cells for conversion of hydrogen into electrical power, highly efficient and clean, since produces electricity, heat, and solely water as exhaust gas by electrochemical processes. Solid Oxide Electrolyser Cells (SOEC) correspond to the reverse operation of SOFC. Reversible solid oxide fuel cells (RSOFC) are devices to produce energy and store it employing hydrogen as energy carrier, acting reversibly as fuel or electrolyser cells. A brief financial review shows RSOFC as a viable alternative for hybrid renewal energy systems. Current state of electrolyte, hydrogen and oxygen electrodes materials has been reviewed and discussed in detail, comparing common points between SOFC and SOEC developed here. Perovskites, Ruddlesden-Popper series and Double Perovskites materials show to have lower resistance, therefore, potentially more efficiency than the state-of-art oxygen electrode, lanthanum strontium manganite (LSM). A fine-grained microstructure can enhance key properties, for instance the state-of-art electrolyte yttria stabilized zirconia (YSZ) increase >95% the ionic conductivity comparing grain sizes 300 nm and 2.15 μm. To achieve fine-grained structure, must be employed powders with small particle sizes and sintering techniques to hinder the grain growth.

Ruddlesden-Popper series as $La_2NiO_{4+\delta}$-based materials exhibit high oxygen permeability, ionic conductivity among other properties advantageous for RSOFC. In this work, the synthesis and oxygen transport properties for a novel material ($La_{2-y}Sr_yNi_{1-x}Mo_xO_{4+\delta}$ $0.0 \leq y \leq 0.4$ and $0.0 \leq x \leq 0.1$) are reported. The phase relations analysis disclose low Mo solubility limit on the B-site of the $A_2BO_{4+\delta}$ structure. Single phase $La_{1.8}Sr_{0.2}Ni_{0.95}Mo_{0.05}O_{4+\delta}$ bar shape samples were cold-isostatically pressed and pressureless sintered at 1500ºC for 4 h. Sintered densities above 95% and grain size of 14.3±8 μm were obtained. A simple defect model was applied to explain electrical conductivity. Surface exchange coefficients (k_{chem}) and bulk diffusion coefficients (D_{chem}) in terms of temperature and P_{O2} were assessed by electrical conductivity relaxation (ECR) and discussed comparing with similar compounds, showing that doping the B site of lanthanum nickelate with Mo can enhance the oxygen transport properties.

To enhance the materials ionic conductivity, is desirable to manufacture the electrolyte using powders with small particle size and plan the sintering technique with the time-temperature profile to obtain fine-grained microstructures. There is a lack of accurate models to predict the compacts density during sintering. Here a densification model was developed to

predict densification, as a function of temperature, time and particle size. The model was able to predicting the achieved density using different sintering conditions. Sintering of powders leads to simultaneous densification and grain growth, particularly for nanocrystalline materials. Currently, methods such as spark plasma sintering (SPS), hot pressing (HP), two-step sintering (TSS) and fast firing (FF) are employed to hinder grain growth while maintaining a high densification. In this work, FF consisting in thermal treatments with high heating rates (>500º/min) and conventional sintering (RH) approaches were experimentally compared for yttria-stabilized zirconia (3YSZ and 8YSZ) compacts. Experiments were carried out in a tube furnace with a heating rate of ~500 °C/min (FF) and 10 °C/min (RH), analyzing the continuous density change and the grain size distribution of the dense structure. RH-samples present grain size bigger by a factor of ~4 and ~2 in comparison to raw powder for 8YSZ and 3YSZ respectively. Conversely, FF method completely suppresses grain growth at the experimental conditions with a growth factor of ~1 for both materials. Those results indicate that high heat inputs minimize grain growth.

Keywords: SOFC, SOEC, RSOFC, Fast Firing, YSZ, Sintering, Modelling.

.

TABLE OF FIGURES

INDEX OF TABLES

TABLE OF CONTENTS

1. GENERAL INFORMATION

1.1. CONTENT OF THE THESIS

This thesis was proposed under the cooperative network SOCs, for energy conversion from renewable sources in solid oxide cells, which was a joint Latin American–European project as contribution to technological research and development towards a feasible hydrogen economy.

Two main milestones of the group were:

- Production of hydrogen from steam using solid oxide electrolyser cells (SOECs).
- Use of sustainable, renewable energy sources as fuels in solid oxide fuel cells (SOFCs).

The plan was conceived to study a technology that could work in either objectives or directions, literally in *reversible solid oxide fuel cells (RSOFCs)*, which come into view as an appealing alternative to energy storage using hydrogen as energy carrier.

With the aim of contributing with innovations on the research field, a detailed state-of-art on reversible solid oxide fuel cells was first written, where the development of novel materials and processing techniques overcome the known drawbacks and improve the performance and economic feasibility for further commercialization of RSOFC technology.

Then, two different challenges to RSOFC development were addressed: synthesis and characterization of a new electrode material, and modelling of a fast firing process of a common electrolyte material.

Those 3 tasks are distributed in chapters 2, 3 and 4, respectively. There were developed as parallel work, which seek the complementary objectives. However, the topics are rather independent and were written following the same format. Separated introduction, methodology, results and conclusions are given in each chapter.

In *Chapter 2* some tutorial information is given regading the operation principles, processing parameters and performance evaluation of RSOFC systems. The state of the art includes the most recent findings, and detailed discussions of related topics.

Chapter 3 presents the synthesis of lanthanum nickelate doped with Sr and Mo (LSNM), and the analysis of their effect on transport properties. The conductivity and oxygen transport, bulk diffusion and surface exchange of LSNM were assessed by electrical conductivity

relaxation. The composition $La_{1.8}Sr_{0.2}Ni_{0.95}Mo_{0.05}O_{4+\delta}$, was subjected to measurements as function of temperature and oxygen partial pressure. Experimental results were discussed and compared with previous related works.

Chapter 4 presents two simultaneous studies directed to overcome grain coarsening during sintering in ceramic processing. Fast firing was compared to conventional sintering in ceramic compacts, and a general model was developed to predict the densification in powder compacts under different temperatures and time.

Finally in *Chapter 5,* the conclusions are summarized.

1.2. OBJECTIVES

1.2.1 General Objective

The main objective of this work is to contribute on the research field of reversible oxide fuel cells, identifying key issues and proposing alternatives solutions for some of the challenges related to materials and technology.

1.2.2 Specific Objectives

- To build a detailed state-of-art and analysis regarding solid oxide reversible cells RSOFC, including solid oxide fuel cells and solid electrolyser cells.
- To develop an innovative material intended for RSOFC electrode, including synthesis and characterisation of key transport properties.
- To study the microestrutural development during sintering for a material commonly used as electrolyte in RSOFC, analysing different sintering methods and pointing key issues to optimize the microstructure.
- To formulate a general model to predict relative density of samples during sintering cycles.

2. CURRENT DEVELOPMENTS ON REVERSIBLE SOLID OXIDE FUEL CELLS

ABSTRACT

Solid oxide fuel cells (SOFC) are the most efficient electrochemical devices for conversion of hydrogen directly into electrical power. Solid Oxide Electrolyser Cells (SOEC) correspond to the reverse operation of SOFC. Reversible solid oxide fuel cells (RSOFC) are devices to produce energy and store it employing hydrogen as energy carrier, acting reversibly as fuel or electrolyser cells. In this part of the thesis, RSOFC are presented as a feasible alternative for hybrid renewal energy systems. Current state of electrolyte, hydrogen and oxygen electrodes materials has been reviewed and discussed in detail, comparing different systems reported. Durability test, novel materials development and processing techniques were identified to overcome the known drawbacks and improve the performance and economic feasibility for further commercialization of RSOFC technology.

Keywords: SOFC, SOEC, RSOFC, Hydrogen, Oxygen, Steam.

2.1. INTRODUCTION

Problems related to greenhouse gas emissions, energy supplies and their costs, such as dwindling fossil fuel reserves, human and environmental diseases and climate change are strong arguments to shift towards a more environmentally benign fuel matrix based in renewable energy [1-4]. Finite fuel sources like coal, petrol and natural gas are the major energy suppliers, but the demand rate grows faster than the energy generation threatening the energy balance. Alternatively, the use of standalone or hybrid renewable energy systems can help meeting the future demand [5-9].

Renewable energy produces a varying supply of power. Demand for electrical power also varies continuously, encouraging energy storage to match supply and demand. Two approaches are normally used: batteries or a coupled fuel cell-electrolyzer with hydrogen as energy carrier [10, 11]. This review is focused on reversible solid oxide fuel cells (RSOFC), which operate in both fuel cell and electrolysis modes, fulfilling both requirements in a single device.

Key issues such as operation principles, processing parameters and performance evaluation of RSOFC systems are included. First, a brief presentation is given including technical viability, thermodynamic

fundamentals and current status of RSOFC. Then, a section for each main component (electrolyte, hydrogen electrode and oxygen electrode) is presented. Throughout the manuscript major research results and challenges in reversible solid oxide fuel cells are summarized.

2.1.1. Role and viability in renewable energy

Among fuel cells, solid oxide fuel cells (SOFC) are the most efficient (>60%) for conversion of hydrogen directly into electrical power, and one of the cleanest routes to produce electricity due to their low greenhouse emissions [12-14]. Solid oxide electrolyser cells (SOEC) correspond to the reverse operation of SOFC, which are also the most efficient comparing to low temperature electrolysers. Alkaline water electrolysers show efficiencies exceeding 80% [15] and polymer electrolyte electrolysis cells (PEEC) may reach 83.4% [16]. In comparison, efficiencies around 98% are reported for SOEC operating at 650°C. Moreover, high temperature electrolysis is more economic, according to previous studies. The cost involved in hydrogen production are lower than 66% of the hydrogen price generated by low temperature electrolysis [17]. Since it is a combination of SOEC and SOFC technologies, a RSOFC is a device that can work efficiently in both operating modes, as a fuel cell or as an electrolyser.

The ideal configuration of renewable energy systems depends on the environment and equipment issues. Thus, the final energy costs may vary in a broad range (0.149-1.104 US$/kWh) [18]. Comparative designs show that renewable energy systems are currently less cost intensive in specific conditions (e.g. 0.438 vs. 0.510 US$/kWh for solar-wind-diesel and diesel systems, respectively) [9, 18]. The payback time of hybrid wind turbine and hybrid photovoltaic panel systems is approximately 3-4 years and 6-7 years, respectively. For hydrogen use, the payback takes more time (up to 25 years), because of the high initial investment in the fuel cell, the electrolyser and the hydrogen tank [11]. However, a RSOFC can perform the fuel cell/electrolyser work in a single device, employing the available surplus of cheap off-peak energy from renewable sources for hydrogen production by electrolysis and using it to generate electricity with decreasing costs [18-20]. An economic analysis in a 1-year period, considering a RSOFC working 2920 h in SOEC mode and 2815.2 h in SOFC mode for a hybrid photovoltaic system found a comparatively low electricity cost of 0.068 US$/kWh [20].

In the future, reductions in the prices of renewable energy components are expected making the corresponding technology economically feasible. The benefits derived from these systems are continuous operation and low pollution levels. Notwithstanding, drawbacks discussed through the manuscript are still associated to solid oxide cells. Reliability, new materials, performance and stability are the main concerns for RSOFC research and development.

2.1.2. Operating principles and thermodynamics

As previously described, a RSOFC is a high temperature device able to operate as fuel cell (SOFC) and electrolyzer (SOEC). In SOFC mode, it can generate electricity by electrochemical combination of fuel with air. In SOEC mode coupled with a power source, it produces hydrogen by electrolysis of water, and also by co-electrolysis of H_2O/CO_2 (syngas), [14, 21]. Fig. 2.1 illustrates the operating principles of the RSOFC.

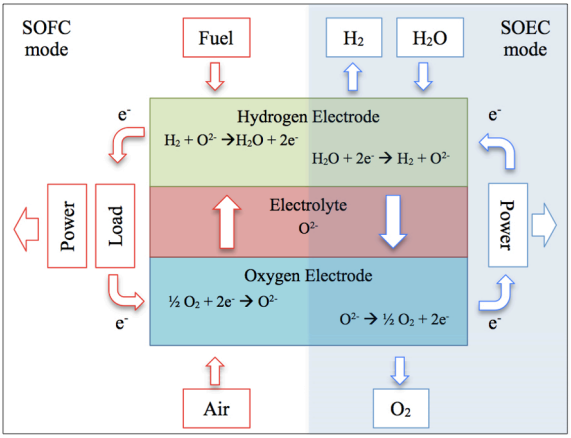

Fig. 2.1. Operating RSOFCs principles: SOFC (left) and SOEC (right) modes.

RSOFC cells work reversibly as shown in Fig 1. according to the reactions at the hydrogen electrode eq. (2.1), and oxygen electrode eq. (2.2), respectively, which may be combined into an overall reaction eq. (2.3). In this case, where the SOEC mode corresponds to the reactions carried out from left to right, and SOFC mode to the opposite way:

$$H_2O + 2e^- \rightleftharpoons O_2^- + H_2 \tag{2.1}$$

$$\frac{1}{2}O_2 + 2e^- \rightleftharpoons O_2^- \tag{2.2}$$

$$H_2O \rightleftharpoons \frac{1}{2}O_2 + H_2 \tag{2.3}$$

In the electrolysis mode, the total energy demanded is the enthalpy change, ΔH, described by the first law of thermodynamics as:

$$\Delta H = \Delta G + Q \tag{2.4}$$

where ΔG is the Gibbs free energy or the electrical energy demand, and Q are the heat energy demand. Each term can be estimated as [22-25]:

$$\Delta H = \Delta H^0_{298.15} + \int_{298.15}^{T} \Delta C_p \, dT \tag{2.5}$$

$$Q = T\Delta S \tag{2.6}$$

$$\Delta S = \Delta S^0_{298.15} + \int_{298.15}^{T} \frac{\Delta C_p}{T} dT \tag{2.7}$$

where T is the absolute temperature, ΔC_p is the heat capacity at constant pressure, ΔS is the entropy change, $\Delta H^0_{298.15}$ and $\Delta S^0_{298.15}$ are, respectively, the enthalpy and entropy at 298.15 K and 1 atm. Those properties are temperature-dependent and may be found in the literature for water and other substances [24]. When converted in terms of potential, they may be expressed as:

$$V_{th} = \frac{\Delta H + \Delta H_{evap}}{nF} \tag{2.8}$$

$$E = \frac{\Delta G}{nF} \tag{2.9}$$

where F is the Faraday's constant; n the number of electrons (2 for H_2); V_{th} is the thermoneutral voltage (necessary potential to perform electrolysis); and E is the Nernst potential related to the electricity demand.

From Eqs. (2.4)-(2.9), Fig. 2.2 can be built, showing that it is advantageous to operate the electrolysis cells at high temperatures, where a significant part of the required energy (ΔH) is provided as thermal energy (Q). Consequently the electric energy demand (ΔG), is considerably reduced. External heat might lower production costs, particularly when using geothermal sources or integrating the cell to industrial or nuclear heat waste to obtain high exergetic efficiencies [26-

28]. If not provided, the heat energy demand can be produced from Joule heat within the cell as a consequence of the flow of electrical current through the cell, hence, increasing the electric demand. As an example, feeding with liquid water instead of steam, the energy demand should be increased 0.21V, corresponding to ΔH_{evap} =40.65 kJ mol^{-1}.

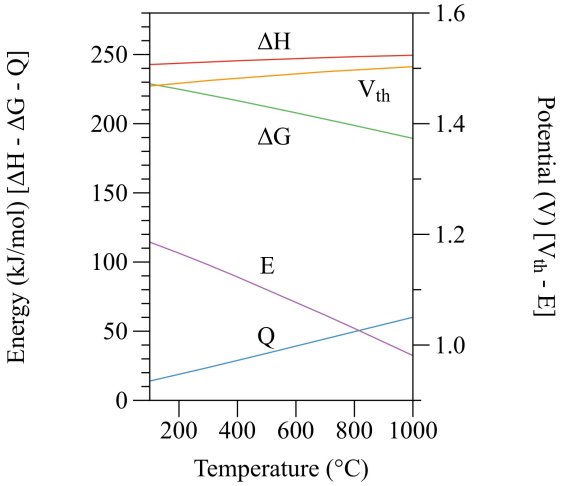

Fig. 2.2. Thermodynamics of steam electrolysis.

For every system, the efficiency follows the energy relationship in Eq. 2.10, so it can be written for both SOEC and SOFC mode as:

$$\eta_{System} = \frac{Energy_{useful}}{Energy_{in}} \tag{2.10}$$

$$\eta_{SOEC} = \frac{\dot{N}_{H_2\,out} LHV_{H_2}}{W_{in} + Q_{in}} \tag{2.11}$$

$$\eta_{SOFC} = \frac{W_{SOFC-net}}{\dot{N}_{H_2\,out} LHV_{H_2}} \tag{2.12}$$

where η is the efficiency, $\dot{N}_{H_2\,out}$ is the molar flux of H_2, and W is the power. Also the power can be estimated as:

$$W = VJ \tag{2.13}$$

where V is the voltage, J the current density. On the other hand, voltage and current density of the system can be used to estimate the hydrogen

production $\left(\dot{N}_{H_2,out}\right)$, from the Kirchhoff law and Nernst Equation as [22, 23]:

$$\frac{V}{J} = \text{ASR} \tag{2.14}$$

$$\dot{N}_{H_2,out} = J2F \tag{2.15}$$

where ASR is the area specific resistance. So reorganizing Eqs.(2.10)-(2.15), Eqs. (2.11) and (2.12) can be written as:

$$\eta_{SOEC} = \frac{V^2 LHV_{H_2}}{\text{ASR}(W_{in} + Q_{in})} \tag{2.16}$$

$$\eta_{SOFC} = \frac{V^2}{\text{ASR}(\dot{N}_{H_2,in} LHV_{H_2})} \tag{2.17}$$

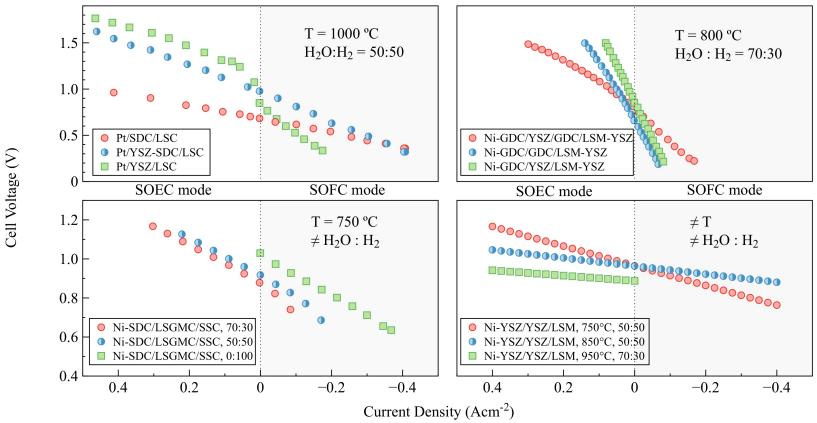

Fig. 2.3. Current density (*J*) *vs.* voltage (*V*) curves from different works [17, 29-31].

Hence, Eqs. (2.16) and (2.17) show that high ASR values represent lower efficiency in both RSOFC modes. From the slope of the relationship *J vs. V* the ASR value can be extracted. Fig. 2.3 shows *J vs. V* data for different conditions and materials [17, 29-31]. The values commonly follow a straight line which is affected by temperature and by the electrode materials, but they are independent from the inlet

composition and working mode. Thus, it is possible to construct an ASR *vs.* temperature diagram in order to compare different systems in this RSOFC common point (ASR lower better). Those diagrams are presented latter for each component: hydrogen electrode, oxygen electrode and electrolyte.

2.1.3. **State of the art for RSOFC**

Advancements in RSOFCs are influenced by progress in SOFC/SOEC technology. SOFC and SOEC have a long history resulting in a strong knowledge inherently in RSOFC, which comprises both modes of operation in the same cell [14, 21]. Practically, the development process is more limited by SOEC technology, where the constraints seem to be more critical and also less studied comparatively (Fig. 2.4). Nevertheless, research on SOEC is steadily increasing as seen in Fig 2.4. Researches have been published extensively during several decades and RSOFC has profited mainly from SOEC studies, since electrolysis investigators normally characterize the cells in SOFC mode. However, several critical issues are required to be addressed, which are specific to RSOFC, such as oxygen electrode performance and reversibility, set of materials, cell/stack designs and operating parameters suitable for reversible operation, and system design and integration to demonstrate the feasibility of the technology [32].

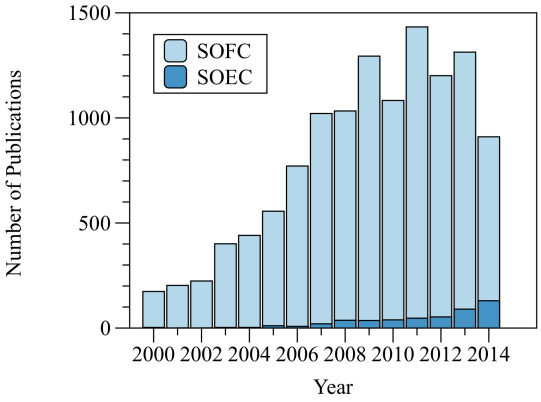

Fig 2.4. Number of publications on SOFC and SOEC according to ISI Web of Knowledge database.

The material usually employed for the electrolyte is yttria-stabilized zirconia (YSZ); as well as Ni/YSZ cermet for the hydrogen electrode; and $La_{1-x}Sr_xMnO_{3-\delta}$ (LSM) or $La_{1-x}Sr_xFe_{1-y}Co_yO_{3-\delta}$ (LSCF) for oxygen electrode. These compositions present a series of drawbacks discussed later, which limit the RSOFC systems. In this way, novel materials and long-term test are required for future developments in both SOFC and SOEC modes. In the following sections of this chapter, each component will be reviewed.

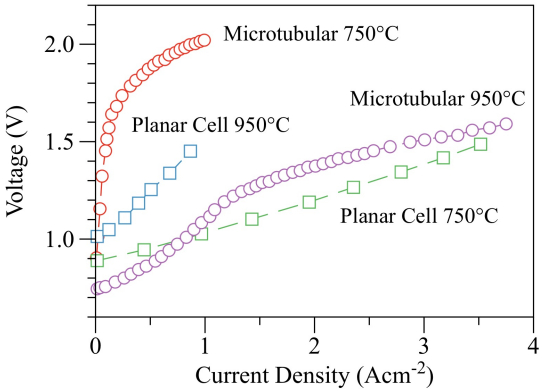

Fig. 2.5. Voltage *vs*. current density for microtubular [33] and planar [17] cells; system Ni/YSZ|YSZ|LSM/YSZ, 70% H_2O.

Most of the designs of cells are based on a planar configuration, and there are no remarkable differences related with the cell shape. For instance a comparison between microtubular and planar cells design with Ni/YSZ|YSZ|LSM/YSZ regarding *J vs. V* curves at similar operation conditions shows that the microtubular design presents S-shaped curve and is able to sustain current densities as high as 6 $A.cm^{-2}$ at 1.5 V. The internal resistance of the cell at high voltage values (above 1.3 V) is as low as 0.10 $\Omega.cm^2$ in SOEC mode at 950°C [33]. Those are high numbers comparing to a planar model with Ni/YSZ|YSZ|LSM/YSZ system [17] with current density of −3.6 $A.cm^{-2}$ at 950°C, 1.48 V 0.17 $\Omega.cm^2$. However, as seen in Fig. 2.5, the open circuit voltage (OCV) at 750°C for the microtubular design have lower electrochemical performance than the planar configuration. Designs with microtubular cells [16] reports efficiencies of ≈98% at HHV standard with ASR of 0.81 $\Omega.cm^2$ and test at the same temperature with a planar cells, presents ASR values lower as ≈0.53 $\Omega.cm^2$. This suggests

that the differences can be due to the system itself, i.e. materials and microstructural differences, but not due to the cell shape. However, the cell size is an important research topic in SOFC technology, scoping both scale-up for suitable designs in large power systems, and miniaturization for portable power units. Those designs have been successfully manufactured in tubular and planar shape [32].

2.2. ELECTROLYTES

The electrolyte for solid oxide cells must be stable in both reducing and oxidizing environments, and must have sufficiently high ionic conductivity (>0.1 Scm^{-1} [34]) with low electronic conductivity (~0 due to short-circuit see Fig. 2.1) at the cell operating temperature. In addition, the material must be able to be shaped into a thin, dense, strong film [14]. The electrolyte performance depends mainly on the operation temperature, thickness and material properties. The trend analyzing the ASR values for different systems in Fig. 2.6a and b, show that it is advantageous to operate cells with small electrolyte thickness at high temperatures independently on the used materials. High operation temperature is desirable owing to the ionic conductivity of the materials, which increase with temperature and also because of the electrochemical processes are thermally activated. Fig. 2.6b show the opposite trend, where larger thickness increases the area specific resistance [16, 17, 29, 30, 34-52].

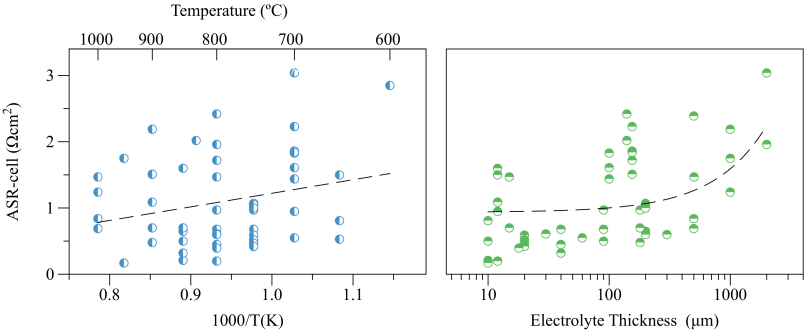

Fig. 2.6. a) Area specific resistance *vs.* operation temperature; b) area specific resistance *vs.* electrolyte thickness. Constructed from *J vs. V* tests for different systems reported in [16, 17, 29, 30, 34-52].

In Fig. 2.7, the ASR values for different cells are presented regarding the electrolyte material and operation temperature [16, 17, 29, 30, 34-52]. Yttria-stabilized zirconia is the most studied electrolyte material for RSOFC, although many other ion-conducting materials are available such as: other zirconia-based, ceria-based, $LaGaO_3$-based, and proton conduction electrolytes. YSZ has lower ASR values at temperatures higher than 700 ºC. At lower temperatures, protonic electrolytes as $BaCe_{0.5}Zr_{0.3}Y_{0.2}O_{3-\delta}$ (BCZY), or ceria-based electrolytes as: Samarium Doped Ceria (SDC) 20SDC-Li_2CO_3-Na_2CO_3 and Scandia Ceria Stabilized Zirconia (ScCSZ) has the lower ASR values, hence, are feasible compositions for intermediate temperature operation. YSZ has advantages as abundance, chemical stability, non-toxicity and cost [14, 53-59]. However, because of the poor ionic conduction at low temperature of the yttria-stabilized zirconia, other compositions materials become attractive to have higher ionic conductivity than YSZ at lower operation temperatures (see Fig 2.8), those compositions are discussed in this section.

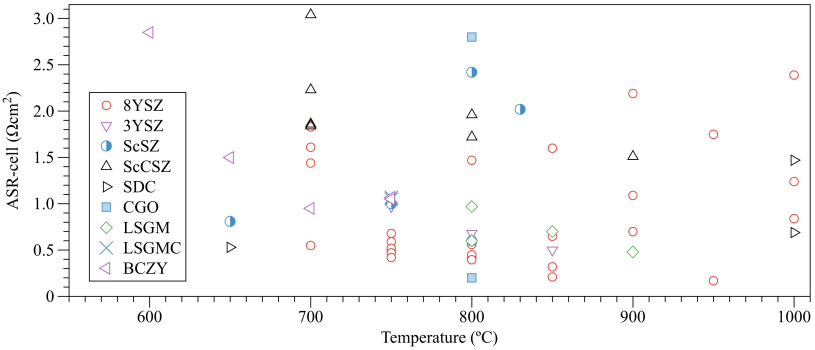

Fig. 2.7. Area specific resistance *vs.* temperature for different electrolyte materials: yttria-stabilized zirconia (8YSZ or YSZ), yttria-partially-stabilized zirconia (3YSZ), scandia-stabilized zirconia (ScSZ), scandia-ceria-stabilized zirconia (ScCSZ), samaria-doped ceria (SDC), gadolinium ceria oxide (CGO), lanthanum strontium gadolinium manganite (LSGM), lanthanum strontium gadolinium manganite cobaltite (LSGMC), barium ceria yttria zirconate (BCZY). Constructed from *J vs. V* tests reported in [16, 17, 29, 30, 34-52].

2.2.1. Zirconia-based electrolytes

As previously described, YSZ is the most commonly used electrolyte for RSOFC due to properties, cost and availability.

Nevertheless, some authors have reported on alternative electrolyte materials to YSZ, mainly due to its limitations at lower temperatures, i.e., decreasing in ionic conductivity (Fig 2.8) [12, 14]. It was shown that the choice of electrolyte material can influence the electrode performance, e.g., there are reported improvements for temperature interval from 700–900 ºC upon changing the electrolyte material from YSZ to the more expensive, but more conductive scandia stabilized zirconia (ScSZ) [60].

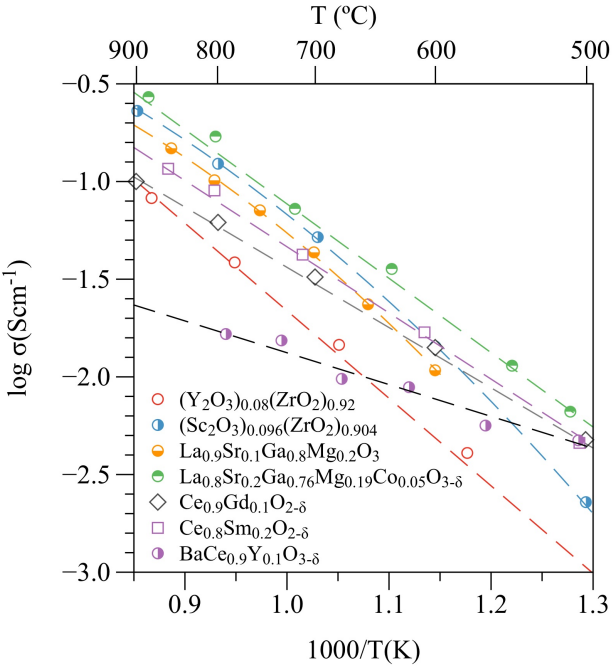

Fig. 2.8. Selected data on the ionic conductivity of electrolyte materials. [53-59].

Tests comparing YSZ and 4 mol% scandia-stabilized zirconia (4ScSZ) electrolyte supported cells over a temperature range of 800-900 ºC show a better performance for a ScSZ based cell. A 140 µm thick cell based on 4ScSZ yields ASR values of about 0.50 and 0.33 $\Omega.cm^2$ at 800 ºC and 850 ºC, respectively. The cell performance is continuous from SOFC to SOEC mode operation. However, it presents ASR degradation associated with thermal cycling, and short-term durability test in ScSZ based cell shows a degradation rate of 0.056 $mV.h^{-1}$ during 450 h

operation in SOEC mode [23, 61, 62]. Other composites containing ceria and scandia (e.g. 10Sc1CeSZ) show degradation near the electrode interface even at intermediate temperatures (500-750°C) and also high ASR values (1.84 $\Omega.cm^2$ at 700 °C) [44].

ScSZ compositions show conductivity degradation as function of time at high temperatures by the formation of an ordered phase rich in Sc. The degradation is lower in compositions containing Sc_2O_3 close to 9.3% mol. Below 9% mol, the degradation is higher due to the presence of a t-ZrO_2 phase, and above 10% mol due to the presence of a low conducting rhomboedral-phase ($Sc_2Zr_7O_{17}$) [54]. Another drawback of the ScSZ material is its high cost which limits a large-scale use [63, 64].

2.2.2. Ceria-based electrolytes

Substitution of YSZ as electrolyte by ceria-based have been reported benefical due diminished ASR-cell values. Electrolyte materials as samaria-doped CeO_2 (SDC) show lower ASR values (see Fig 2.8 at 700ºC). However, the partial reduction of ceria from Ce^{4+} to Ce^{3+} deteriorates the mechanical properties and reduces the current efficiency ($\eta_{ocv} \approx$ 68%) showing a H_2 poor evolution in SOEC mode [29]. In SOFC mode, the reduction causes electric conduction; therefore, a decrease of the power output [65].

Varying from short-circuit of SOFC mode to high voltage of SOEC conditions, the applied voltage sharpens the maximum tensile stress by seven times, and raises the minimum permitted oxygen partial pressure at the electrode-electrolyte interface, provoking electrolyte collapse even at 600 °C, suggesting the inapplicability of doped-ceria electrolyte in SOEC mode [66].

Gadolinium-doped CeO_2 (CGO) materials also present Ce^{4+} to Ce^{3+} reduction. At temperatures below 727 °C, $Ce_{0.9}Gd_{0.1}O_{2-\delta}$ (10CGO) is more stable than $Ce_{0.8}Gd_{0.2}O_{2-\delta}$ (20CGO). Incorporation of praseodymium oxide into 20CGO leads to a slight improvement of the stability at intermediate temperatures, but for 10CGO it is insignificant. Since interaction of ceria-based ceramics with electrode materials, such as lanthanum-strontium manganites (LSM), result in the formation of low-conductive layers at the electrode/electrolyte interface, optimization of electrode fabrication conditions is needed. Has been reported that surface modification of the electrode layers with praseodymium oxide results in decrease of cathodic overpotentials, suggesting higher electrochemical activity for electrodes of perovskite-type in contact with 20CGO electrolyte. However, Pr-CGO exhibits electronic conductivity

in the electrolyte and reduction in reducing environments, which decrease the cell performance [56, 67].

Single-phase ceria-based electrolytes conductivity limits the intermediary temperature applications (5×10^{-3}–3×10^{-2} $S.cm^{-1}$ at 600°C for GDC and SDC, respectively), which is not sufficient for high performance SOFCs that require 0.1 Scm^{-1} [34, 65]. Ceria-based composites (CBC) show overcoming problems of the single-phase ceria-based electrolytes. Electrolytes with 20SDC-Li_2CO_3-Na_2CO_3 as material can be used for intermediate and low temperature RSOFCs showing a low ASR value (0.53 $\Omega.cm^2$) with Pt electrodes, also present proton and oxygen ion conduction, effective for both SOFC (at 650 ºC $\approx$0.38$W.cm^{-2}$) and SOEC.

The electrolysis measurements show decomposition voltages of 1.0 and 1.75 V for the H^+ side and the O^{2-} side, respectively. Other ceria composites such as bi-layered electrolytes GDC/YSZ exhibit lower ASR-cell values for a factor of 5 in comparison with GDC and YSZ electrolyte in equal conditions. Besides, durability test suggest that the bi-layered GDC/YSZ approach can increase the cell stability with GDC as an interdiffusion layer of 2 μm, between the electrolyte and oxygen electrode, [31, 34, 50, 68, 69].

2.2.3. $LaGaO_3$-based electrolytes

Lanthanum gallates (LG) have been also proposed as electrolyte materials. LG is a perovskite oxide doped with divalent ions, typically Sr and Mg in La (A) and Ga (B) sites, respectively, which achieves high mobile oxygen vacancies concentration and thus high conductivity [52]. However, modifications are required due to its instability in presence of nickel. LG reacts with Ni, forming a stable $LaNiO_3$ phase [70-74]. Strategies as decreasing the Ni content (Ni-Fe 9:1 atomic) in the electrode is reported diminishing overpotentials and being benefical for RSOFC reversibility [75].

Even if conductivity of LGSM is entirely ionic over a wide range of oxygen partial pressure, LGSM presents electronic conductivity. The electronic conductivity tends to decrease with increasing A/B cation non-stoichiometry. Thus, doping with Co (LSGMC) can rise the overall conductivity dominated by ionic conductivity, however, the conductivity still develops an electrical component [55, 57]. Under oxidizing conditions, LSGM conductivity is almost completely ionic, but in reducing atmospheres presents electronic conductivity, resulting from the partial reduction of Ga^{+3} to Ga^{+2} [55, 57].

In spite of the drawbacks, systems based on LSGM show lower ASR values at intermediate temperatures than YSZ. For single cells LSGM based electrolytes, are reported lower ASR values as 0.6 $\Omega.cm^2$ for 800ºC, which are comparable to ScSZ-based cells [52]. In similar systems LSGM at 800°C shows lower polarization resistance in air and hydrogen than YSZ; 1.6 $\Omega.cm^2$ in air, 1 $\Omega.cm^2$ in hydrogen [76, 77] for LSCrAl and YSZ, and 0.18 in air, 0.09 $\Omega.cm^2$ in oxygen [78] for LSCrMN with LSGM.

2.2.4. Proton conducting electrolytes

Cells based on protonic electrolytes are also attractive due to the possibility to avoid H_2 separation, introducing both the steam and the oxygen feed at the oxygen electrode, and obtaining hydrogen at the hydrogen electrode [40]. High temperature protonic cells (HTPCs) show proton conductivity when exposed to hydrogen and/or steam containing atmospheres. The compounds are oxides with perovskite-related structure (ABO_3). They have an alkaline earth element, such as Ba, Sr, and Ca, in the A site while the B site is occupied by a rare earth element, usually Ce, Zr. To promote protonic conductivity, is commonly to dope the B site with trivalent elements, such as: Y, Nd, Sm, Yb, In, Eu, Gd. This leads to the formation of oxygen ion vacancies to increase the production of mobile protons [79]. Protons incorporated in the HTPC structure are generally not bound to any particular oxygen ion, but are instead free to migrate from one ion to the next. This enhanced migration results in high proton conductivity even at low temperatures as 500 ºC (see Fig 2.8) [80].

Barium zirconate cerates $Ba(Zr,Ce)O_3$ have been investigated for their higher stability of the zirconate combined with the higher grain boundary conduction of the cerate [81].

Tests on proton conducting electrolytes as $BaCe_{0.9}Y_{0.1}O_{3-\delta}$ (10BCY) and $BaZr_{0.9}Y_{0.1}O_{3-\delta}$ (10BZY) show lower conductivity for 10BZY, and a comparison with oxide ionic conducting electrolytes reflects a high ASR values, and even higher in SOFC mode (ASR_{SOEC} ≈8.5 $\Omega.cm^2$; ASR_{SOFC} ≈ 16.7 $\Omega.cm^2$ at 750ºC) [82]. The use of $BaCe_{0.5}Zr_{0.3}Y_{0.2}O_{3-\delta}$ (BCZY) as RSOFC has been reported, showing low ASR values, 0.95 $\Omega.cm^2$, at relatively low temperatures (700°C) [40]. Test regarding stability are required since is one the major concerns in proton conducting materials [83].

2.2.5. Manufacturing

As previously described, the electrolyte must be dense with a high ionic conductivity and negligible electronic conductivity. In Table 1 a data compilation is presented summarizing materials and processes for the electrolyte manufacture.

Table 2.1. Electrolyte Processing

Material	Processing	Thickness (μm)	T_{sint} (°C)	Ref
BCZY	Dry pressing	20	1400 (5h)	[40]
CBC	Pressing	500	—	[34]
SDC	Press molding	500	1600	[29]
ScSZ-GDC	Slurry coating	11	—	[16]
LSGM	Uniaxial pressing	265	1400 (4h)	[84]
YSZ	Dip coating	30	1500 (5h)	[39]
YSZ	Isostatic pressing (140 MPa)	150-500	1450	[85]
YSZ	Reactive magnetron sputtering (RMS)	2-10	1100 (3h)	[86]
YSZ	Screen-printing	12	1400 (4h)	[43]
YSZ	Slip casting	500	1400	[29]
YSZ	Tape casting + lamination	100	1550	[47]
YSZ	Tape casting + lamination	65	1500	[46]
YSZ	Tape casting + lamination (6 MPa at 614ºC)	50	1500	[87]
YSZ	Vacuum plasma spraying (VPS)	40	—	[41]
YSZ	Vacuum slip casting	5-30	—	[88]
YSZ-SDC	Slip casting, physical vapor deposition (PVD)	502	1400-1600	[29]
YSZ/Al_2O_3	Pressing	—	1300	[89]

Tape casting and lamination is the most usual technique [46, 47, 87]. Some layers are commonly manufactured from a mixture of electrolyte material and porous formers in different proportions or compositions (e.g. YSZ and graphite [46]), to produce a dense electrolyte layer in the middle with porous outer layers, with the aim of impregnate latter the electrode materials into the porous structure (40-60% of porosity [46, 47]). In this case, high ionic and electrical

conductivity are reached on the electrode side, due to the synergy of the porous electrolyte matrix with the electrode.

To enhance the materials ionic conductivity, is desirable to manufacture the electrolyte using powders with low particle size and plan the sintering technique with the time-temperature (T_{sint}) profile to obtain fine-grained microstructures [90-92]. For instance have been reported to increase >95% the ionic conductivity, for YSZ with grain sizes of 300 nm (209 mS/cm) compared with 2.15 μm (107 mS/cm) [90].

The sintering step is challenging, since powder sintering leads to simultaneous densification and grain growth, particularly for nanocrystalline materials. Regardless the use of dopants, spark plasma sintering (SPS) [93, 94], hot pressing (HP) [94, 95], two-step sintering (TSS) [96] and fast firing (FF) [97] are currently appropriate adopted techniques for production of nanostructured ceramics. The last two are pressureless unassisted techniques with the advantage of feasible implementation in conventional furnaces [92, 96-99].

In addition the temperature can lead to other effects as bloating or delamination. For instance, LSGM electrolytes may present bloating due to the volatilization of Ga_2O from the perovskite structure [57].

2.3. HYDROGEN ELECTRODES

The hydrogen electrode must be made from a high ionic and electrical conductivity material to transport the charges during the electrochemical reactions. As a material, is usual the use of a metal-ceramic mixture (cermet), where the metal component provides the electrical conductivity and the ceramic (electrolyte material) the ionic conductivity. The target for the overall conductivity for hydrogen electrode materials is set above ~100 $S.cm^{-1}$. However, the actual requirement depends on the cell design, and particularly on the length of the current path for current collection. Thus, this requirement may be relaxed to as low as 1 $S.cm^{-1}$ [100, 101].

As previously described Ni/YSZ cermet is generally adopted as hydrogen electrode. Long-term test points out that the electrode degradation is not directly related to the applied current density but rather a consequence of adsorbed impurities in the Ni/YSZ hydrogen electrode [17, 36, 102-105].

Postmortem test indicates degradation by presence of Zr-oxide nanoparticles on the surface of Ni grains, which has been identified as one of the major degradation mechanisms for Ni–YSZ electrodes under

SOEC operation where the degradation is higher than under SOFC mode [50, 106]. Other drawbacks reported for this material during operation are: Ni particles oxidation, steam starvation, layer peeling and grain coarsening [21, 29, 30, 41, 107, 108]. In the case of oxidation, it is attributable to the high temperature and concentrated electrolysis current at preferential regions at the electrode [30]. In addition, the lower performance with time can be related to the deposition of undesirable residues such as Si oxide [109] or Zr oxide particles on the on the surface of Ni grains or electrode pores, reducing the triple phase boundary (TPB: where gas, the ionic and the electronic conductor assemble and the reaction occurs) and poisoning the electrode [50, 106].

In spite of the drawbacks presented by Ni/YSZ composition, in general shows performance reversibility between fuel cell and electrolysis modes at low currents [32]. Tests in SOEC mode at 800 ºC report high stability for cells with Ni-YSZ as hydrogen electrode, for up to 500 h at current densities of 0.2 $A.cm^{-2}$ [110, 111]. However, with increasing current levels (1.5 $A.cm^{-2}$) both electrodes (hydrogen and oxygen) contributed to the overall cell degradation [112]. Other materials have been proposed to replace Ni/YSZ, which are discussed below.

2.3.1. Conventional cermets

Cu (60Cu:40YSZ) has been used to replace Ni, achieving slightly higher hydrogen production of 1.8 cm^3/min compared with 60Ni:40YSZ electrode with 1.4 cm^3/min. Cu combined with YSZ presents conductivities after sintering of 1.1×10^{-1} S/cm and 2.1 S/cm with 40 and 60 vol% Cu, respectively, which are lower comparing to 40 vol% Ni (1.0×10^4 S/cm) [85]. Ruiz-Morales et. al [113] report the formation of Y-rich cubic and monoclinic zirconia even at CuO content as low as 1 wt% sintering YSZ with Cu. Other issue described is a partial reduction of Zr^{+4} to Zr^{+3} that increases ≈25% the overall resistance. The impregnation method is proposed to overcome both problems, as well as manufacturing at low temperatures (<850 ºC oxidizing atmosphere and <700 ºC reducing conditions), for Cu electrodes intended for low temperature cells (~600ºC)[113].

For a LSGM-based electrolyte the use of different bimetallic electrodes Ni–Fe (9:1) atomic showed the smallest overpotentials for both hydrogen electrode and oxygen electrode. The addition of Fe to the Ni fuel electrode seems effective for improving the SOEC performance, where the potential losses become much larger than in SOFC mode [75].

Other strategy to enhance the performance is impregnating with nanoparticles of an ionic conductor as GDC, which increases the active region and decrease the electrode polarization resistance from the order of ~10 to ~0.1 Ωcm^2 [114].

Even though pure hydrogen is the preferred fuel for the SOFC mode, hydrocarbon fuels, reformed coal gas (syngas) and bio-derived fuels are attractive due to favorable costs and the facility of storage when compared to hydrogen. In the same way, working in SOEC mode with other sources as CO_2, or H_2O/CO_2 (syngas) is promising. Sources different than steam or H_2 may produce contaminants, including sulfur poisoning and/or coking due to high C-concentration decreasing the electrode performance. There are different strategies to diminish or avoid contaminants formation, such as use of thiospinels or metal sulfides as electrode material, modification of the traditional Ni/YSZ cermet, and adding mixed ionic and electronic conductors (MIEC).

Thiospinels (AB_2S4; i.e. $CuFe_2S_4$, $NiFe_2S_4$) and metal sulfides (i.e. WS_2, CoS_2, MoS_2) are materials able to avoid sulfuring for the decomposition of H_2S into H_2 [64, 115-118]. Though, their potential utility is in H_2S-rich fuels. At high H_2 content the benefit and reaction mechanisms remain unclear. Metal sulfides become stable by addition of Fe, Co, Ni or Ag [64, 118, 119]. However, those metals may present similar drawbacks as Ni under SOEC mode, where corrosion occurs increasing resistivity and change dimensions because of cell component swelling [108].

Tailoring of Ni/YSZ by composition is the usual approach to enhance performance, and sulfuring-coking resistance. In Table 2, a summary of tested materials is given, showing partial or total Ni substitution by conductive materials or oxides including perovskites and YSZ.

Modifications to the traditional Ni/YSZ cermets are focused in increasing TPB area by reaction sites enlargement to promote stability and catalytic activity through materials substitution, doping, introduction of active layers or particles, and microstructure refinements. For instance, Ni/YSZ infiltration with perovskite ($BaZr_{0.9}Yb_{0.1}O_{3-\delta}$) increase the structural stability and poisoning resistance [120] or coating with samaria-doped ceria (SDC, $Sm_{0.2}Ce_{0.8}O_2$) [121] resulted in polarization four-times lower. Optimized routes to produce fine-grained microstructures may decrease the polarization resistance, as the case of LSCM–YSZ nanocomposites, where the polarization is 30% lower for the composites synthesized via

polymerizable complex in comparison with LSCM–YSZ simple mixture [122].

Table 2. Modification of Ni/YSZ cermet, sulfur and/or coking poisoning summary.

Modification	Benefits	Drawbacks	Ref.
Substitution of Ni by cooper ((Cu/YSZ)	Cu resists coking formation and sulfur adsorption better than Ni	Lower conductivity; operation at low temperature (<700^{o}C) to prevent agglomeration of particles	[64, 85, 123, 124]
Replacement of Ni by selected oxides. (Oxide/YSZ)	Voltage drop diminished comparatively in presence of H_2S: none 0.59; Ce 0.2; Y 0.2; La 0.2; Mg 0.22; Nb 0.23; Sc 0.25; Zr 0.27; Ti 0.29; Ru 0.5.	By doping with Ca, Co and Al, the voltage drop remains equal or higher due to H_2S presence	[63]
Substitution of YSZ by scandia-doped zirconia oxide (ScSZ/Ni)	Improved conductivity and sulfur tolerance	ScSZ high cost limits application	[63, 64]
Ceria with Ni (CeO_2/Ni)	CeO_2 promotes sulfur and coking resistance	Degradation of a CeO_2 linked with the formation of ceria oxysulfide (Ce_2O_2S); otherwise, H_2S tolerance up to 900-5000 ppm	[125-127]
Cu and CeO_2 instead of Ni (Cu/CeO_2/YSZ)	High sulfur tolerance and good electro-catalytic performance and coking resistance	CeO_2 degradation and low temperature of operation due to Cu use	[64, 126, 127]
Copper, CeO_2 and cobalt instead of Ni and YSZ. (Cu/CeO_2/Co)	High sulfur tolerance and good electro-catalytic activity	Higher polarization resistance associated with slower electrochemical oxidation for fuels other than H_2	[128]
Doped gadolinium or ceria oxide with Ni (Ni/CGO)	Higher performance and sulfur tolerance compared to Ni–YSZ electrode.	CGO is not an effective sulfur absorbent as CeO_2. ; sulfur tolerance enhanced by higher CGO content which compromises electron transfer, increasing polarization overpotential	[129-133]
Doped samarium or ceria oxide with Ni (Ni/SDC)	Higher performance and conductivity	Poisoning by a small amount of H_2S	[129, 130, 134]
Infiltration of perovskite ($BaZr_{0.9}Yb_{0.1}O_{3-\delta}$) - Ni/YSZ	Improved performance and diminished H_2S and coking formation	Lack of stability tests	[120]

Alternatively, mixed ionic and electronic conductors (MIEC), which are perovskites and related phases, have been receiving increasing interest as material for the hydrogen electrode due to reduced interfacial polarization resistance, by expanding reaction sites from the TPB to the whole anode. MIEC-based materials present higher compatibility, stability and sulfur tolerance compared to metal components [100].

Perovskites have been found to be less reactive with H_2S than the Ni-based anode [135]. However, comparatively low catalytic activity towards hydrogen oxidation is the common challenge for the most MIEC electrodes. Perovskites as $BaZr_{0.1}Ce_{0.7}Y_{0.2-x}Yb_xO_{3-\delta}$ need composition optimization to achieve sufficient stability for H_2S as the case of [64, 136, 137]. One exception with higher catalytic activity are the double perovskite materials, which seem a possible replacement for the Ni-base anode [137]. Those compositions are discussed in the oxygen electrode section.

2.3.2. LSCM

LSCM-electrode cells present higher performance with lower ASR compared to other hydrogen electrode materials using YSZ as electrolyte at 700°C and lower polarization resistance in air and hydrogen; at 900°C: 0.29-0.59 $\Omega.cm^2$ [138], at 850°C: 0.27-0.34 $\Omega.cm^2$ [139], air-hydrogen respectively, this values suggest LSCM as possible hydrogen electrode and oxygen electrode for manufacturing symmetrical cells in SOFC mode. However, the modest electrical conductivity of LSCM in reducing environment (38 $S.cm^{-1}$ in air; 3 $S.cm^{-1}$ in H_2 [140, 141]), requires the addition of a electron conductive secondary phase, where Ni between 35-45 wt% are the usual content for application of this material as electrode [142].

Direct steam electrolysis was reported in SOEC mode, based on LSCM as electrode without reducing environment. It was found that the composite was stable without any potential degradation, but insufficient catalytic activity [46, 143, 144]. Curves and impedance measurements show limited performance of the LSCM in a humidified H_2 atmosphere [145], so this material appears suitable for SOEC CO_2 electrolysis, but not as RSOFC electrode.

2.3.3. Titanate composites

The perovskite-type ABO_3 titanate composites doped with Sr are alternative materials for solid oxide fuel cell hydrogen electrodes. To increase the low conductivity displayed by $Sr^{+2}Ti^{+4}O_3$, Sr^{2+} is partially

substituted by a trivalent ion such as La^{3+} (LST) or Y^{3+} (YST) [146-150]. In particular, A-site doped $La_xSr_{1-x}TiO_3$ (LST), $Y_xSr_{1-x}TiO_3$ (YST) and B-site doped $SrNb_xTi_{1-x}O_3$ (SNT), these materials show chemical stability when sintered with YSZ, and similar coefficient of thermal expansion to YSZ (CTE), and electronic conductivity in the range of 10–100 $S.cm^{-1}$.

The conductivities are achieved by reduction at high temperatures (>1300 ºC), which are higher than fuel cell operating temperature, thus can be done in-situ [146-152]. Comparative studies indicate that high conductivity and lower chemical expansion of these materials represent an incompatibility and therefore the material trend to form cracks or broke. Among them, YST materials present comparatively the best proportion conductivity/chemical expansion [101].

LST with GDC (GDC to increase the mixed conductivity) and impregnated Ni (Ni≈1 $mg.cm^{-2}$, to enhance catalytic activity) improves the cell performance by ≈460% maximum power density comparing to a similar cell with LST-GDC electrode [153].

Other titanate composites, such as $SrTa_xTi_{1-x}O_3$ (STT), show similar behavior. Redox stable conductivity can be achieved with x=0.01 and 0.05; lower dopant concentrations resulted in higher redox stable conductivities. Enhanced conductivity from a high temperature reduction was maintained after oxidation at 1000 ºC and reasonably good electrochemical performance was achieved when STT–YSZ was infiltrated with 3 wt% CeO_2 and 1 wt% Pd [154]. Those results show that via impregnation or microstructure optimization of doped-titanates may improve the performance as hydrogen electrode materials.

LST used in SOEC mode is feasible in direct steam electrolysis. However, the steam electrolysis performance is still restricted by the low catalytic activity of LST electrodes. This drawback might be again overcome by the use of Ni active nanoparticles impregnated to the electrode [155, 156].

2.3.4. Manufacturing

The hydrogen electrode is manufactured by several methods, according to strategies to improve the ionic-electronic conductivity, to taylor the porosity and to avoid delamination by thermal expansion mismatch with the electrolyte [14]. In Table 2.3, a data compilation is presented, summarizing techniques, processing parameters and materials related to production of the powder and manufactuing of the hydrogen electrode.

Table 2.3. Hydrogen Electrode: materials, synthesis, and processing variables.

Material	Composition (vol%)	Porous Formers	Mixing	Processing	Thick (µm)	T (°C)	Ref
Ni-YSZ	80NiO:20YSZ	—	Ball milling	—	—	1400	[29]
Ni-CeO_2-ZrO_2	Mixed oxides	—	Ball milling	—	—	—	[89]
Ni/YSZ	40NiO:60YSZ	—	Ball milling	Tape casting - spray painting	300-10	—	[17]
LSCM-YSZ-Pd/CYZ	Nitrates reaction in acid	Polystyrene Graphite	Ball milling	Tape casting - dip coating	60	1200	[46]
Ni/YSZ	—	—	—	—	—	—	[45]
Ni/YSZ	60Ni:40YSZ - 40Ni:60YSZ	—	Ball milling	Pressing	—	—	[157]
CeO_2	30% CeO_2 + $Co(NO_3)_2$ and $Ce(NO_3)_3$	Graphite	Ball milling	Tape casting - dip coating	300	—	[87]
Cu/YSZ	60Cu-40YSZ-40Cu-60YSZ	—	Ball milling	Screen-printing	30-50	1300 (Ar-5%H_2)	[85]
Ni/YSZ	—	Starch	Mechanical alloying	Dry pressing (250 MPa)	500	800 (2h)	[43]
Ni/YSZ	—	—	—	Air plasma spraying	50	—	[41]
Ni-CGO	—	—	—	—	30	—	[35]
Ni/BCZY	65Ni:35BCZY	—	Mechanical alloying	Screen-printing	40	1100 (2h)	[40]
Ni/YSZ	60Ni:40YSZ	PMMA; Potato starch; Ammonium oxalate	Mechanical alloying	Pressing (250 MPa)	—	800	[158]
$La_{0.98}Mg_{0.02}NbO_4$	Molten salts	—	Ball milling	Pressing	—	1200 (12h)	[159]
Ni/YSZ	60Ni:40YSZ	Starch	Ball milling	Pressing	1200	1200 (2h)	[39]
SFM[e]	—	Heraeus binder V006	—	Screen-printing	70	1150 (5h)	[37]
Ni/ScSZ	—	—	—	Ram extrusion	250	—	[16]
CeO_2/Pd	Oxides and Nitrates	—	Calcination	Dip coating (40 wt% slurry)	15	—	[87]

Ni is largely employed as the hydrogen electrode due to its high conductivity. Nevertheless, a wide variety of materials from Cu [85] to oxides such as CeO_2 [87], $La_{0.8}Sr_{0.2}Cr_{0.5}Mn_{0.5}O_3$ (LSCM) [46],

$La_{0.98}Mg_{0.02}NbO_4$ (LMN) [159] and $Sr_2Fe_{1.5}Mo_{0.5}O_{6-\delta}$ (SFM) [37] have been also proposed. Those materials are normally combined with the electrolyte material as: cerium gadolinium oxide (CGO) [35], yttrium doped barium cerate-zirconate (BCZY) [40] and yttria stabilized zirconia (YSZ) to avoid mismatch electrode-electrolyte due to thermal expansion, and also to enhance the ionic conductivity.

Normally the electrolyte and electrode raw materials are dry or wet mixed in powder form in a ball mill. Wet milling leads to uniform coatings of YSZ particles on Ni, developing more the network structure. Conductivities of $<10^{-5}$ and 2.5×10^{2} Scm^{-1} are respectively reported for dry and wet milled sintered samples of 60 vol% Nickel/yttria stabilized zirconia (Ni/YSZ) electrodes [157].

Different powder forming techniques have been used to produce the electrode, such as air plasma spraying, spray-painting, pressing, screen-printing, tape casting and dip coating as seen in Table 2.3. Air plasma spraying and spray painting are used to deposit thin layers (<70 μm) on a substrate [160]. Spray-painting, screen-printing, tape casting and dip coating requires the preparation of a ceramic suspension (powder + additives), and the use casting devices as spray, stencil, doctor blade and immersion holder. On spray painting the deposition is controlled to define the electrode thickness, normally in the range of 30 to 70 μm. In dip coating, the substrate might be a porous scaffold of the electrolyte material, this procedure has the advantage of lowering the percolation threshold for the electronic conductor (≈20%) in the case of Ni [88]. Extrusion is preferred to produce tubular geometries [16].

To increase the transport properties of the functional electrode, shaping is often carried out with sacrificial materials or pore formers to produce a porous the porous structure. Simulations show that porosity reduces concentration overpotentials [161]. Electrical conductivities decreased with porosity, regardless of the pore former used and discontinuity of the electrical conductor probably rises increasing porosity, which leads to higher ohmic resistances affecting electrical conductivities [158].

Porosity requirement for SOFC is reported to be between 35–40% [162]. Differences between SOEC and SOFC operating modes are attributed to different gas transport mechanisms, since Knudsen diffusion is affected by H_2O, which has much higher molecular weight than H_2 [48, 163], hence, higher porosity is needed for SOEC mode. This suggest that RSOFC electrodes, thee porosity may be setup roughly

at 50%, however, can be optimized due to compromise between conductivity and porosity.

Different pore formers and techniques have been used to produce the electrode porosity, achieving varied values as a function of the concentration as seen in Fig 2.9. Inorganic pore formers promote lower porosity than organics. Coated graphite (CG) shows less porosity taking into account the contribution of the reduction of Ni, but with the advantage of a lower metal amount to achieve higher electronic conductivity. CG conductivity is 83 Scm^{-1} higher for 19 vol% Ni in comparison to the conventional 38 vol% Ni graphite mixture, diminishing the percolation threshold from 37 to 19 vol% of Ni [164].

Other parameter to take into account is the particle size of the pore former. Smaller pore former particles surround and isolate other particles resulting in a decrease of the triple phase boundary (TPB), where the electrochemical reaction is carried out [165].

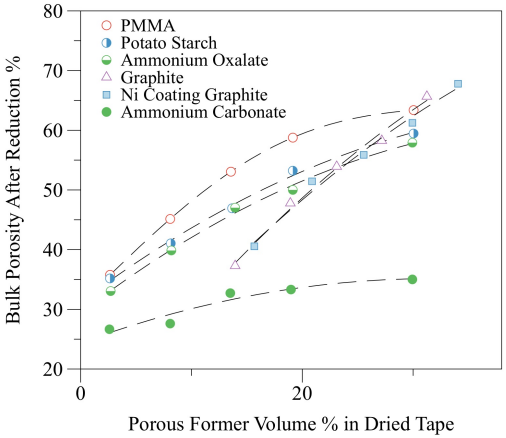

Fig. 2.9. Porosity of Ni/YSZ sintered samples *vs*. pore formers content; solid symbols [158] for 40 wt% Ni, white symbols [164] for 5 vol% Ni-coated graphite and 11 vol% Ni-coated graphite.

The cell needs to be supported on the electrolyte or electrode to provide mechanical strength, this means increase the thickness of the support. However, the increase in thickness of any component increases the losses on the cell [48]. The design strategy is to make a non-functional support with the same material of the hydrogen electrode with higher porosity and thickness than the functional part (Fig 2.10a). Those components can be produced by different methods as tape casting and

spray painting [17] or pressing several cast tapes with porous formers [46]. Other design supports the cell on the current collector, using a diffusion barrier to avoid electrodes contamination [41] (Fig 2.10b).

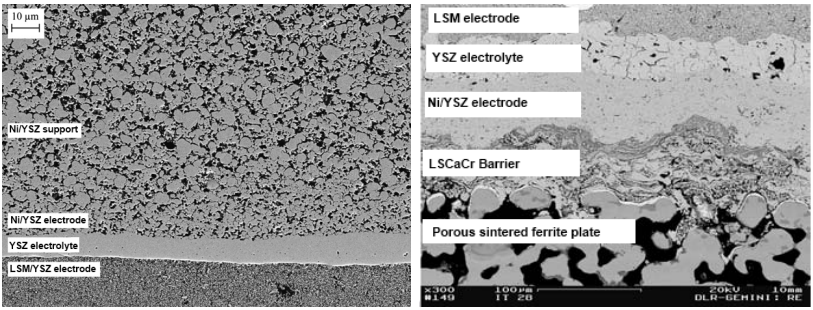

(a) (b)

Fig. 2.10. SEM micrographs: a) Ni/YSZ support [109]; b) diffusion barrier [41].

2.3 OXYGEN ELECTRODES

Oxygen electrodes for reversible solid oxide fuel cells have to present high electrical conductivity, high catalytic activity for oxygen reduction, and compatibility with other cell components. In the earliest stages of SOFC development, platinum was used as electrode since other materials were not available. However, platinum is practically not used anymore due to high cost. Less expensive perovskites are nowadays the most used materials [14].

As shown in Fig 2.11 conventional electronic conductors such as $La_{1-x}Sr_xMnO_{3-\delta}$ (LSM) are commonly used as oxygen electrodes for RSOFCs. LSM is mostly used because of high electronic conductivity and thermal expansion coefficient that match the YSZ electrolyte. In this case the electrode is electronic conductor and the reaction is limited to the triple phase boundary (TPB) region, where the air, electrode and electrolyte are in contact [166]. As a consequence, the performance is dependent on the electrode morphology and chemical and structural changes at the electrode/electrolyte interface. The majority of studies are devoted to control the complex electrode morphologies through processing, or adding a secondary ion-conducting phase or by using a mixed ionic-electronic conductor to increase the reaction region [49, 167-172].

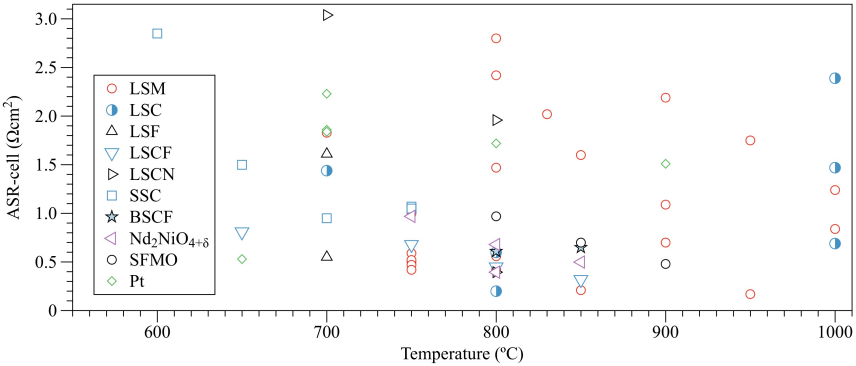

Fig. 2.11. Area Specific Resistance *vs.* Temperature for different oxygen electrode materials. Perovskites: $La_{0.8}Sr_{0.2}FeO_{3-\delta}$ (LSM), $La_{0.6}Sr_{0.4}Fe_{0.8}Co_{0.2}O_{3-\delta}$ (LSFC), $La_{0.6}Sr_{0.4}Fe_{0.8}Ni_{0.2}O_{3-\delta}$ (LSCN), $Sm_{0.5}Sr_{0.5}CoO_{3-\delta}$, $Ba_{0.5}Sr_{0.5}Fe_{0.8}Co_{0.2}FeO_{3-\delta}$ (BSCF). Ruddlesden-Popper**:** $La_2NiO_{4+\delta}$, (LNO), $Nd_2NiO_{4+\delta}$ (NNO). Double Perovskites: $Sr_2Fe_{1.5}Mo_{0.5}O_{6-\delta}$ (SFMO). Constructed from *J vs. V* tests reported in [16, 17, 29, 30, 34-52].

Comparing LSM and other perovskites in Fig 2.12, the ASR electrode values show that perovskites are potentially more efficient [59, 173-176]. Perovskite-type mixed ionic-electronic (MIEC) has predominantly low ASR comparatively with LSM, which present wide-range results (Fig 2.11). MIECs such as $La_{1-x}Sr_{x.}Fe_{1-y}Co_yO_{3-\delta}$ (LSCF) have been extensively [177-181]. Less attention has been paid to other perovskites and perovskite-related structures such as the Ruddlesden-Popper series and double or layered perovskites. This may be related to the perception that oxygen electrodes require simple structural types allowing three dimensional conduction pathways [182].

There are operation and stability differences of the solid oxide cells working in the SOFC and SOEC modes. Studies on distinct oxygen electrodes show that electrodes in SOEC mode exhibit higher potential losses, which are not affected by the oxygen partial pressure at the oxygen electrode side. SOFC mode changes considerably the maximum power density and potential losses [36, 177, 183-185]. Another feature is the stability, which is higher in the SOEC mode in comparison to SOFC mode. This degradation is more accentuated for electronic-conducting electrodes [32, 186, 187].

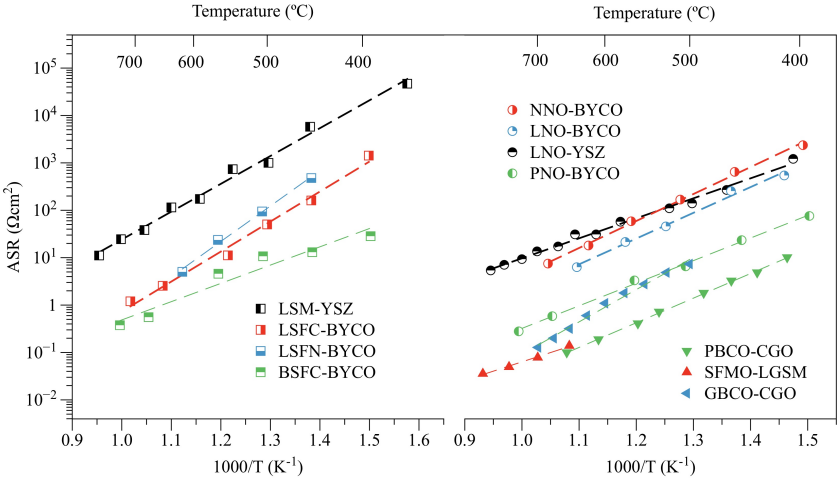

Fig. 2.12. Arrhenius plots of ASR for electrodes *vs*. Temperature: ■Perovskites: $La_{0.8}Sr_{0.2}FeO_{3-\delta}$ (LSM), $La_{0.6}Sr_{0.4}Fe_{0.8}Co_{0.2}O_{3-\delta}$ (LSFC), $La_{0.6}Sr_{0.4}Fe_{0.8}Ni_{0.2}O_{3-\delta}$ (LSFN), $Ba_{0.5}Sr_{0.5}Fe_{0.8}Co_{0.2}FeO_{3-\delta}$ (BSCF); ●Ruddlesden-Popper: $La_2NiO_{4+\delta}$, (LNO), $Nd_2NiO_{4+\delta}$ (NNO), $Pr_2NiO_{4+\delta}$ (NNO) ▲Double Perovskites: $Sr_2Fe_{1.5}Mo_{0.5}O_{6-\delta}$ (SFMO), $GdBaCo_2O_{5+\delta}$ GBCO, $PrBaCo_2O_{5+\delta}$ (PBCO) [59, 173-176].

The main cause of performance degradation of SOECs is attributed to the polarization losses at high current densities for the O_2 evolution reaction on the oxygen electrodes, which causes electrode structural and chemical changes [111, 112, 181, 188]. There are several degradation mechanisms of the oxygen electrodes reported in the literature, including electrode delamination at the electrode/electrolyte interface as a result of the formation of high internal oxygen pressure within the electrolyte, just near the oxygen electrode/electrolyte interface [111, 181, 188, 189], poisoning of the oxygen electrodes by contaminants such as chromium, strontium or silica [103, 109, 186, 190, 191].

At current density of 1 $A.cm^{-2}$ the major contributor of degradation is the oxygen electrode, but increasing at 1.5 $A.cm^{-2}$ both electrodes (hydrogen and oxygen) contributed to the overall cell degradation [112]. Similar results are achieved in long-term tests; cells operated at 0.5 $A.cm^{-2}$ exhibit no measurable resistance degradation or delamination over 1000 h of operation, regardless of cycling condition. This indicates the possibility of stable operation of RSOFC at low currents.

Conversely, cells operated at 1-1.5 $A.cm^{-2}$ show continuous degradation [181, 188].

The degradation rate is decreased for reversing-current relatively to constant-current electrolysis operation, and for decreasing cycle duration. The suppression of degradation by rapidly switching current direction is expected taking into account the proposed mechanisms, which involve formation of new phases or voids that have an incubation time [111, 188, 189, 192]. Thus, RSOFC durability appears to be more complex than a simple relationship with the time an electrode experiences in electrolysis mode [32, 188].

2.4.1. LSM

LSM is widely used as oxygen electrode material. Poor LSM ionic conductivity limits the cell performance, because the reaction only occurs in a small area between electrolyte and oxygen electrode (TPB). To increase ionic conductivity LSM is combined with the electrolyte material to form a composite electrode, which can extend the active area [17].

Has been reported that the electro-catalytic activity of LSM electrode was significantly enhanced for the O_2 reduction reaction in the SOFC mode [193-196], but the effect is not important in SOEC mode where the performance present limitations, showing deterioration after 20 to 24 h of operation. In this case, the polarization of the oxygen electrode contributed majorly to the polarization energy losses (up to 67%), which can be minimized to enhance the cell yield [39, 47].

In agreement with ASR values, Ni/YSZ-YSZ-YSZ/LSM can present different performances even at similar conditions and composition, for instance, 1.09 [43] and 0.17 [17] $\Omega.cm^2$ at 900°C. This suggests that efficiency improvements can be made, by optimizing the manufacturing parameters regarding the components microstructure.

In the case of SOFC stacks, the degradation rate is low as 0.5%/1000 h for a LSM oxygen electrode running over 19000 h [197]. Conversely, the SOEC stack has degradation high as ≈20%, for operation of 1000-2000 h [186, 190]. LSM electrode lifetime is in inverse proportion to the applied anodic current, and the increase of operating temperature can shorten the electrode lifetime [183].

Degradation mechanisms reported for LSM includes delamination, comprising interfacial formation of lanthanum zirconate ($La_2Zr_2O_7$), YSZ grain boundary porosity development, and morphological changes

related to the formation of nanoparticles within LSM grains close to the electrolyte surface [111, 192, 198].

The failure mechanisms indicate that stability can be increased extending the electrode reaction sites. This has been demonstrated by the implementation of engineering electrode nanostructured technology mainly by infiltration, effectively improving the electro-catalytic activity and stability under SOEC mode [49, 167-172]. For instance, the addition of GDC nanoparticles to LSM forming a continuous network for a 0.5 and 1.5 $mg.cm^{-2}$ GDC infiltrated, is reported a polarization resistance of 0.39 and 0.09 $\Omega.cm^2$ respectively, which are lower than 8.2 $\Omega.cm^2$ observed for the reaction on a pure LSM electrode, all at 800 ºC. The high thermal stability of the GDC nanoparticles under the oxygen rich SOEC operating conditions also contributes to microstructure stability [167].

2.4.2. Perovskites (ABO_3)

The increase of LSM performance has been reported by adding an ionic conducting secondary phase to increase the reaction sites. Another route is substituting its A and/or B sites (i.e. ABO_3, where A=La, Sr, Pr; B=Mn, Co, Fe) to produce ionic conductivity [199]. When Mn is replaced by Co or Fe–Co, enhanced activity is attained for oxygen reduction and increased ionic conductivity due to mixed ionic electronic conduction effect [166].

The overpotential measurements at similar conditions follow this increasing order: $La_{0.8}Sr_{0.2}CoO_{3-\delta}$ (LSC) < LSM < $La_{0.8}Sr_{0.2}FeO_{3-\delta}$ (LSF) [177], showing that MIEC materials exhibit higher electrochemical performance. LSC presents poor performance comparing to LSM and cannot be used with the Cr current connectors, because poorly conducting secondary phases are formed. The dissociation of LSC-Cr contact layer leads to the deterioration of the electronic activation and thus contributes to the degradation in SOEC mode [191].

$La_{1-x}Sr_xFe_{1-y}Co_yO_{3-\delta}$ (LSCF) has been reported to have high electro-catalytic activity and the polarization resistance (R_p) is lowest for deficient A-site (x=0.15), 14.8 and 2.75 $\Omega.cm^2$ at 600 and 700°C, respectively; and 0.58 at 800°C for x=0.10 [178]. The R_p value of LSFC with 20 mol% Sm-doped ceria has been reported as 0.23 $\Omega.cm^2$ at 700°C and 0.067 $\Omega.cm^2$ at 750°C [179]. This shows that mixtures of MIECs with doped ceria compounds decrease the overpotentials, therefore,

increasing the electrochemical performance ($Sm_{0.5}Sr_{0.5}CoO_{3-\delta}$, R_p= 0.18 Ω.cm²) [180].

Mixed-conducting oxygen electrodes such as LSCF has shown higher performance and stability compared with LSM for RSOFC [186]. Furthermore, LSCF values reported of 0.68 $\Omega.cm^2$ for YSZ, and 0.81 $\Omega.cm^2$ for ScSZ-CGO at 750 and 650°C with LSCF as electrode shows higher performance regardless of the electrolyte even at intermediate temperatures (see Fig 2.12). In the case of SOFC stacks, the degradation rate is 0.6-1.4%/1000 h for LSCF oxygen electrode [200, 201], and, the SOEC stack presents higher degradation rate, 5.6%/1000 h, for a LSCF oxygen electrode operating for ≈4000 h [202].

The degradation due to the change in the phase of LSCF or cation (e.g., Sr) segregation occurs in the SOFC and SOEC mode. Layers of SDC on the oxygen side are effective for lowering the resistance without deterioration in the open circuit voltage [29]. The electrochemical performances were improved remarkably by the addition of SDC to the oxygen electrode. For example, current densities with 40 vol% SDC were up to 5 times higher than using just LSCF [203]. CGO layers in between the oxygen electrode may diminish the formation of instable interphases, which may cause delamination in SOEC mode, as reported for LSC and LSCF materials used as oxygen electrodes [204, 205].

The initial ASR value for cells with YSZ electrolytes with a CGO layer is higher, but more stable with time [50, 106, 205]. Long term tests report, structuring of grain surfaces in the electrolyte, voids formation along grain boundaries affecting mechanical properties and ohmic resistance, horizontally aligned pores especially at the 8YSZ/CGO interface, formation of a dense layer at the 8YSZ/CGO interface, compositional fluctuations in the LSCF electrode affecting the ohmic resistance, recrystallization of LSCF in the electrochemically active area affecting the catalytic behavior of the electrode [181].

$Ba_{0.5}Sr_{0.5}Fe_{0.8}Co_{0.2}FeO_{3-\delta}$ (BSCF) used in SOFC mode has small polarization resistance (R_p=0.1 Ω.cm²) even at temperatures as low as 600°C [206]. This is considerably lower than other perovskite-based electrode materials (e.g. 14.8 Ω.cm² for LSC [178]). A significant performance decay of BSCF cell is observed under SOEC mode after 20 h, compared to a relatively stable LSM-YSZ at same operation conditions [39].

2.4.3. Ruddlesden-Popper series

Ruddlesden-Popper series or A_2BO_4-type oxides are phases that can be looked as natural heterostructures with alternating blocks of rock-salt and perovskites, where the oxygen is very mobile within the rock-salt layer, helping the oxygen evolution [182].

There is special attention on materials such as $A_2NiO_{4+\delta}$, with A=Nd, La or Pr, which have been widely investigated in RSOFC mainly for its oxygen transport properties [207]. Comparing the electrochemical behavior of nickelate-type electrodes, Nd-nickelate (NNO) presents the higher activity [174]. The phase presenting the highest oxygen diffusion and the lower cathodic ASR values is $Pr_2NiO_{4+\delta}$ (PNO) [59, 208]. The main drawback of the nickelate electrodes is its reactivity with YSZ and GDC, which limits its application for being the most used electrolytes [209, 210]. To avoid the reactions, the electrode materials should keep below the reactive threshold for some of the nickelates, for $La_2NiO_{4+\delta}$ (LNO) YSZ: T>900ºC, GDC: T>700ºC), for NNO YSZ and GDC:T>1000ºC, for Pr-derivative is inconclusive due to $Pr_2NiO_{4+\delta}$ decomposition [51, 209-211]. However, typical sintering temperatures are usually higher than 1000 ºC in order to get strong adhesion at the electrode/electrolyte interface, electrode strength and interconnected microstructure. To overcome this issue the infiltration technique of nickelate salt precursors followed by calcination has been implemented with success [51].

Test comparing SOEC and SOFC with LSM confirm a better performance of NNO. For 1.3 V of operation voltage, the current density is 1.7, 3 and 4.2 times higher for the cell containing $Nd_2NiO_{4+\delta}$ at 850, 800 and 750°C, respectively. Hence, is convenient to use $Nd_2NiO_{4+\delta}$ as oxygen electrode at temperatures below 800°C [35]. Studies on LSCN demonstrate to be active as an oxygen electrode for both SOFC and SOEC applications [38], but the electrode/electrolyte interface must be optimized. Moreover, LSCN was tested only under lower steam conditions [21]. For the LNO electrode, ASR values can be reduced from 6 to 0.11 $\Omega.cm^2$ by optimizing the microstructure to fine-grained [212]. This can be done with the sintering techniques described in the electrolyte section. In addition, the overall conductivity at elevated temperatures has been reported as >100 $S \cdot cm^{-1}$ [213]. Thus, Ruddlesden-Popper series show properties requirement as low ASR, high conductivity, and oxygen transport properties to be used to oxygen electrode in RSOFC. However, R&D improvements are required to

optimize the microstructure, manufacture and increase the compatibility electrode-electrolyte.

2.4.4. Double perovskites

Ordered double perovskites with general formula $AA'B_2O_{5+\delta}$, where A is a rare earth, A' an alkaline earth and B is Co or Mn, have been recently proposed as next generation electrode materials for intermediate and low temperature operation. Materials such as $GdBaCo_2O_{5+\delta}$ and $PrBaCo_2O_{5+\delta}$ show higher desirable properties for electrodes, as high conductivity (550 and 400 $S.cm^{-1}$ at 500 ºC respectively) and high oxygen transport properties ($D^*=2.8x10^{-10}$; $3.6x10^{-7}$ $cm^2.s^{-1}$ respectively), in comparison to LSM (120 $S.cm^{-1}$, $4.5x10^{-20}$ $cm^2.s^{-1}$) [173, 175, 182]. However, they have not been tested as materials for electrode at SOEC mode.

Other related double perovskites with fully occupied lattice with formula $A_2B_2O_{6-+\delta}$ have been extensively studied, such as $Sr_2Fe_{1.5}Mo_{0.5}O_{6-\delta}$ (SFMO), in which Fe and Mo exhibit order leading to a double perovskite unit cell [214]. SFMO has been tested as oxygen electrode for RSOFC, showing high performance with LSGM as electrolyte according to ASR values of 0.97, 0.70, 0.48 $\Omega.cm^2$ at 800, 850, 900°C. For this material a voltage drop under electrolysis operation (16% after 10 h, 24% after 100 h) [37] is observed. Although this fact suggests instability, the system presents satisfactory results in symmetrical cells and it is also a candidate for hydrogen electrode. Comparing to other electrode materials, SFMO has high conductivity (780ºC 550 and 310 Scm^{-1} in air and hydrogen respectively) and low R_p (0.24-0.27 $\Omega.cm^2$ in air and hydrogen respectively with LSGM as electrolyte) [37, 215]. SFM also shows high oxide ionic conductivity of 0.13 $S.cm^{-1}$ at 800 °C [216]. A decrease of a factor of two in the polarization values of SFM has been reported, at 750 °C, using CSO nanoparticles [215]. However, SFMO readily reacted with water to form an irreversible $Sr(OH)_2$ phase. This imposes severe restrictions in RSOFC application for this material, which also is unstable over time in air at temperatures higher than 400 °C, and it quickly dissociate into $SrMoO_4$ and $SrFeO_{3-x}$ [217, 218].

Nb-doped SFMO shows short-term stability in SOFC mode with no observable degradation over 15 h when operating at 750 °C. These results show that Nb-doping can improve the SFM materials stability, but this doping has not been tested so far in SOEC mode. The results

show that SFMO stability can be further improved by doping, for instance with $Ce_{0.8}Sm_{0.2}O_{1.9}$, Nb, Co [215, 219-221].

2.4.5. Manufacturing

As previously described, the oxygen electrode is manufactured from a material with high ionic and electric conductivity. Table 4 shows a data compilation of techniques and materials for processing the oxygen electrode. Lanthanum manganites doped with strontium ($La_{1-x}Sr_xMnO_{3-\delta}$, or LSM) are largely used as oxygen electrode materials. Perovskite materials and related structures with different elements in the composition follow a similar synthesis route as LSM. The strategy to manufacture is to mix the A or B components of the desirable structure in the stoichiometric amounts, e.g. perovskites (ABO_3); the site A with alkaline elements such as Ba, Sr, Ca, Pr; and the site B with transition metals such as Mn, Co, Fe, Ni [215]. For instance, in the mixed oxide $La_{1-x}Sr_xCo_yFe_yO_{3-\delta}$ (LSCF), La increases the δ value; in presence of oxygen, Co oxidation state is instable between +3 and +4 in comparison with Fe. Thus, increasing the oxygen vacancies increases the ionic conductivity or oxygen excess in the case of $A_2BO_{4+\delta}$ type oxides [222].

The oxide powders are produced through reaction of nitrates or acetates of the constitutive elements in acid; e.g. $La(NO_3)_3{\cdot}6H_2O$, $Sr(NO_3)_2$, $Fe(NO_3)_3{\cdot}9H_2O$ in NH_4NO_3 for LSF [46], the powders are obtained after a calcination at high temperature temperature (see Table 2.4) and later mixed in a ball mill if combined with the electrolyte material. The oxides can be fabricated in the same way from the elementary oxide or carbonate precursors [35, 207]. For instance the synthesis of LSN by calcination or also called solid state reaction (SS), involves the precursors: $SrCO_3$, NiO_3, La_2O_3, weighted in stoichiometric amounts to achieve the composition after calcination [207]. Other technique that end up in a fine grade powder is spray pyrolysis (SP), where elementary stable solutions of the precursors are mixed in stoichiometric amounts to produce the compositions, so the precursor solution are pumped with pressurized air to give atomized spray and pyrolised in a rotating furnace at high temperature (≈850ºC) [207, 223]. The compositions and phases may be checked afterwards by XRD.

The electrochemical performance of electrodes depends on the synthesis method. Composites of LSM/YSZ processed via glycine-nitrate combustion adding YSZ powder to the reaction materials showed

that this technique lowers the ASR to 0.52 $\Omega.cm^2$ at 850°C when comparing with traditional LSM and YSZ mixture [43]. Also comparing methods as SS and SP, disclose that those manufactured by SP presents higher oxygen diffusion, and surface exchange coefficients, attributed to the lower particle sizes resulting from the SP process and inherently fine-grained microstructure [224].

Porous formers are used to generate porosity in the oxygen electrode. Graphite, carbon black, cornstarch, and rice starch have been used as pore formers. Graphite is the most suitable pore former according to the electrode performance [225]. The porosity generated by graphite depends on the electrode materials (Fig 2.13), which might be adjusted to produce the porosity, which may also help to avoid delamination between layers [223]. According to thermo-gravimetric analysis, the porous former may help to diminish the rate of shrinkage of screen-printed layers, avoiding stresses that cause cracks and poor performance. Electrode porosity changes have small effect on SOEC performance [226]. However, porosity about 60% for LSCF [203] and between 50% and 60% for LSC have been reported as optimal values. For porosity higher than 60%, the contact between particles became worse increasing the overall resistance [203].

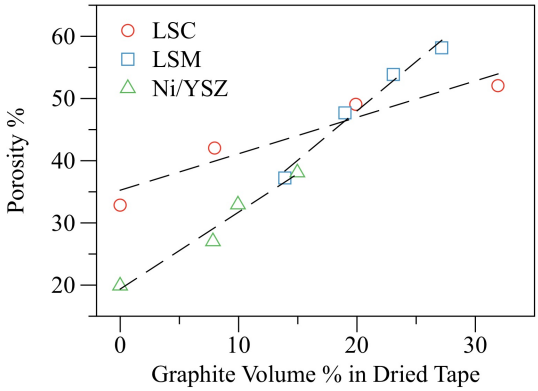

Fig. 2.13. Porosity of solid oxide cell components *vs*. graphite content: LSC [223], LSM [227], Ni/YSZ [164].

Table 2.4. Oxygen electrode processing

Material	Precursors	Powder Synthesis	Processing	Thick (μm)	T (°C)	Ref.
LSM	Acetates Mixture	Calcination (900°C)	Dip coating	—	1200	[29]
LSC	Acetates Mixture	Calcination (900°C)	Dip coating	—	1200	[29]
LCM	—	Spray Pyrolysis (1200°C)	Screen-printing	—	1300	[89]
LSF-YSZ	Nitrate salts	—	Dip coating	300	1250	[47]
LSC-YSZ	Nitrate salts	—	Dip coating	300	1250	[47]
LSM-YSZ	Nitrate salts	—	Dip coating	300	1250	[47]
LSM-YSZ	50LSM:50YSZ	Ball milling	Spray-painting	10	—	[17]
LSF-YSZ	Nitrate salts	Calcination (900°C)	Dip coating (suspension 40% wt)	300	900	[46]
Co/CeO_2	Nitrates-Oxides	Calcination	Dip coating (suspension 40% wt)	15	—	[87]
BSCF-SDC	Acid-Nitrates	Calcination	—	—	1000	[42]
LSM/YSZ	—	Ball milling (2 h, 5 wt% ethyl-cellulose 95% wt terpineol)	Screen-printing	50	1180	[43]
LSCF	—	—	Plasma Spraying	30	—	[41]
$Nd_2NiO_{4-\delta}$	Nd, Ni Oxides in Nitric Acid	Annealing (1000 ◦C 12h)	Screen-printing	30	1100	[35]
SSC/BCZY	70SSC:30BCZY	Ball milling (in ethocel and abietyl alcohol)	Screen-printing	40	1100 (2h)	[40]
SFM	—	—	Screen-printing (binder as pore former)	70	1150 (5h)	[37]
BSCF	Acid-Nitrates	Calcination	Screen-printing	30	1000 (1h)	[39]
LSC	Nitrates	Spray Pyrolysis	Screen-printing	36	1000 (1h)	[223]
LSCF/CGO	—	—	Dip coating	30	—	[16]
LSCN	Oxides	Calcination (1100°C 18h)	Screen-printing	10	1000 (2h)	[38]

The process design parameters, such as sintering conditions, composition and oxygen electrode thickness can affect polarization resistance [199]. Sintering parameters should be optimized for the specific system, for instance, differences lower than 50°C can rise by 3 order of magnitude the electrode polarization resistance (R_p) for $Pr_{0.58}Sr_{0.4}Fe_{0.8}Co_{0.2}O_{3-\delta}$-CGO (PSFC-CGO) electrodes [199].

The processing technique must be selected mainly by the shape and size of the components. Although ceramic processing involves a broad variety of methods, pressing, tape casting, dip coating and screen printing are preferred [160]. Those processes were already discussed in the hydrogen electrode manufacture section.

2.5. SUMMARY

Reversible solid oxide fuel cells (RSOFC) were presented as a feasible alternative for energy storage using hydrogen as energy carrier. The current state of development of electrolyte, hydrogen and oxygen electrode materials has been reviewed in detail. RSOFCs technology has potential and the advancements in RSOFCs are growing by following the progress in SOFC/SOEC technology. However, it is required to address critical issues specific to the RSOFC.

Hydrogen and oxygen electrode performance and reversibility which mostly result in delamination of the oxygen electrode at high current densities, due to O_2 evolution reaction on the oxygen electrodes, which causes electrode structural and chemical changes.

Although it is indicated the possibility of stable operation of RSOFC at low currents, cells operating above 1 A.cm-2 show continuous degradation, which diminished decreasing cycle duration. However, switching and degradation mechanisms are not fully understood.

The stacks design, long-term tests and improvements are strongly focused on Ni/YSZ/(LSM or LSCF). Less attention has been dedicated to configurations regarding other materials with different structures, where key research features are scarce, as: degradation, stability and microstructural optimizations.

In addition, the development of novel materials and new processing techniques are required to overcome the known drawbacks and improve the performance and economic feasibility for further commercialization of RSOFC technology.

2.6. REFERENCES

[1] (U.S.) NRC. Hidden costs of energy : unpriced consequences of energy production and use. Washington, D.C.: National Academies Press; 2010.
[2] Panwar NL, Kaushik SC, Kothari S. Role of renewable energy sources in environmental protection: A review. Renewable and Sustainable Energy Reviews. 2011;15:1513-24.
[3] Suranovic S. Fossil fuel addiction and the implications for climate change policy. Global Environmental Change. 2013;23:598-608.
[4] Höök M, Tang X. Depletion of fossil fuels and anthropogenic climate change—A review. Energy Policy. 2013;52:797-809.
[5] Ball M, Wietschel M, Rentz O. Integration of a hydrogen economy into the German energy system: an optimising modelling approach. Int J Hydrogen Energ. 2007;32:1355-68.
[6] Rehman S, El-Amin IM, Ahmad F, Shaahid SM, Al-Shehri AM, Bakhashwain JM, et al. Feasibility study of hybrid retrofits to an isolated off-grid diesel power plant. Renewable and Sustainable Energy Reviews. 2007;11:635-53.
[7] Shaahid SM, Elhadidy MA. Technical and economic assessment of grid-independent hybrid photovoltaic–diesel–battery power systems for commercial loads in desert environments. Renewable and Sustainable Energy Reviews. 2007;11:1794-810.
[8] Straatman PJT, van Sark WGJHM. A new hybrid ocean thermal energy conversion–Offshore solar pond (OTEC–OSP) design: A cost optimization approach. Solar Energy. 2008;82:520-7.
[9] Erdinc O, Uzunoglu M. Optimum design of hybrid renewable energy systems: Overview of different approaches. Renewable and Sustainable Energy Reviews. 2012;16:1412-25.
[10] Stoutenburg ED, Jenkins N, Jacobson MZ. Power output variations of co-located offshore wind turbines and wave energy converters in California. Renewable Energy. 2010;35:2781-91.
[11] Türkay BE, Telli AY. Economic analysis of standalone and grid connected hybrid energy systems. Renewable Energy. 2011;36:1931-43.
[12] Larminie J, Dicks A. Fuel Cell Systems Explained (2nd Edition). 2nd ed. Chichester: John Wiley & Sons; 2003.
[13] Rand DAJ, Dell RM. Hydrogen energy: challenges and prospects. Cambridge: RSC Publishing; 2008.
[14] Singhal SC, Kendall K. High-temperature solid oxide fuel cells : fundamentals, design, and applicatons. New York: Elsevier Advanced Technology; 2003.
[15] Schiller G, Henne R, Mohr P, Peinecke V. High performance electrodes for an advanced intermittently operated 10-kW alkaline water electrolyzer. Int J Hydrogen Energ. 1998;23:761-5.

[16] Wang ZW, Mori M, Araki T. Steam electrolysis performance of intermediate-temperature solid oxide electrolysis cell and efficiency of hydrogen production system at 300 Nm(3) h(-1). Int J Hydrogen Energ. 2010;35:4451-8.
[17] Jensen SH, Larsen PH, Mogensen M. Hydrogen and synthetic fuel production from renewable energy sources. Int J Hydrogen Energ. 2007;32:3253-7.
[18] Akikur RK, Saidur R, Ping HW, Ullah KR. Comparative study of stand-alone and hybrid solar energy systems suitable for off-grid rural electrification: A review. Renewable and Sustainable Energy Reviews. 2013;27:738-52.
[19] Hotza D, Diniz da Costa JC. Fuel cells development and hydrogen production from renewable resources in Brazil. Int J Hydrogen Energ. 2008;33:4915-35.
[20] Akikur RK, Saidur R, Ping HW, Ullah KR. Performance analysis of a co-generation system using solar energy and SOFC technology. Energy Conversion and Management. 2014;79:415-30.
[21] Laguna-Bercero MA. Recent advances in high temperature electrolysis using solid oxide fuel cells: A review. J Power Sources. 2012;203:4-16.
[22] Hawkes GL, O'Brien JE, Stoots CM, Herring JS, Shahnam M. Computational fluid dynamics model of a planar solid-oxide electrolysis cell for hydrogen production from nuclear energy. Nucl Technol. 2007;158:132-44.
[23] Herring JS, O'Brien JE, Stoots CM, Hawkes GL, Hartvigsen JJ, Shahnam M. Progress in high-temperature electrolysis for hydrogen production using planar SOFC technology. Int J Hydrogen Energ. 2007;32:440-50.
[24] Liu MY, Yu B, Xu JM, Chen J. Thermodynamic analysis of the efficiency of high-temperature steam electrolysis system for hydrogen production. J Power Sources. 2008;177:493-9.
[25] Liu MY, Yu B, Xu JM, Chen J. Two-dimensional simulation and critical efficiency analysis of high-temperature steam electrolysis system for hydrogen production. J Power Sources. 2008;183:708-12.
[26] Perdikaris N, Panopoulos KD, Hofmann P, Spyrakis S, Kakaras E. Design and exergetic analysis of a novel carbon free tri-generation system for hydrogen, power and heat production from natural gas, based on combined solid oxide fuel and electrolyser cells. Int J Hydrogen Energ. 2010;35:2446-56.
[27] Strazza C, Del Borghi A, Costamagna P, Traverso A, Santin M. Comparative LCA of methanol-fuelled SOFCs as auxiliary power systems on-board ships. Appl Energ. 2010;87:1670-8.

[28] Elder R, Allen R. Nuclear heat for hydrogen production: Coupling a very high/high temperature reactor to a hydrogen production plant. Progress in Nuclear Energy. 2009;51:500-25.
[29] Eguchi K, Hatagishi T, Arai H. Power generation and steam electrolysis characteristics of an electrochemical cell with a zirconia- or ceria-based electrolyte. Solid State Ionics. 1996;86-8:1245-9.
[30] Momma A, Kaga Y, Takano K, Nozaki K, Negishi A, Kato K, et al. Experimental investigation of anodic gaseous concentration of a practical seal-less solid oxide fuel cell. J Power Sources. 2005;145:169-77.
[31] Kim-Lohsoontorn P, Laosiripojana N, Bae J. Performance of solid oxide electrolysis cell having bi-layered electrolyte during steam electrolysis and carbon dioxide electrolysis. Curr Appl Phys. 2011;11:S223-S8.
[32] Minh NQ, Mogensen MB. Reversible Solid Oxide Fuel Cell Technology for Green Fuel and Power Production. The Electrochemical Society's INTERFACE. 2013;22:7.
[33] Laguna-Bercero MA, Campana R, Larrea A, Kilner JA, Orera VM. Steam Electrolysis Using a Microtubular Solid Oxide Fuel Cell. J Electrochem Soc. 2010;157:B852-B5.
[34] Zhu B, Albinsson I, Andersson C, Borsand K, Nilsson M, Mellander B-E. Electrolysis studies based on ceria-based composites. Electrochem Commun. 2006;8:495-8.
[35] Chauveau F, Mougin J, Bassat JM, Mauvy F, Grenier JC. A new anode material for solid oxide electrolyser: The neodymium nickelate Nd(2)NiO(4+delta). J Power Sources. 2010;195:744-9.
[36] Jensen SH, Sun XF, Ebbesen SD, Knibbe R, Mogensen M. Hydrogen and synthetic fuel production using pressurized solid oxide electrolysis cells. Int J Hydrogen Energ. 2010;35:9544-9.
[37] Liu Q, Yang C, Dong X, Chen F. Perovskite Sr2Fe1.5Mo0.5O6−δ as electrode materials for symmetrical solid oxide electrolysis cells. Int J Hydrogen Energ. 2010;35:10039-44.
[38] Laguna-Bercero MA, Kinadjan N, Sayers R, El Shinawi H, Greaves C, Skinner SJ. Performance of La(2-x)Sr(x)Co(0.5)Ni(0.5)O(4 +/-delta) as an Oxygen Electrode for Solid Oxide Reversible Cells. Fuel Cells. 2011;11:102-7.
[39] Kim-Lohsoontorn P, Brett DJL, Laosiripojana N, Kim YM, Bae JM. Performance of solid oxide electrolysis cells based on composite La0.8Sr0.2MnO3−δ – yttria stabilized zirconia and Ba0.5Sr0.5Co0.8Fe0.2O3−δ oxygen electrodes. Int J Hydrogen Energ. 2010;35:3958-66.
[40] He F, Song D, Peng RR, Meng GY, Yang SF. Electrode performance and analysis of reversible solid oxide fuel cells with proton conducting

electrolyte of BaCe(0.5)Zr(0.3)Y(0.2)O(3-delta). J Power Sources. 2010;195:3359-64.
[41] Schiller G, Ansar A, Lang M, Patz O. High temperature water electrolysis using metal supported solid oxide electrolyser cells (SOEC). J Appl Electrochem. 2009;39:293-301.
[42] Yu B, Zhang WQ, Xu JM, Chen J. Microstructural characterization and electrochemical properties of Ba(0.5)Sr(0.5)Co(0.8)Fe(0.2)O(3-delta) and its application for anode of SOEC. Int J Hydrogen Energ. 2008;33:6873-7.
[43] Liang M, Yu B, Wen M, Chen J, Xu J, Zhai Y. Preparation of LSM–YSZ composite powder for anode of solid oxide electrolysis cell and its activation mechanism. J Power Sources. 2009;190:341-5.
[44] Laguna-Bercero MA, Skinner SJ, Kilner JA. Performance of solid oxide electrolysis cells based on scandia stabilised zirconia. J Power Sources. 2009;192:126-31.
[45] Brisse A, Schefold J, Zahid M. High temperature water electrolysis in solid oxide cells. Int J Hydrogen Energ. 2008;33:5375-82.
[46] Bidrawn F, Kim G, Corre G, Irvine JTS, Vohs JM, Gorte RJ. Efficient reduction of CO(2) in a solid oxide electrolyzer. Electrochem Solid St. 2008;11:B167-B70.
[47] Wang WS, Huang YY, Jung SW, Vohs JM, Gorte RJ. A comparison of LSM, LSF, and LSCo for solid oxide electrolyzer anodes. J Electrochem Soc. 2006;153:A2066-A70.
[48] Ni M, Leung MKH, Leung DC. A modeling study on concentration overpotentials of a reversible solid oxide fuel cell. J Power Sources. 2006;163:460-6.
[49] Yang C, Jin C, Coffin A, Chen F. Characterization of infiltrated (La0.75Sr0.25)0.95MnO3 as oxygen electrode for solid oxide electrolysis cells. Int J Hydrogen Energ. 2010;35:5187-93.
[50] Hjalmarsson P, Sun X, Liu Y-L, Chen M. Durability of high performance Ni–yttria stabilized zirconia supported solid oxide electrolysis cells at high current density. J Power Sources. 2014;262:316-22.
[51] Laguna-Bercero MA, Hanifi AR, Monzon H, Cunningham J, Etsell TH, Sarkar P. High performance of microtubular solid oxide fuel cells using Nd2NiO4+[small delta]-based composite cathodes. Journal of Materials Chemistry A. 2014;2:9764-70.
[52] Elangovan S, Hartvigsen JJ, Frost LJ. Intermediate temperature reversible fuel cells. International Journal of Applied Ceramic Technology. 2007;4:109-18.
[53] Mori M, Abe T, Itoh H, Yamamoto O, Takeda Y, Kawahara T. Cubic-stabilized zirconia and alumina composites as electrolytes in planar type solid oxide fuel cells. Solid State Ionics. 1994;74:157-64.

[54] Badwal SPS, Ciacchi FT, Milosevic D. Scandia–zirconia electrolytes for intermediate temperature solid oxide fuel cell operation. Solid State Ionics. 2000;136–137:91-9.
[55] Stevenson JW, Hasinska K, Canfield NL, Armstrong TR. Influence of Cobalt and Iron Additions on the Electrical and Thermal Properties of (La , Sr) (Ga , Mg) O 3 − δ. J Electrochem Soc. 2000;147:3213-8.
[56] Kharton VV, Figueiredo FM, Navarro L, Naumovich EN, Kovalevsky AV, Yaremchenko AA, et al. Ceria-based materials for solid oxide fuel cells. J Mater Sci. 2001;36:1105-17.
[57] Stevenson JW, Armstrong TR, Pederson LR, Li J, Lewinsohn CA, Baskaran S. Effect of A-site cation nonstoichiometry on the properties of doped lanthanum gallate. Solid State Ionics. 1998;113–115:571-83.
[58] Kharton VV, Marques FMB, Atkinson A. Transport properties of solid oxide electrolyte ceramics: a brief review. Solid State Ionics. 2004;174:135-49.
[59] Dailly J, Fourcade S, Largeteau A, Mauvy F, Grenier JC, Marrony M. Perovskite and A(2)MO(4)-type oxides as new cathode materials for protonic solid oxide fuel cells. Electrochim Acta. 2010;55:5847-53.
[60] Osada N, Uchida H, Watanabe M. Polarization behavior of SDC cathode with highly dispersed Ni catalysts for solid oxide electrolysis cells. J Electrochem Soc. 2006;153:A816-A20.
[61] Wang ZW, Mori M. SOFC-SOEC Characteristics of an Intermediate-temperature Micro-tubular Ceramic Reactor Using Ag for Current Collecting. Electrochemistry. 2010;78:601-5.
[62] O'Brien JE, Stoots CM, Herring JS, Hartvigsen J. Hydrogen production performance of a 10-cell planar solid-oxide electrolysis stack. J Fuel Cell Sci Tech. 2006;3:213-9.
[63] Sasaki K, Susuki K, Iyoshi A, Uchimura M, Imamura N, Kusaba H, et al. H2S Poisoning of Solid Oxide Fuel Cells. J Electrochem Soc. 2006;153:A2023-A9.
[64] Gong M, Liu X, Trembly J, Johnson C. Sulfur-tolerant anode materials for solid oxide fuel cell application. J Power Sources. 2007;168:289-98.
[65] Badwal SPS, Ciacchi FT, Drennan J. Investigation of the stability of ceria-gadolinia electrolytes in solid oxide fuel cell environments. Solid State Ionics. 1999;121:253-62.
[66] Zhu S, Wang Y, Rao Y, Zhan Z, Xia C. Chemically-induced mechanical unstability of samaria-doped ceria electrolyte for solid oxide electrolysis cells. Int J Hydrogen Energ. 2014;39:12440-7.
[67] Maffei N, Kuriakose AK. Solid oxide fuel cells of ceria doped with gadolinium and praseodymium. Solid State Ionics. 1998;107:67-71.
[68] Kim-Lohsoontorn P, Bae J. Electrochemical performance of solid oxide electrolysis cell electrodes under high-temperature coelectrolysis of steam and carbon dioxide. J Power Sources. 2011;196:7161-8.

[69] Kim-Lohsoontorn P, Kim YM, Laosiripojana N, Bae J. Gadolinium doped ceria-impregnated nickel-yttria stabilised zirconia cathode for solid oxide electrolysis cell. Int J Hydrogen Energ. 2011;36:9420-7.
[70] Huang KQ, Feng M, Goodenough JB, Milliken C. Electrode performance test on single ceramic fuel cells using as electrolyte Sr- and Mg-doped LaGaO3. J Electrochem Soc. 1997;144:3620-4.
[71] Maffei N, de Silveira G. Interfacial layers in tape cast anode-supported doped lanthanum gallate SOFC elements. Solid State Ionics. 2003;159:209-16.
[72] Haile SM. Fuel cell materials and components. Acta Materialia. 2003;51:5981-6000.
[73] Steele BCH, Heinzel A. Materials for fuel-cell technologies. Nature. 2001;414:345-52.
[74] Yamamoto O. Solid oxide fuel cells: fundamental aspects and prospects. Electrochim Acta. 2000;45:2423-35.
[75] Ishihara T, Jirathiwathanakul N, Zhong H. Intermediate temperature solid oxide electrolysis cell using LaGaO3 based perovskite electrolyte. Energ Environ Sci. 2010;3:665-72.
[76] Jardiel T, Caldes MT, Moser F, Hamon J, Gauthier G, Joubert O. New SOFC electrode materials: The Ni-substituted LSCM-based compounds La0.75Sr0.25)(Cr0.5Mn0.5-x Ni-x)O-3 (-) (delta) and (La0.75Sr0.25)(Cr0.5- xNixMn0.5)O-3 (- delta). Solid State Ionics. 2010;181:894-901.
[77] Delahaye T, Jardiel T, Joubert O, Laucournet R, Gauthier G, Caldes MT. Electrochemical properties of novel SOFC dual electrode La0.75Sr0.25Cr0.5Mn0.3Ni0.2O3 (-) (delta). Solid State Ionics. 2011;184:39-41.
[78] Zhu X, Lü Z, Wei B, Huang X, Zhang Y, Su W. A symmetrical solid oxide fuel cell prepared by dry-pressing and impregnating methods. J Power Sources. 2011;196:729-33.
[79] Gopalan S, Virkar AV. Thermodynamic Stabilities of SrCeO3 and BaCeO3 Using a Molten Salt Method and Galvanic Cells. J Electrochem Soc. 1993;140:1060-5.
[80] Iwahara H, Yajima T, Hibino T, Ushida H. Performance of Solid Oxide Fuel Cell Using Proton and Oxide Ion Mixed Conductors Based on BaCe1 − x Sm x O 3 − α. J Electrochem Soc. 1993;140:1687-91.
[81] Ryu KH, Haile SM. Chemical stability and proton conductivity of doped BaCeO3–BaZrO3 solid solutions. Solid State Ionics. 1999;125:355-67.
[82] Stuart PA, Unno T, Kilner JA, Skinner SJ. Solid oxide proton conducting steam electrolysers. Solid State Ionics. 2008;179:1120-4.

[83] Norby T. Proton Conductivity in Perovskite Oxides. In: Ishihara T, editor. Perovskite Oxide for Solid Oxide Fuel Cells: Springer US; 2009. p. 217-41.
[84] Liu QA, Dong XH, Xiao GL, Zhao F, Chen FL. A Novel Electrode Material for Symmetrical SOFCs. Adv Mater. 2010;22:5478-82.
[85] Lee S, Kim JM, Hong HS, Woo SK. Fabrication and characterization of Cu/YSZ cermet high temperature electrolysis cathode material prepared by high-energy ball-milling method II. 700 degrees C-sintered. J Alloy Compd. 2009;467:614-21.
[86] Kharton VV, Tsipis EV, Naumovich EN, Thursfield A, Patrakeev MV, Kolotygin VA, et al. Mixed conductivity, oxygen permeability and redox behavior of K2NiF4-type La2Ni0.9Fe0.1O4+δ. J Solid State Chem. 2008;181:1425-33.
[87] Wang W, Gorte RJ, Vohs JM. Analysis of the performance of the electrodes in a natural gas assisted steam electrolysis cell. Chem Eng Sci. 2008;63:765-9.
[88] Tietz F, Buchkremer HP, Stöver D. Components manufacturing for solid oxide fuel cells. Solid State Ionics. 2002;152–153:373-81.
[89] Kaiser A, Monreal E, Stolten D. Preparation Techniques and Materials For Long Term Stable SOFC - Single Cell Membranes. Ionics. 1997;3:143-8.
[90] Razavi Hesabi Z, Mazaheri M, Ebadzadeh T. Enhanced electrical conductivity of ultrafine-grained 8Y2O3 stabilized ZrO2 produced by two-step sintering technique. J Alloy Compd. 2010;494:362-5.
[91] Bellino MG, Lamas DG, Walsoe de Reca NE. Preparation and ionic transport properties of YDC-YSZ nanocomposites. J Mater Chem. 2008;18:4537-42.
[92] Esposito V, Traversa E. Design of Electroceramics for Solid Oxides Fuel Cell Applications: Playing with Ceria. J Am Ceram Soc. 2008;91:1037-51.
[93] Tran TB, Hayun S, Navrotsky A, Castro RHR. Transparent Nanocrystalline Pure and Ca-Doped MgO by Spark Plasma Sintering of Anhydrous Nanoparticles. J Am Ceram Soc. 2012;95:1185-8.
[94] Dahl P, Kaus I, Zhao Z, Johnsson M, Nygren M, Wiik K, et al. Densification and properties of zirconia prepared by three different sintering techniques. Ceramics International. 2007;33:1603-10.
[95] Weibel A, Bouchet R, Denoyel R, Knauth P. Hot pressing of nanocrystalline TiO2 (anatase) ceramics with controlled microstructure. J Eur Ceram Soc. 2007;27:2641-6.
[96] Chen IW, Wang XH. Sintering dense nanocrystalline ceramics without final-stage grain growth. Nature. 2000;404:168-71.
[97] Harmer MP, Brook RJ. Fast Firing-Microstructural Benefits. Trans J Brit Ceram Soc. 1981;5:147-8.

[98] Chiang YM, Birnie DP, Kingery WD. Physical Ceramics: Principles for Ceramic Science and Engineering: Wiley; 1996.
[99] Garcia DE, Klein AN, Hotza D. Advanced ceramics with dense and fine-grained microstructures through fast firing. Reviews on Advanced Materials Science. 2012;30:273-81.
[100] Atkinson A, Barnett S, Gorte RJ, Irvine JTS, McEvoy AJ, Mogensen M, et al. Advanced anodes for high-temperature fuel cells. Nat Mater. 2004;3:17-27.
[101] Ma Q, Tietz F. Comparison of Y and La-substituted SrTiO3 as the anode materials for SOFCs. Solid State Ionics. 2012;225:108-12.
[102] Hauch A, Ebbesen SD, Jensen SH, Mogensen M. Highly efficient high temperature electrolysis. J Mater Chem. 2008;18:2331-40.
[103] Hauch A, Jensen SH, Bilde-Sorensen JB, Mogensen M. Silica segregation in the Ni/YSZ electrode. J Electrochem Soc. 2007;154:A619-A26.
[104] Hauch A, Ebbesen SD, Jensen SH, Mogensen M. Solid oxide electrolysis cells: Microstructure and degradation of the Ni/yttria-stabilized zirconia electrode. J Electrochem Soc. 2008;155:B1184-B93.
[105] Knibbe R, Traulsen ML, Hauch A, Ebbesen SD, Mogensen M. Solid Oxide Electrolysis Cells: Degradation at High Current Densities. J Electrochem Soc. 2010;157:B1209-B17.
[106] Chen M, Liu Y-L, Bentzen JJ, Zhang W, Sun X, Hauch A, et al. Microstructural Degradation of Ni/YSZ Electrodes in Solid Oxide Electrolysis Cells under High Current. J Electrochem Soc. 2013;160:F883-F91.
[107] Menzler N, Tietz F, Uhlenbruck S, Buchkremer H, Stöver D. Materials and manufacturing technologies for solid oxide fuel cells. J Mater Sci. 2010;45:3109-35.
[108] Sohal MS, O'Brien JE, Stoots CM, Sharma VI, Yildiz B, Virkar A. Degradation Issues in Solid Oxide Cells During High Temperature Electrolysis. J Fuel Cell Sci Tech. 2012;9.
[109] Wiedenmann D, Hauch A, Grobety B, Mogensen M, Vogt UF. Complementary techniques for solid oxide electrolysis cell characterisation at the micro- and nano-scale. Int J Hydrogen Energ. 2010;35:5053-60.
[110] Li Q, Zheng Y, Guan W, Jin L, Xu C, Wang WG. Achieving high-efficiency hydrogen production using planar solid-oxide electrolysis stacks. Int J Hydrogen Energ. 2014;39:10833-42.
[111] Keane M, Mahapatra MK, Verma A, Singh P. LSM–YSZ interactions and anode delamination in solid oxide electrolysis cells. Int J Hydrogen Energ. 2012;37:16776-85.
[112] Sun X, Chen M, Liu Y-L, Hjalmarsson P, Ebbesen SD, Jensen SH, et al. Durability of Solid Oxide Electrolysis Cells for Syngas Production. J Electrochem Soc. 2013;160:F1074-F80.

[113] Ruiz-Morales JC, Canales-Vazquez J, Marrero-Lopez D, Pena-Martinez J, Tarancon A, Irvine JTS, et al. Is YSZ stable in the presence of Cu? J Mater Chem. 2008;18:5072-7.
[114] Jiang SP. A review of wet impregnation—An alternative method for the fabrication of high performance and nano-structured electrodes of solid oxide fuel cells. Materials Science and Engineering: A. 2006;418:199-210.
[115] Pujare NU, Semkow KW, Sommells AF. A Direct H_2S / Air Solid Oxide Fuel Cell. J Electrochem Soc. 1987;134:2639-40.
[116] Pujare NU, Tsai KJ, Sammells AF. An Electrochemical Claus Process for Sulfur Recovery. J Electrochem Soc. 1989;136:3662-78.
[117] Yates C, Winnick J. Anode Materials for a Hydrogen Sulfide Solid Oxide Fuel Cell. J Electrochem Soc. 1999;146:2841-4.
[118] Liu M, Wei G, Luo J, Sanger AR, Chuang KT. Use of Metal Sulfides as Anode Catalysts in H_2S -Air SOFCs. J Electrochem Soc. 2003;150:A1025-A9.
[119] Wei G-L, Luo J-L, Sanger AR, Chuang KT. High-Performance Anode for H_2S - Air SOFCs. J Electrochem Soc. 2004;151:A232-A7.
[120] Blinn KS, Liu M. $BaZr_{0.9}Yb_{0.1}O_{3-\delta}$-modified bi-electrode supported solid oxide fuel cells with enhanced coking and sulfur tolerance. J Power Sources. 2013;243:24-8.
[121] Yoon SP, Han J, Nam SW, Lim T-H, Hong S-A. Improvement of anode performance by surface modification for solid oxide fuel cell running on hydrocarbon fuel. J Power Sources. 2004;136:30-6.
[122] Jung I, Lee D, Lee SO, Kim D, Kim J, Hyun S-H, et al. LSCM–YSZ nanocomposites for a high performance SOFC anode. Ceramics International. 2013;39:9753-8.
[123] Park S, Vohs JM, Gorte RJ. Direct oxidation of hydrocarbons in a solid-oxide fuel cell. Nature. 2000;404:265-7.
[124] Boder M, Dittmeyer R. Catalytic modification of conventional SOFC anodes with a view to reducing their activity for direct internal reforming of natural gas. J Power Sources. 2006;155:13-22.
[125] Flytzani-Stephanopoulos M, Sakbodin M, Wang Z. Regenerative Adsorption and Removal of H2S from Hot Fuel Gas Streams by Rare Earth Oxides. Science. 2006;312:1508-10.
[126] Devianto H, Yoon SP, Nam SW, Han J, Lim T-H. The effect of a ceria coating on the H2S tolerance of a molten carbonate fuel cell. J Power Sources. 2006;159:1147-52.
[127] Gorte RJ, Kim H, Vohs JM. Novel SOFC anodes for the direct electrochemical oxidation of hydrocarbon. J Power Sources. 2002;106:10-5.
[128] Fuerte A, Valenzuela RX, Escudero MJ, Daza L. Study of a SOFC with a bimetallic Cu–Co–ceria anode directly fuelled with simulated biogas mixtures. Int J Hydrogen Energ.

[129] Trembly JP, Marquez AI, Ohrn TR, Bayless DJ. Effects of coal syngas and H2S on the performance of solid oxide fuel cells: Single-cell tests. J Power Sources. 2006;158:263-73.
[130] Aravind PV, Ouweltjes JP, de Heer E, Woudstra N, Rietveld G. Impact of Biosyngas and its components on SOFC Anodes. Electrochemical Society Proceedings 2005;7:1459-67.
[131] Ishihara T, Shibayama T, Nishiguchi H, Takita Y. Nickel–Gd-doped CeO2 cermet anode for intermediate temperature operating solid oxide fuel cells using LaGaO3-based perovskite electrolyte. Solid State Ionics. 2000;132:209-16.
[132] Jiang SP, Zhang S, Zhen YD, Koh AP. Performance of GDC-Impregnated Ni Anodes of SOFCs. Electrochemical and Solid-State Letters. 2004;7:A282-A5.
[133] Nurk G, Huthwelker T, Braun A, Ludwig C, Lust E, Struis RPWJ. Redox dynamics of sulphur with Ni/GDC anode during SOFC operation at mid- and low-range temperatures: An operando S K-edge XANES study. J Power Sources. 2013;240:448-57.
[134] Tomita A, Tsunekawa K, Hibino T, Teranishi S, Tachi Y, Sano M. Chemical and redox stabilities of a solid oxide fuel cell with BaCe0.8Y0.2O3−α functioning as an electrolyte and as an anode. Solid State Ionics. 2006;177:2951-6.
[135] Mukundan R, Brosha EL, Garzon FH. Sulfur Tolerant Anodes for SOFCs. Electrochemical and Solid-State Letters. 2004;7:A5-A7.
[136] Yang L, Wang S, Blinn K, Liu M, Liu Z, Cheng Z, et al. Enhanced Sulfur and Coking Tolerance of a Mixed Ion Conductor for SOFCs: BaZr0.1Ce0.7Y0.2–xYbxO3–δ. Science. 2009;326:126-9.
[137] Huang Y-H, Dass RI, Xing Z-L, Goodenough JB. Double Perovskites as Anode Materials for Solid-Oxide Fuel Cells. Science. 2006;312:254-7.
[138] Jiang SP, Ab LZ, Zhang Y. Lanthanum strontium manganese chromite cathode and anode synthesized by gel-casting for solid oxide fuel cells. J Mater Chem. 2007;17:2627-35.
[139] Ruiz-Morales JC, Canales-Vázquez J, Peña-Martínez J, López DM, Núñez P. On the simultaneous use of La0.75Sr0.25Cr0.5Mn0.5O3−δ as both anode and cathode material with improved microstructure in solid oxide fuel cells. Electrochim Acta. 2006;52:278-84.
[140] Tao S, Irvine JTS. A redox-stable efficient anode for solid-oxide fuel cells. Nat Mater. 2003;2:320-3.
[141] Bastidas DM, Tao SW, Irvine JTS. A symmetrical solid oxide fuel cell demonstrating redox stable perovskite electrodes. J Mater Chem. 2006;16:1603-5.
[142] Reyes-Rojas A, Alvarado-Flores J, Esparza-Ponce H, Esneider-Alcala M, Espitia-Cabrera I, Torres-Moye E. Symmetry breaking and electrical

conductivity of La0.7Sr0.3Cr0.4Mn0.6O3-delta perovskite as SOFC anode material. Materials Chemistry and Physics. 2011;126:773-9.
[143] Li YX, Gan Y, Wang Y, Xie K, Wu YC. Composite cathode based on Ni-loaded La0.75Sr0.25Cr0.5Mn0.5O3-delta for direct steam electrolysis in an oxide-ion-conducting solid oxide electrolyzer. Int J Hydrogen Energ. 2013;38:10196-207.
[144] Yang X, Irvine JTS. (La0.75Sr0.25)(0.95)Mn0.5Cr0.5O3 as the cathode of solid oxide electrolysis cells for high temperature hydrogen production from steam. J Mater Chem. 2008;18:2349-54.
[145] van den Bossche M, Matthews R, Lichtenberger A, McIntosh S. Insights Into the Fuel Oxidation Mechanism of La0.75Sr0.25Cr0.5Mn0.5O3-delta SOFC Anodes. J Electrochem Soc. 2010;157:B392-B9.
[146] Hashimoto S, Kindermann L, Poulsen FW, Mogensen M. A study on the structural and electrical properties of lanthanum-doped strontium titanate prepared in air. J Alloy Compd. 2005;397:245-9.
[147] Canales-Vázquez J, Tao SW, Irvine JTS. Electrical properties in La2Sr4Ti6O19−δ: a potential anode for high temperature fuel cells. Solid State Ionics. 2003;159:159-65.
[148] Marina OA, Canfield NL, Stevenson JW. Thermal, electrical, and electrocatalytical properties of lanthanum-doped strontium titanate. Solid State Ionics. 2002;149:21-8.
[149] Fu QX, Mi SB, Wessel E, Tietz F. Influence of sintering conditions on microstructure and electrical conductivity of yttrium-substituted SrTiO3. J Eur Ceram Soc. 2008;28:811-20.
[150] Ma Q, Tietz F, Stöver D. Nonstoichiometric Y-substituted SrTiO3 materials as anodes for solid oxide fuel cells. Solid State Ionics. 2011;192:535-9.
[151] Kolodiazhnyi T, Petric A. The Applicability of Sr-deficient n-type SrTiO3 for SOFC Anodes. J Electroceram. 2005;15:5-11.
[152] Blennow P, Hagen A, Hansen KK, Wallenberg LR, Mogensen M. Defect and electrical transport properties of Nb-doped SrTiO3. Solid State Ionics. 2008;179:2047-58.
[153] Yoo KB, Choi GM. Performance of La-doped strontium titanate (LST) anode on LaGaO3-based SOFC. Solid State Ionics. 2009;180:867-71.
[154] Smith BH, Holler WC, Gross MD. Electrical properties and redox stability of tantalum-doped strontium titanate for SOFC anodes. Solid State Ionics. 2011;192:383-6.
[155] Li SS, Li YX, Gan Y, Xie K, Meng GY. Electrolysis of H2O and CO2 in an oxygen-ion conducting solid oxide electrolyzer with a La0.2Sr0.8TiO3+delta composite cathode. J Power Sources. 2012;218:244-9.

[156] Zhang J, Xie K, Gan Y, Wu GJ, Ding B, Zhang Y, et al. Composite titanate cathode enhanced with in situ grown nickel nanocatalyst for direct steam electrolysis. New Journal of Chemistry. 2014;38:3434-42.
[157] Hong HS, Chae US, Choo ST. The effect of ball milling parameters and Ni concentration on a YSZ-coated Ni composite for a high temperature electrolysis cathode. J Alloy Compd. 2008;449:331-4.
[158] Liu MY, Yu B, Xu JM, Chen J. Influence of pore formers on physical properties and microstructures of supporting cathodes of solid oxide electrolysis cells. Int J Hydrogen Energ. 2010;35:2670-4.
[159] Mielewczyk-Gryn A, Gdula K, Molin S, Jasinski P, Kusz B, Gazda M. Structure and electrical properties of ceramic proton conductors obtained with molten-salt and solid-state synthesis methods. J Non-Cryst Solids. 2010;356:1976-9.
[160] Gamble S. Fabrication-microstructure-performance relationships of reversible solid oxide fuel cell electrodes-review. Mater Sci Tech-Lond. 2011;27:1485-97.
[161] Ni M. Modeling of a solid oxide electrolysis cell for carbon dioxide electrolysis. Chem Eng J. 2010;164:246-54.
[162] Pratihar SK, Sharma AD, Maiti HS. Electrical behavior of nickel coated YSZ cermet prepared by electroless coating technique. Materials Chemistry and Physics. 2006;96:388-95.
[163] Ni M, Leung MKH, Leung DYC. Mathematical modeling of the coupled transport and electrochemical reactions in solid oxide steam electrolyzer for hydrogen production. Electrochim Acta. 2007;52:6707-18.
[164] Clemmer RMC, Corbin SF. Influence of porous composite microstructure on the processing and properties of solid oxide fuel cell anodes. Solid State Ionics. 2004;166:251-9.
[165] Bertei A, Nicolella C. Percolation theory in SOFC composite electrodes: Effects of porosity and particle size distribution on effective properties. J Power Sources. 2011;196:9429-36.
[166] Takeda Y, Kanno R, Noda M, Tomida Y, Yamamoto O. Cathodic Polarization Phenomena of Perovskite Oxide Electrodes with Stabilized Zirconia. J Electrochem Soc. 1987;134:2656-61.
[167] Chen K, Ai N, Jiang SP. Performance and structural stability of Gd0.2Ce0.8O1.9 infiltrated La0.8Sr0.2MnO3 nano-structured oxygen electrodes of solid oxide electrolysis cells. Int J Hydrogen Energ. 2014;39:10349-58.
[168] Chen K, Ai N, Jiang SP. Reasons for the high stability of nano-structured (La,Sr)MnO3 infiltrated Y2O3–ZrO2 composite oxygen electrodes of solid oxide electrolysis cells. Electrochem Commun. 2012;19:119-22.

[169] Bernuy-Lopez C, Knibbe R, He Z, Mao X, Hauch A, Nielsen KA. Electrochemical characterisation of solid oxide cell electrodes for hydrogen production. J Power Sources. 2011;196:4396-403.
[170] Chen K, Ai N, Jiang SP. Enhanced electrochemical performance and stability of (La,Sr)MnO3–(Gd,Ce)O2 oxygen electrodes of solid oxide electrolysis cells by palladium infiltration. Int J Hydrogen Energ. 2012;37:1301-10.
[171] Ai N, Chen K, Liu S, Jiang SP. Performance and stability of nano-structured Pd and Pd0.95M0.05 (M = Mn, Co, Ce, and Gd) infiltrated Y2O3–ZrO2 oxygen electrodes of solid oxide electrolysis cells. Int J Hydrogen Energ. 2013;38:16569-78.
[172] Jiang SP. Nanoscale and nano-structured electrodes of solid oxide fuel cells by infiltration: Advances and challenges. Int J Hydrogen Energ. 2012;37:449-70.
[173] Kim G, Wang S, Jacobson AJ, Reimus L, Brodersen P, Mims CA. Rapid oxygen ion diffusion and surface exchange kinetics in PrBaCo2O5+x with a perovskite related structure and ordered A cations. J Mater Chem. 2007;17:2500-5.
[174] Mauvy F, Lalanne C, Bassat J-M, Grenier J-C, Zhao H, Huo L, et al. Electrode properties of Ln2NiO4 + δ (Ln = La, Nd, Pr): AC Impedance and DC Polarization Studies. J Electrochem Soc. 2006;153:A1547-A53.
[175] Tarancon A, Skinner SJ, Chater RJ, Hernandez-Ramirez F, Kilner JA. Layered perovskites as promising cathodes for intermediate temperature solid oxide fuel cells. J Mater Chem. 2007;17:3175-81.
[176] Meng X, Liu X, Han D, Wu H, Li J, Zhan Z. Symmetrical solid oxide fuel cells with impregnated SrFe0.75Mo0.25O3−δ electrodes. J Power Sources. 2014;252:58-63.
[177] Marina OA, Pederson LR, Williams MC, Coffey GW, Meinhardt KD, Nguyen CD, et al. Electrode Performance in Reversible Solid Oxide Fuel Cells. J Electrochem Soc. 2007;154:B452-B9.
[178] Hansen KK, Hansen KV. A-site deficient (La0.6Sr0.4)1−sFe0.8Co0.2O3−δ perovskites as SOFC cathodes. Solid State Ionics. 2007;178:1379-84.
[179] Fu C, Sun K, Zhang N, Chen X, Zhou D. Electrochemical characteristics of LSCF–SDC composite cathode for intermediate temperature SOFC. Electrochim Acta. 2007;52:4589-94.
[180] Xia C, Rauch W, Chen F, Liu M. Sm0.5Sr0.5CoO3 cathodes for low-temperature SOFCs. Solid State Ionics. 2002;149:11-9.
[181] Tietz F, Sebold D, Brisse A, Schefold J. Degradation phenomena in a solid oxide electrolysis cell after 9000 h of operation. J Power Sources. 2013;223:129-35.

[182] Tarancon A, Burriel M, Santiso J, Skinner SJ, Kilner JA. Advances in layered oxide cathodes for intermediate temperature solid oxide fuel cells. J Mater Chem. 2010;20:3799-813.
[183] Zhang Y, Chen K, Xia C, Jiang SP, Ni M. A model for the delamination kinetics of La0.8Sr0.2MnO3 oxygen electrodes of solid oxide electrolysis cells. Int J Hydrogen Energ. 2012;37:13914-20.
[184] Chen K, Lü Z, Chen X, Ai N, Huang X, Du X, et al. Development of LSM-based cathodes for solid oxide fuel cells based on YSZ films. J Power Sources. 2007;172:742-8.
[185] Wang J, Zhang Y, Liang T, Deng C, Xu J. Effect of oxygen partial pressure on the electrochemical impedance of La0.8Sr0.2MnO3−δ/Zr0.92Y0.08O2 porous composite anodes in solid oxide electrolysis cell. J Power Sources. 2012;208:415-20.
[186] Minh NQ. Development of Reversible Solid Oxide Fuel Cells (RSOFCs)and Stacks. ECS Transactions. 2011;35:2897-904.
[187] Mougin J, Chatroux A, Couturier K, Petitjean M, Reytier M, Gousseau G, et al. High Temperature Steam Electrolysis Stack with Enhanced Performance and Durability. Energy Procedia. 2012;29:445-54.
[188] Hughes GA, Yakal-Kremski K, Barnett SA. Life testing of LSM-YSZ composite electrodes under reversing-current operation. Physical Chemistry Chemical Physics. 2013;15:17257-62.
[189] Virkar AV. Mechanism of oxygen electrode delamination in solid oxide electrolyzer cells. Int J Hydrogen Energ. 2010;35:9527-43.
[190] Mawdsley JR, David Carter J, Jeremy Kropf A, Yildiz B, Maroni VA. Post-test evaluation of oxygen electrodes from solid oxide electrolysis stacks. Int J Hydrogen Energ. 2009;34:4198-207.
[191] Sharma VI, Yildiz B. Degradation Mechanism in La(0.8)Sr(0.2)CoO(3) as Contact Layer on the Solid Oxide Electrolysis Cell Anode. J Electrochem Soc. 2010;157:B441-B8.
[192] Chen K, Jiang SP. Failure mechanism of (La,Sr)MnO3 oxygen electrodes of solid oxide electrolysis cells. Int J Hydrogen Energ. 2011;36:10541-9.
[193] Lee HY, Cho WS, Oh SM, Wiemhöfer HD, Göpel W. Active Reaction Sites for Oxygen Reduction in La0.9Sr0.1MnO3 / YSZ Electrodes. J Electrochem Soc. 1995;142:2659-64.
[194] Mizusaki J, Mori N, Takai H, Yonemura Y, Minamiue H, Tagawa H, et al. Oxygen nonstoichiometry and defect equilibrium in the perovskite-type oxides La1−xSrxMnO3+d. Solid State Ionics. 2000;129:163-77.
[195] Jiang SP, Love JG. Origin of the initial polarization behavior of Sr-doped LaMnO3 for O2 reduction in solid oxide fuel cells. Solid State Ionics. 2001;138:183-90.

[196] Jiang SP, Love JG. Observation of structural change induced by cathodic polarization on (La,Sr)MnO3 electrodes of solid oxide fuel cells. Solid State Ionics. 2003;158:45-53.
[197] De Haart LGJ, Vinke IC. Long-Term Operation of Planar Type SOFC Stacks. ECS Transactions. 2011;35:187-94.
[198] Chen K, Ai N, Jiang SP. Performance and stability of (La,Sr)MnO3–Y2O3–ZrO2 composite oxygen electrodes under solid oxide electrolysis cell operation conditions. Int J Hydrogen Energ. 2012;37:10517-25.
[199] Patro PK, Delahaye T, Bouyer E. Development of Pr(0.58)Sr(0.4)Fe(0.8)Co(0.2)O(3-delta)-GDC composite cathode for solid oxide fuel cell (SOFC) application. Solid State Ionics. 2010;181:1378-86.
[200] Schuler JA, Wuillemin Z, Hessler-Wyser A, Comminges C, Steiner NY, Van herle J. Cr-poisoning in (La,Sr)(Co,Fe)O3 cathodes after 10,000 h SOFC stack testing. J Power Sources. 2012;211:177-83.
[201] Nguyen VN, Fang QP, Packbier U, Blum L. Long-term tests of a Julich planar short stack with reversible solid oxide cells in both fuel cell and electrolysis modes. Int J Hydrogen Energ. 2013;38:4281-90.
[202] Schefold J, Brisse A, Zahid M, Ouweltjes JP, Nielsen JU. Long Term Testing of Short Stacks with Solid Oxide Cells for Water Electrolysis. ECS Transactions. 2011;35:2915-27.
[203] Tao Y, Nishino H, Ashidate S, Kokubo H, Watanabe M, Uchida H. Polarization properties of La(0.6)Sr(0.4)Co(0.2)Fe(0.8)O(3)-based double layer-type oxygen electrodes for reversible SOFCs. Electrochim Acta. 2009;54:3309-15.
[204] Baumann FS, Fleig J, Konuma M, Starke U, Habermeier H-U, Maier J. Strong Performance Improvement of La0.6Sr0.4Co0.8Fe0.2O3 − δ SOFC Cathodes by Electrochemical Activation. J Electrochem Soc. 2005;152:A2074-A9.
[205] Kim SJ, Choi GM. Stability of LSCF electrode with GDC interlayer in YSZ-based solid oxide electrolysis cell. Solid State Ionics. 2014;262:303-6.
[206] Shao Z, Haile SM. A high-performance cathode for the next generation of solid-oxide fuel cells. Nature. 2004;431:170-3.
[207] Gómez SY, Gurauskis J, Øygarden V, Hotza D, Grande T, Wiik K. Synthesis and oxygen transport properties of La2-xSrxNi0.95Mo0.05O4+δ (0<x<0.4). In submission process. 2014.
[208] Boehm E, Bassat JM, Dordor P, Mauvy F, Grenier JC, Stevens P. Oxygen diffusion and transport properties in non-stoichiometric Ln2NiO4δ oxides. Solid State Ionics. 2005;176:2717-25.
[209] Sayers R, Liu J, Rustumji B, Skinner SJ. Novel K2NiF4-Type Materials for Solid Oxide Fuel Cells: Compatibility with Electrolytes in the Intermediate Temperature Range. Fuel Cells. 2008;8:338-43.

[210] Montenegro-Hernández A, Vega-Castillo J, Mogni L, Caneiro A. Thermal stability of Ln2NiO4+δ (Ln: La, Pr, Nd) and their chemical compatibility with YSZ and CGO solid electrolytes. Int J Hydrogen Energ. 2011;36:15704-14.
[211] Amow G, Whitfield PS, Davidson IJ, Hammond RP, Munnings CN, Skinner SJ. Structural and sintering characteristics of the La2Ni1−xCoxO4+δ series. Ceramics International. 2004;30:1635-9.
[212] Rieu M, Sayers R, Laguna-Bercero MA, Skinner S, Lenormand P, Ansart F. Investigations of Graded Cathodes to Improve SOFC Electrochemical Performances. ECS Transactions. 2009;25:2565-71.
[213] El Shinawi H, Greaves C. Synthesis and characterization of La1.5+xSr0.5-xCo0.5Ni0.5O4+/-[small delta] (x = 0, 0.2). J Mater Chem. 2010;20:504-11.
[214] Yuan CL, Wang SG, Song WH, Yu T, Dai JM, Ye SL, et al. Enhanced intergrain tunneling magnetoresistance in double perovskite Sr2FeMoO6 polycrystals with nanometer-scale particles. Applied Physics Letters. 1999;75:3853-5.
[215] Ruiz-Morales JC, Marrero-Lopez D, Canales-Vazquez J, Irvine JTS. Symmetric and reversible solid oxide fuel cells. Rsc Adv. 2011;1:1403-14.
[216] Xiao G, Liu Q, Zhao F, Zhang L, Xia C, Chen F. Sr2Fe1.5Mo0.5O6 as Cathodes for Intermediate-Temperature Solid Oxide Fuel Cells with La0.8Sr0.2Ga0.87Mg0.13O3 Electrolyte. J Electrochem Soc. 2011;158:B455-B60.
[217] Wright JH, Virkar AV, Liu Q, Chen F. Electrical characterization and water sensitivity of Sr2Fe1.5Mo0.5O6−δ as a possible solid oxide fuel cell electrode. J Power Sources. 2013;237:13-8.
[218] Son LH, Phuc NX, Phuc PV, Hong NM, Hong LV. Observation of phase decomposition of Sr2FeMoO6 by Raman spectroscopy. Journal of Raman Spectroscopy. 2001;32:817-20.
[219] Zhang L, Liu Y, Zhang Y, Xiao G, Chen F, Xia C. Enhancement in surface exchange coefficient and electrochemical performance of Sr2Fe1.5Mo0.5O6 electrodes by Ce0.8Sm0.2O1.9 nanoparticles. Electrochem Commun. 2011;13:711-3.
[220] Hou M, Sun W, Li P, Feng J, Yang G, Qiao J, et al. Investigation into the effect of molybdenum-site substitution on the performance of Sr2Fe1.5Mo0.5O6−δ for intermediate temperature solid oxide fuel cells. J Power Sources. 2014;272:759-65.
[221] Pan X, Wang Z, He B, Wang S, Wu X, Xia C. Effect of Co doping on the electrochemical properties of Sr2Fe1.5Mo0.5O6 electrode for solid oxide fuel cell. Int J Hydrogen Energ. 2013;38:4108-15.
[222] Caneiro A, Mogni L, Grunbaum N, Prado F. Physicochemical properties of non-stoichiometric oxides. J Therm Anal Calorim. 2011;103:597-606.

[223] Prestat M, Morandi A, Heel A, Holzer L, Holtappels P, Graule TJ. Effect of graphite pore former on oxygen electrodes prepared with La(0.6)Sr(0.4)CoO(3-delta) nanoparticles. Electrochem Commun. 2010;12:292-5.
[224] Bartonickova E, Wiik K, Maca K, Lein HL, Rudberg EA. Synthesis and oxygen transport properties of La0.2Sr0.8Fe1−xTixO3−δ (x;=0;0.2, 0.4) intended for syn-gas production. J Eur Ceram Soc. 2010;30:605-11.
[225] Nie L, Liu J, Zhang Y, Liu M. Effects of pore formers on microstructure and performance of cathode membranes for solid oxide fuel cells. J Power Sources. 2011;196:9975-9.
[226] Ni M. Computational fluid dynamics modeling of a solid oxide electrolyzer cell for hydrogen production. Int J Hydrogen Energ. 2009;34:7795-806.
[227] Sahu AK, Ghosh A, Suri AK. Characterization of porous lanthanum strontium manganite (LSM) and development of yttria stabilized zirconia (YSZ) coating. Ceramics International. 2009;35:2493-7.

3. SYNTHESIS AND OXYGEN TRANSPORT PROPERTIES OF $La_{2-y}Sr_yNi_{1-x}Mo_xO_{4+\delta}$

ABSTRACT

K_2NiF_4-type structure $La_2NiO_{4+\delta}$-based materials exhibit high oxygen permeability, ionic conductivity among other properties advantageous for several applications. In this work the synthesis and oxygen transport properties for the system $La_{2-y}Sr_yNi_{1-x}Mo_xO_{4+\delta}$ $0.0 \leq y \leq 0.4$ and $0.0 \leq x \leq 0.1$ materials are reported. The phase relations analysis disclose low Mo solubility limit on the B-site. Single phase $La_{1.8}Sr_{0.2}Ni_{0.95}Mo_{0.05}O_{4+\delta}$ bar shape samples were cold-isostatically pressed and pressureless sintered at 1500ºC for 4 h. Sintered densities above 95% and grain size of 14.3±8 μm were obtained. A simple defect model was applied to explain electrical conductivity. Surface exchange coefficients (k_{chem}) and bulk diffusion coefficients (D_{chem}) in terms of temperature and P_{O2} were assessed by electrical conductivity relaxation (ECR) and discussed comparing with similar compounds.

Keywords: Oxygen diffusion; Surface exchange; Doped Lanthanum Nickelate, Electrical Conductivity Relaxation.

3.1. INTRODUCTION

Mixed conductors derived from nickelates with K_2NiF_4-type structure, $La_2NiO_{4+\delta}$ (LNO) and doped-LNO compounds have attracted much attention as materials for solid oxide fuel cell (IT-SOFC cathodes) and ceramic membranes for oxygen separation and partial oxidation of light hydrocarbons [1-9]. The advantages of LNO-based materials include high oxygen permeability and ionic conductivity, moderate thermal and chemically induced expansion, and high electrocatalytic activity [10-13].

The intergrowth K_2NiF_4-type structure of LNO is tetragonal (space group I4/mmm or F4/mmm), described as a succession of perovskite layers alternating with rock-salt LaO sheets; can be looked as a natural heterostructures with alternating blocks of rock-salt LaO and perovskite $LaNiO_3$ layers [14-19] (see Fig 3.1). The oxygen ionic transport occurs by a complex mechanism, combining vacancy diffusion in the perovskite planes and interstitial anion migration in the rock-salt layers, where the oxygen is very mobile, this structure can accommodate oxygen excess helping the oxygen evolution [18, 20, 21].

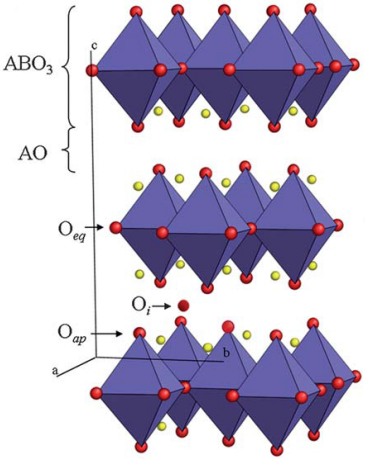

Fig 3.1. Polyhedral view of a Ruddlesden-Popper structure of general formula $A_{n+1}B_nO_{3n+1}$ consisting of $n$$ABO_3$ perovskite layers between two AO rock-salt layers. Oxygen in equatorial, apical and interstitial sites has been highlighted, adapted from [18].

3.1.1. Defect Model and Conductivity

To estimate characteristic features of the oxygen transport and conductivity of LNO based compounds, a simplified model may be considered viz. [22-24]. Assuming that the main point defects in $La_2NiO_{4+\delta}$ are interstitial oxygen ions and electron holes (originating from the presence of Ni^{2+} and Ni^{3+}) the following defect equilibria may be formulated:

$$\frac{1}{2}O_2 = O_i'' + \dot{h} \tag{3.1}$$

the corresponding equilibrium constant can be written as:

$$K_p' = \frac{[O_i''][\dot{h}]^2}{P_{O_2}^{1/2}} \tag{3.2}$$

where K_p' is a constant, assuming A^{+2} and B^{+3} in $La_{2-y}A_yNi_{1-x}B_xO_{4+\delta}$, the electroneutrality as:

$$2\left[O_i''\right]+\left[A_{La}'\right]-\left[B_{Ni}^{\bullet}\right]=\left[\dot{h}\right] \tag{3.3}$$

for the undoped compound the simplified electroneutrality condition in Eq. (3.3) is:

$$2\left[O_i''\right]=\left[\dot{h}\right] \tag{3.4}$$

substituting Eq. (3.4) into the equilibrium condition Eq. (3.2):

$$P_{O_2}^{1/2}=K_p\left[\dot{h}\right]^3 \tag{3.5}$$

easily obtaining:

$$\left[\dot{h}\right]\propto\sigma\propto P_{O_2}^{1/6} \tag{3.6}$$

substituting Eq. (3.3) into Eq. (3.2) for doped lanthanum nickelates results in:

$$P_{O_2}^{1/2}=K_{2p}\left(\left(\left[B_{Ni}^{\bullet}\right]-\left[A_{La}'\right]\right)\left[\dot{h}\right]^2+\left[\dot{h}\right]^3\right) \tag{3.7}$$

Eqs. (3.1)-(3.7) show that adding lower valence elements in the A site may increase the overall conductivity and decrease oxygen interstitials and B site (higher valence) dopants may have the opposite effect. This defect equilibrium is supported by previous work; doping by incorporating higher-valence cations, such as Co, Fe or Al often have a positive outcome, resulting in a higher concentration of interstitials anions, which may have a favorable effect on the ionic transport with a deleterious effect on the overall conductivity [11, 17, 20, 21, 23-26], while incorporation of Sr into LNO decreases oxygen diffusivity [11-13, 23]. However, doping with Sr increase the overall conductivity, and EIS studies in Sr doped $La_2NiO_{4+\delta}$, points a lower area specific resistance values in comparison with the undoped compound, which is advantageous for IT-SOFC applications [27, 28].

Substituting divalent Sr for trivalent La on A-site and hexavalent Mo for divalent Ni on B-site in $La_{2-y}A_yNi_{1-x}B_xO_{4+\delta}$, the electroneutrality may be formulated viz.:

$$2\left[O_i''\right]+\left[Sr_{La}'\right]=\left[\dot{h}\right]+4\left[Mo_{Ni}^{\bullet\bullet\bullet\bullet}\right] \tag{3.8}$$

Eqs. (3.1)-(3.8) will form the basis for discussing the behavior of conductivity for both non-substituted and substituted LN.

3.1.2. Oxygen Transport Properties

Bulk diffusion, can be defined as the rate that ions move through the solid matrix (crystal lattice), and oxygen surface exchange is the process when oxygen gas is adsorbed into the crystal lattice of the material. Exist three fundamental experimental techniques usually applied to obtain the bulk diffusion and surface exchange (also called transport coefficients) [29, 30]:

Electrical experiment: an outer electrical potential is applied as a driving force. In the case of an ionic conductor the internal ionic current is balanced by other electronic current, which is measured. *Tracer experiment*: A tracer composition gradient is applied and the diffusion coefficient of the tracer can be found by an analysis of the tracer diffusion profile in chemically homogeneous solids. *Chemical gradient*: A chemical composition gradient is applied and an internal response is induced in the sample [31, 32].

From the experiments is possible to obtain the diffusion and surface exchange coefficients. The experimental rate constants calculated from the experiments electrical (Q), tracer (*) and chemical (chem) are denoted as D_Q, D^*, D_{chem} for diffusion coefficients and k_Q, k^*, k_{chem} for surface exchange. The coefficients for each sort of experiment are different and correspond to specific conditions. However, the coefficients are related showing to be a measurement of the same phenomena [33-35]:

$$k_{chem} = w_0 k^* \tag{3.9}$$

$$D_{chem} = w_0 D^* \tag{3.10}$$

where w_0 is a thermodynamic factor that can be found experimentally and the coefficients of the electrical and tracer experiment are approximately equal if the experimental conditions are similar.

In this work the chemical experiment was used by electrical conductivity relaxation, where the response in conductivity is measured in different temperature conditions, while applying a chemical gradient of P_{O2}.

3.1.3. Chapter's Scope

The aim of this chapter was to analyze the phase relations of LNO doped with Sr and Mo, and measure their effect on oxygen exchange kinetics. The oxygen transport properties, bulk diffusion and surface

exchange, were assessed by electrical conductivity relaxation of $La_{1.8}Sr_{0.2}Ni_{0.95}Mo_{0.05}O_{4+\delta}$. Measurements were performed as function of temperature and oxygen partial pressure, and discussed with previous results in related compounds.

3.2. METHOD

3.2.1. Material Synthesis

The list of chemicals used for powder synthesis is given in Table 3.1. K_2NiF_4-type oxides in the system $La_{2-y}Sr_yNi_{1-x}Mo_xO_{4+\delta}$ were synthesized by two methods, namely solid-state reaction (SS) and spray pyrolysis (SP). Carbonates and oxides were used as starting materials for the SS method. La_2O_3 and NiO were calcined at 1000 ºC for 12 h in a furnace (Nabertherm P330). The suspension of stoichiometric ratios of starting materials in ethanol were mixed in a planetary mill (Retsch PM 100) with zirconia balls of 0.5 cm of diameter for 45 min, afterwards were dried in a rotavapour (Buchi Rotavapour), uniaxial pressed and then the high temperature solid state reaction in air, where the maximum temperature of the thermal cycle was changed between 1100-1500 ◦C. The heat treatment was performed for 12 h at maximum temperature in a high temperature furnace (Entech HT2, Chamber Furnace), the process was repeated up to 3 times to the same powder. A flow chart of the solid-state synthesis procedure can be seen in Fig 3.2.

Table 3.1. List of chemicals used for powder synthesis. No shading: solid state reaction (SS). Light gray shading: spray pyrolysis (SP).

Chemical	Formula	Purity	Supplier
Strontium Carbonate	$SrCO_3$	99.4 wt%	Alfa Aesar GmbH
Lanthanum Oxide	La_2O_3	99.0 wt%	Sigma Aldrich
Nickel Oxide	NiO	99.9 wt%	Sigma Aldrich
Molybdenum Oxide	MoO_3	99.5 wt%	Sigma Aldrich
Ethanol	CH_3CH_2OH	≥99.8 vol%	VWR AS
Strontium nitrate	$Sr(NO_3)_2$	99.0 wt%	Sigma Aldrich
Nickel nitrate hexahydrate	$Ni(NO_3)_2{\cdot}6H_2O$	99.9 wt%	Sigma Aldrich
Ammonium molybdate tetrahydrate	$(NH_4)_6Mo_7O_{24}$	99.8 wt%	Sigma Aldrich
Lanthanum nitrate hexahydrate	$La(NO_3)_2{\cdot}6H_2O$	99.0 wt%	Sigma Aldrich
Ethylenediaminetetraacetic acid	$H_4{\cdot}EDTA$	99 wt%	Acros Organics
Malic acid	$C_4H_6O_5$	99 wt%	Merck
Nitric acid	HNO_3	65 wt%	Merck
Ammonia solution	NH_3	25 wt%	Merck

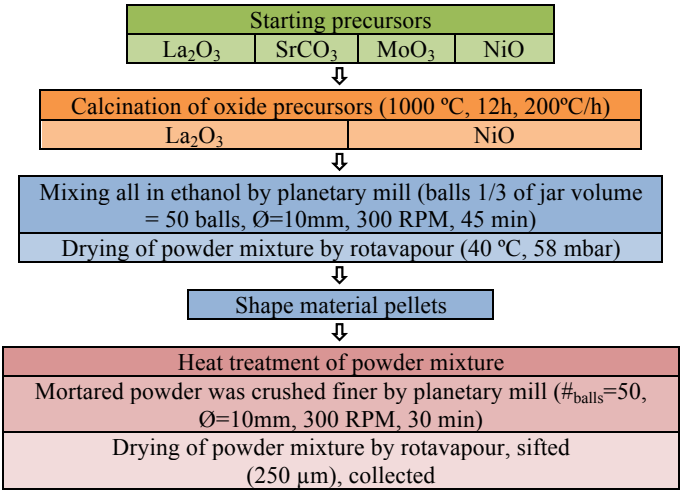

Fig 3.2. Flow chart of the solid-state reaction (SS) process used.

The SP powders were synthesized from stoichiometric aqueous solutions of La–EDTA (EDTA, ethylenediaminetetraacetic), Ni–EDTA, Mo–malic acid solution, and Sr-Nitrate. The solutions were prepared as seen in the flow charts Figs 3.3, 3.4 and 3.5, typical final concentration of solutions prior to spraying was 0.2 M.

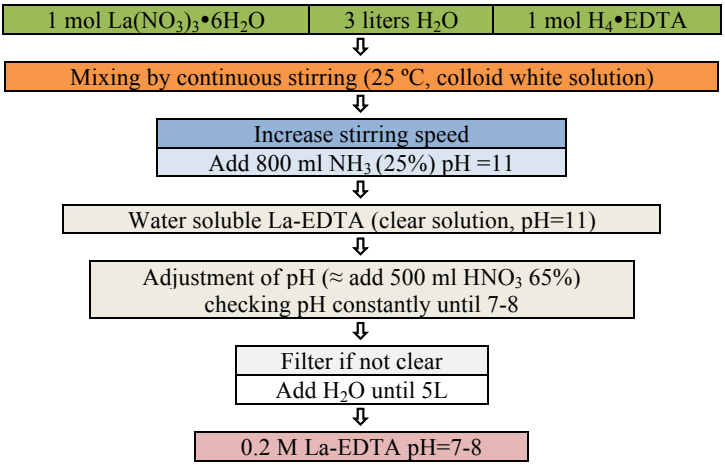

Fig 3.3. Flow chart preparation route of La-EDTA complex.

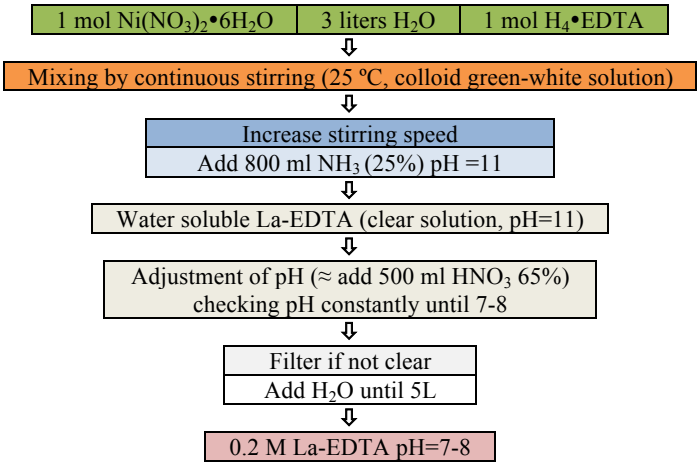

Fig 3.4. Flow chart preparation route of Ni-EDTA complex.

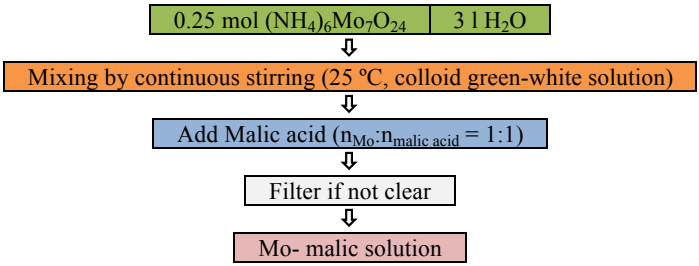

Fig 3.5. Flow chart preparation route of Mo-malic solution.

The concentration of each solution was determined in clear filtered solutions by thermogravimetric standardization, which consists in heat up samples of each solution and determines the concentration as follows.

Four porcelain crucibles for each solution were used for the standardization. The crucibles with glass wool on them were heated to 1000ºC for 6h. 2-3 ml of each solution were used for the standardization and were added into the crucibles with glass wool previously heated. The heating procedure for each solution is shown in Fig 3.6.

The solutions of La–EDTA, Ni–EDTA, Mo–malic, and Sr-Nitrate previously prepared, were mixed in stoichiometric amounts to produce compositions of the system $La_{2-y}Sr_yNi_{1-x}Mo_xO_{4+\delta}$: y=0;x=0.05, y=0.2;x=0.05, y=0.4;x=0.05. The resultant solution was stirred during

24 h. The homogeneous solution were pyrolysed using the pilot scale equipment showed in Fig 3.7 (spray pyrolysis pilot plant, CerPoTech-NTNU). The main airflow through the furnace was set to 1 m^3/min. The precursor was pumped with a flow rate of 8 l/h into the water-cooled lance and sprayed by a two-phase nozzle (Ø=1mm) with 1.5 bar pressurized air to give atomized spray. The spray was pyrolysed in a rotating furnace at 850°C. The outlet temperature of the furnace was around 450°C.

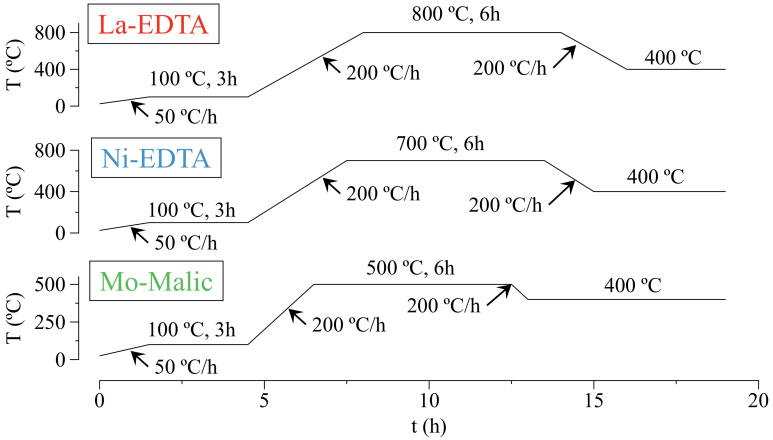

Fig 3.6. Thermal cycles: La-EDTA, Ni-EDTA, Mo-Malic for standardization procedure.

Details of spray pyrolysis procedure are given elsewhere [34]. As-prepared powders were dry ball milled for 15 min, calcined at 700 ºC for 8h, ball milled in 100% ethanol for 12 h, dried in a rotavapour and sieved at 50 µm mesh.

Phase determination of powders and samples was done by X-ray powder diffraction (XRD, AXS D8Focu, Bruker). The XRD-patterns shown in this work was recorded in θ-range $20^o \leq \theta \leq 50^o$ using CuKα-radiation.

The micrographs seen in this work were taken in a scanning electron microscope (LVSEM, S-3400N Hitachi). Samples were placed on sample holders by either tacky carbon tape or carbon glue. No conducting coating of the samples was necessary because the samples are electronically conductive.

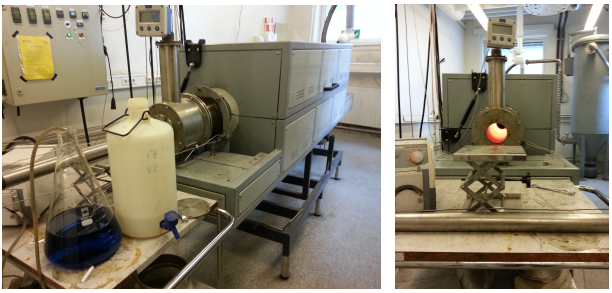

Fig 3.7 Spray pyrolysis pilot plant.

3.2.2. Transport Properties

The conductivity and oxygen transport properties were measured for $La_{1.8}Sr_{0.2}Ni_{0.95}Mo_{0.05}O_{4+\delta}$ and assessed by electrical conductivity relaxation (ECR), with a four-point DC method at 600 to 900 ºC using bar samples with the experimental setup outline in Fig 3.8.

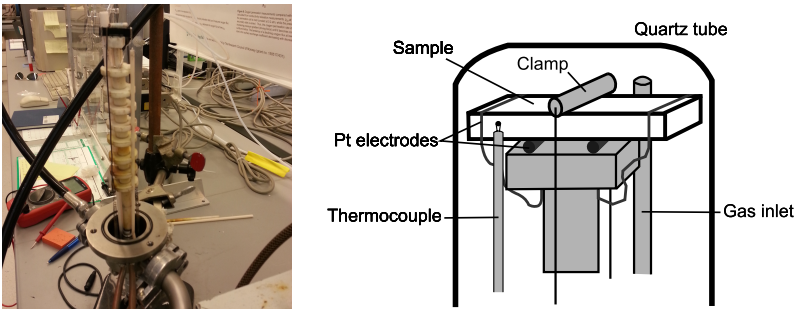

Fig 3.8. Experimental setup outline for electrical conductivity relaxation (ECR), four-point DC method.

An O_2/N_2 gas-mixing equipment (Test bench, NTNU), was used to control the oxygen partial pressure (Fig 3.9). The gas switches were controlled between P_{O2}= 0.2/0.117, 0.117/0.066, 0.066/0.037, 0.037/0.02, 0.02/0.0117, 0.0117/0.0066 atm, half P_{O2} step than reported by other works (i.e. [24]) in order to increase the parameters accuracy as recommended in [35].

The bar-shaped green bodies were prepared by uniaxial pressing (0.8kN) followed by cold isostatic pressing (CIP, 200MPa). The

prepared bodies were heated in air with a rate of 200 ºC/h until 1500 ºC, for 4 h at maximum temperature and cooled with a rate of 200 ºC/h to. Afterwards, the samples with >95% of relative density as measured by the Archimedes´method, were cut and fine grade polished using 1 µm diamond paste, to final dimensions of 1×5×20 mm.

.

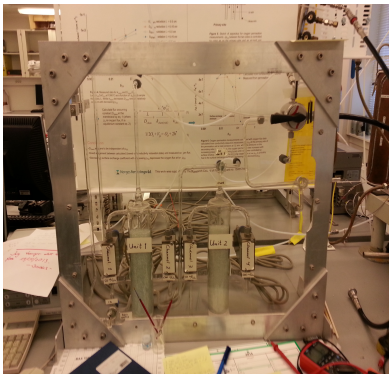

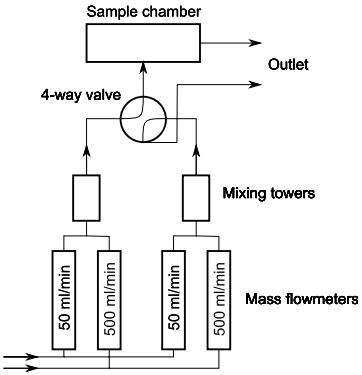

Fig 3.9. O_2/N_2 gas-mixing control equipment.

In ECR experiments, the sample is held in equilibrium at a given oxygen partial pressure condition and constant temperature. Then the gas atmosphere is abruptly changed into a different oxygen pressure at the same temperature. The conductivity behavior depends on the oxygen content and is recorded until a new equilibrium condition is achieved. The transient conductivity relaxation behavior can be precisely described by Fick's second law as [33]:

$$\frac{\sigma_t - \sigma_t}{\sigma_\infty - \sigma_0} = 1 - \sum_{n=1}^{\infty} \frac{2A^2 \exp(-\beta_n^2 D_{chem} t / l^2)}{\beta_n^2 (\beta_n^2 + A^2 + A)} \tag{3.11}$$

where σ is the conductivity and the subscripts 0, t and ∞, are time=0, any given time t, and infinite time respectively. D_{chem} is the chemical diffusion coefficient of oxygen. A is a measure of the contribution from the surface exchange and defined as the ratio of half the sample thickness l to the characteristic length l_d as:

$$A = \frac{l}{l_d} = \frac{l \times k_{chem}}{D_{chem}} \tag{3.12}$$

where k_{chem} is the surface exchange coefficient and β_n is the positive root of:

$$\beta_n \tan \beta_n = A \tag{3.13}$$

Eq. (3.11) can be solved numerically [35, 36] as follows. A change in the oxygen partial pressure will in practical cases not be a discrete step but rather a continuous change over time depending primarily on the flow rate and reactor cross section. The change in oxygen partial pressure may be described by an exponential function, viz.:

$$\frac{P_{O_2 t}(t) - P_{O_2 t=\infty}}{P_{O_2 t=0}(t) - P_{O_2 t=\infty}} = \exp\left(-\frac{t}{\tau_f}\right) \tag{3.14}$$

where τ_f is the reactor flush time. The solution of the Fick's second law of diffusion:

$$\frac{\partial C_0(x,t)}{\partial t} = D_{chem} \frac{\partial^2 C_0(x,t)}{\partial x^2} \tag{3.15}$$

For a long cylindrical sample (1-dimensional) using the change in oxygen partial pressure as described in Eq. (3.14) have been described by den Otter et al. [36] and are given below in terms of sample mass, M:

$$\frac{M_t - M_0}{M_\infty - M_0} = 1 - \exp\left(-\frac{t}{\tau_f}\right) - \sum_{n=1}^{\infty} A_n \frac{\tau_n}{\tau_n - \tau_f}\left[\exp\left(-\frac{t}{\tau_n}\right) - \exp\left(-\frac{t}{\tau_f}\right)\right] \tag{3.16}$$

where M_t is the sample mass, respectively, at any given time (t = t) and subscripts 0 and ∞ denotes the mass at time t = 0 and t = ∞, respectively. The parameter A_n is given by:

$$A_n = \frac{2L_\rho^2}{\rho_n^2(\rho_n^2 + L_\rho^2 + L_\rho)} \tag{3.17}$$

and

$$\tau_n = \frac{r^2}{\rho_n^2 D_{chem}} \tag{3.18}$$

where r is the sample radius. The parameter L_ρ and the eigenvalue ρ_n are solved from:

$$\rho_n J_1(\rho_n) = L_\rho J_0(\rho_n) = \frac{k_{chem}}{D_{chem}} r J_0(\rho_n) \tag{3.19}$$

where J_0 and J_1 denotes the first and second Bessel functions of the first kind. As a criterion for applying conductivity relaxation to assess the transport coefficients of a material, the conductivity, σ, must be linearly proportional to the oxygen non-stoichiometry. When this criterion is fulfilled, the relation between the conductivity and total mass change of the sample, due to a change in oxygen non-stoichiometry, is given by:

$$\frac{\sigma_t - \sigma_0}{\sigma_\infty - \sigma_0} = \frac{M_t - M_0}{M_\infty - M_0} \tag{3.20}$$

where Eq. (3.20) is equal to (3.11) and (3.16), this can be substituted on the left side of Eq. (3.16) and the conductivity response change in partial pressure in oxygen can thus be used to calculate D_{chem} and k_{chem}.

The transport coefficients were determined by fitting the electrical conductivity relaxation data to the Eq. (3.20) left member, and solving Eqs. (3.11) to (3.20). The conductivity relaxation time varies with temperature and P_{O2}, as showed by data given in Fig 3.10; time increases by decreasing temperature and/or $P_{O2.}$

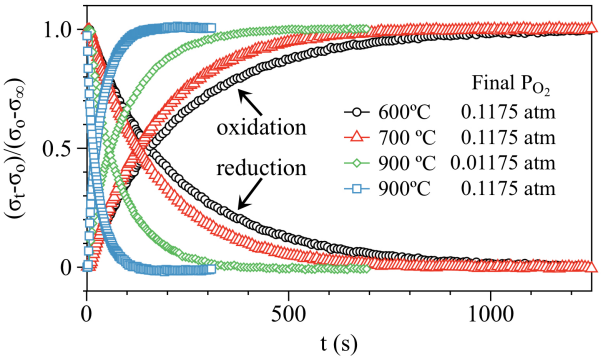

Fig. 3.10. Typical conductivity relaxation profiles of $La_{1.8}Sr_{0.2}Ni_{0.95}Mo_{0.05}O_{4+\delta}$ at different temperatures P_{O2}= 0.2/0.117, 0.117/0.066 and 0.02/0.0117, 0.0117/0.0066 atm.

Thus, with the described procedure it is possible to calculate the D_{chem} and k_{chem} values for each conductivity relaxation. For the calculations, the fitting error and convergence were assessed to obtain accurate values as seen in Fig 3.11. When the functions achieve a minimum in the convergence curve for both parameters (Fig 3.11a), the fit was accurately achieved. When the convergence is not achieved, the curve present a shape parabolic alike and the coefficients must be

neglected, for instance Fig 3.11b.

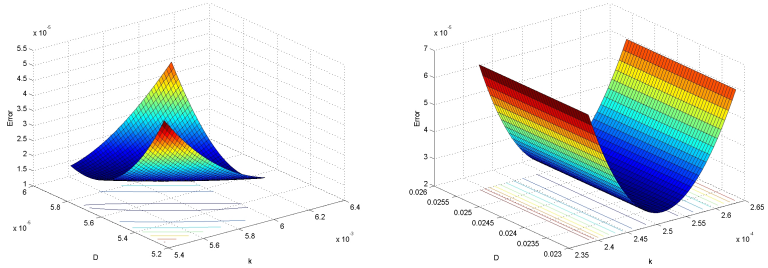

(a) (b)

Fig 3.11. D_{chem} and k_{chem} 3D-error convergence. a) The minimum convergence value was achieved by both parameters D_{chem} and k_{chem}. b) Minimum achieved by solely k_{chem} showing, coefficients inaccurate fit.

3.3. RESULTS AND DISCUSSION

3.3.1. Phase Relations

XRD-analysis of LN substituted with Mo is given in Fig. 3.12 showing formation of secondary phases at Mo $\geq$ 0.0125. Assuming that equilibrium is established a perovskite type phase, $LaMo_{0.2}Ni_{0.8}O_3$, coexists with the main phase for Mo=0.0125 and 0.025, while three phases coexist at Mo=0.05 ($LaMo_{0.2}Ni_{0.8}O_3$, La_6MoO_{12} and main phase).

XRD analysis of $La_{1.8}Sr_{0.2}Ni_{0.95}Mo_{0.05}O_{4+\delta}$ sintered at temperatures between 1250 and 1500^{o}C is given in Fig. 3.13. The formation of a single phase is observed at all temperatures investigated, indicating solid solubility at Mo $\leq$ 0.05 and Sr=0.2. XRD-analysis at even higher Mo-contents and Sr=0.2 is given in Fig. 3.14 revealing the presence of a secondary phase (perovskite type) at Mo>0.05. Phase relations for compositions with Sr=0.4 and Mo=0.05 is given in Fig. 3.15 and shows the formation of a secondary $SrMoO_4$-phase at all temperatures. A summary of phase relations for all compositions are given in Table 3.2.

Samples produced by SS or SP methods show similar results. The difference noticed among methods and sintering temperatures lies on the peaks intensity. Table 3.1 summarizes the results from the synthesis methods and the cell parameters.

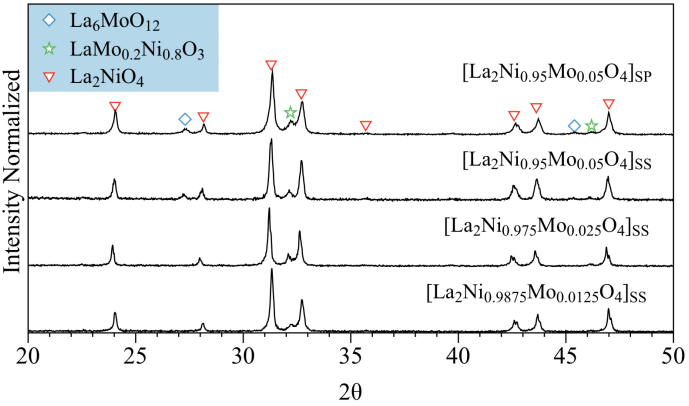

Fig. 3.12 XRD-data for $La_2Ni_{1-x}Mo_xO_{4+\delta}$–samples with x=0.0125, 0.025, 0.05. All SS-samples are sintered at 1300°C while SP-sample is sintered at 1400°C. The presence of the major phase is compared with the characteristic peaks from La_2NiO_4.

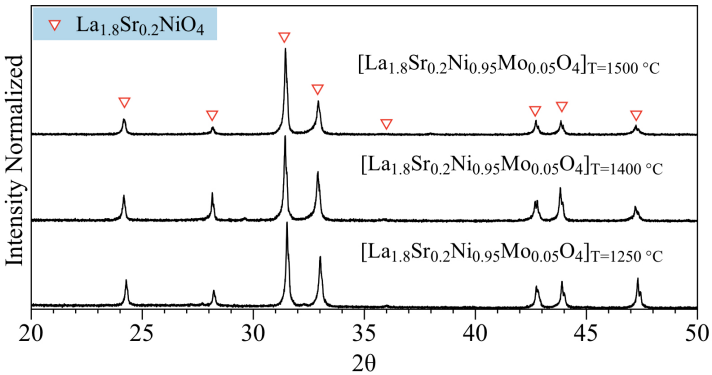

Fig. 3.13. XRD-data for $La_{1.8}Sr_{0.2}Ni_{0.95}Mo_{0.05}O_{4+\delta}$-samples sintered at 1250 (SS-sample), 1400 (SS-sample) and 1500 ºC (SP-sample). The presence of the major phase is compared with the characteristic peaks from $La_{1.8}Sr_{0.2}iO_4$.

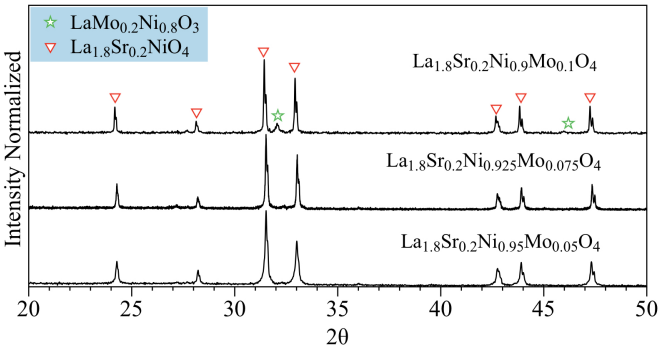

Fig. 3.14. XRD-data for $La_{1.8}Sr_{0.2}Ni_{1-x}Mo_xO_{4+\delta}$-SS-samples with x=0.05, 0.075 and 0.1. All samples sintered at 1300°C. The presence of the major phase is compared with the characteristic peaks from $La_{1.8}Sr_{0.2}iO_4$.

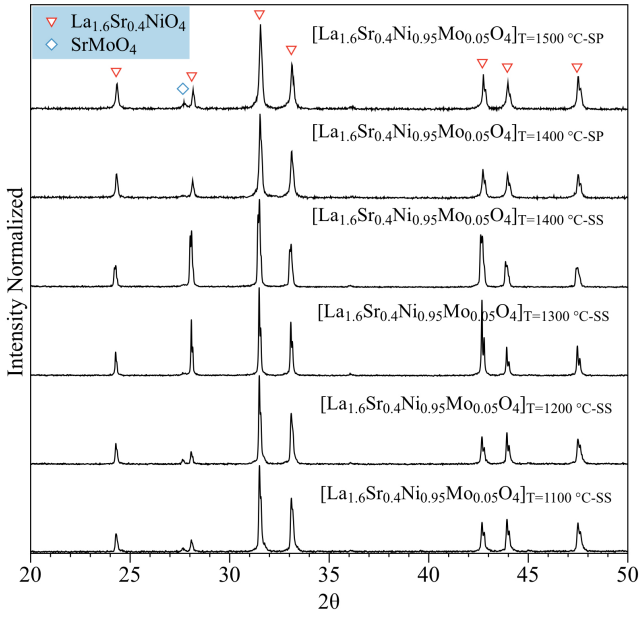

Fig. 3.15. XRD-data for $La_{1.6}Sr_{0.4}Ni_{0.95}Mo_{0.05}O_{4+\delta}$–samples. Type of powder and sintering temperature is given in the figure.

Table 3.2. Synthesis methods, sintering temperature and phases observed according to XRD-analysis. Resulting cell parameters for the major phase are also listed.

y	x	Via	T/ºC	Major Phase	Minor Phases	a/Å	c/Å
0.0	0.05	SP	1400	$La_2Ni_{1-z}Mo_zO_{4+\delta}$ $z<0.0125$	La_6MoO_{12} - $La_2Mo_{0.2}Ni_{0.8}O_3$	3.866	12.665
	0.0125	SS	1300	$La_2Ni_{1-z}Mo_zO_{4+\delta}$ $z<0.0125$	La_6MoO_{12}	3.864	12.679
	0.025	SS	1300	$La_2Ni_{1-z}Mo_zO_{4+\delta}$ $z<0.0125$	La_6MoO_{12}	3.863	12.682
	0.05	SS	1300	$La_2Ni_{1-z}Mo_zO_{4+\delta}$ $z<0.0125$	La_6MoO_{12}- $La_2Mo_{0.2}Ni_{0.8}O_3$	3.863	12.676
0.2	0.05	SP	1250	$La_{1.8}Sr_{0.2}Ni_{0.95}Mo_{0.05}O_{4+\delta}$	-	3.848	12.695
	0.05	SP	1400	$La_{1.8}Sr_{0.2}Ni_{0.95}Mo_{0.05}O_{4+\delta}$	-	3.848	12.676
	0.05	SP	1500	$La_{1.8}Sr_{0.2}Ni_{0.95}Mo_{0.05}O_{4+\delta}$	-	3.849	12.675
	0.05	SS	1300	$La_{1.8}Sr_{0.2}Ni_{0.95}Mo_{0.05}O_{4+\delta}$	-	3.847	12.696
	0.075	SS	1300	$La_{1.8}Sr_{0.2}Ni_{1-z}Mo_zO_{4+\delta}$ $z\approx0.075$	-	3.847	12.688
	0.1	SS	1300	$La_{1.8}Sr_{0.2}Ni_{1-z}Mo_zO_{4+\delta}$ $z\approx0.075$	$La_2Mo_{0.2}Ni_{0.8}O_3$	3.847	12.689
0.4	0.05	SP	1400	$La_{1.6}Sr_{0.4}Ni_{1-z}Mo_zO_{4+\delta}$ $z<0.05$	$SrMo_4$	3.287	12.704
	0.05	SP	1500	$La_{1.6}Sr_{0.4}Ni_{1-z}Mo_zO_{4+\delta}$ $z<0.05$	$SrMo_4$	3.830	12.702
	0.05	SS	1100	$La_{1.6}Sr_{0.4}Ni_{1-z}Mo_zO_{4+\delta}$ $z<0.05$	$SrMo_4$	3.827	12.711
	0.05	SS	1200	$La_{1.6}Sr_{0.4}Ni_{1-z}Mo_zO_{4+\delta}$ $z<0.05$	$SrMo_4$	3.826	12.708
	0.05	SS	1300	$La_{1.6}Sr_{0.4}Ni_{1-z}Mo_zO_{4+\delta}$ $z<0.05$	$SrMo_4$	3.828	12.705
	0.05	SS	1400	$La_{1.6}Sr_{0.4}Ni_{1-z}Mo_zO_{4+\delta}$ $z<0.05$	$SrMo_4$	3.830	12.703

The K_2NiF_4-type structure of $La_{2-y}Sr_yNi_{1-x}Mo_xO_{4+\delta}$ was found to be tetragonal with space group I4/mmm. Fig. 3.16 shows the variation in the a- and c- axis with Mo-substitution for compositions with Sr-content corresponding to 0, 0.2 and 0.4.

There is an indication that for compositions with Sr=0 and 0.2 the c-axis shows a behavior corresponding to Vegard´s law indicating a Mo-solubility limit at 0.0125 and 0.05, respectively. This is supported by Fig. 3.13 (Sr=0), where the presence of secondary phases is evident at $Mo \geq 0.0125$, and Fig. 3.15 (Sr=0.2), where secondary phase are formed at $Mo \geq 0.05$. The c-axis (Fig. 3.16) is slightly increased by Mo-content for compositions with Sr=0.4, indicating a low solid solubility and formation of secondary phases even at low concentrations of Mo.

Supported by Fig. 3.15 showing the formation of $SrMoO_4$ at temperatures between 1100 and 1500°C and Mo=0.05. It is also seen in Fig. 3.16 that the a-axis is relatively independent of the Mo-content, while there is a pronounced reduction with higher Sr-content. The opposite trend is observed for the c-axis where an expansion takes place with increasing Sr-content for compositions without Mo.

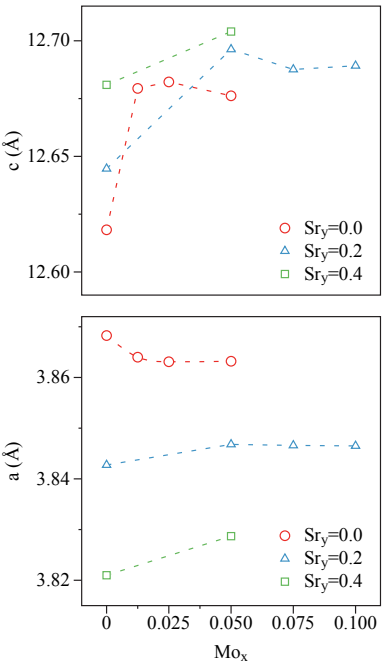

Fig. 3.16 Variation in cell parameter for $La_{2-y}Sr_yNi_{1-x}Mo_xO_{4+\delta}$ with Mo-content for compositions with 0.0, 0.2 and 0.4 Sr. Cell parameter for La_2NiO_4 is taken from [14]. Samples heat treated at T=1300°C.

Since Sr^{2+} ionic radius is larger than that of La^{3+} a lattice expansion is expected as Sr is introduced. In addition, as documented by Takeda et al [14] and Gopalakrishnan et al. [37], the average oxidation state of Ni increase with Sr content resulting in an c-axis expansion and a-axis contraction. According to Bassat et al. [38], the c-axis expansion may diminish the activation energy for oxygen mobility. However, as

reported by Aguadero et al. [19], the a-axis contraction results in a decrease in the cell volume, which ends up on minor tendency to accommodate excess of oxygen as Sr content increases. These two opposite trends may explain the behavior of the a- and c-axis and oxygen transport in the absence of Mo.

A comparison among lattice parameters is given in Fig. 3.17. The c-axis expands as B-site is substituted with 10% Co and Fe, while the a-axis is virtually independent. However, for compositions with Sr=0.2, the c-axis expands significantly and a-axis moderately as 0.05 Mo is added. Assuming 6-valent Mo on B-site, the expanded lattice may be due to an overall increase in interstitial oxygen. The ionic radius of 6-valent Mo is significantly smaller than divalent Ni and should not result in expansion based on size only.

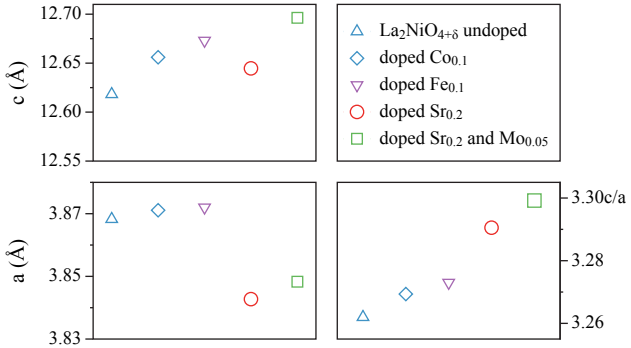

Fig. 3.17. Lattice parameters comparison among LN [14] and LN substituted with Co=0.1 [20], Fe=0.1 [11] and Sr=0.2 [14]. Sample substituted with both Sr and Mo (LSNM) is taken from this work.

3.3.2. Transport Properties

As previously described, the electrical conductivity and transport properties as a function of temperature and partial pressure oxygen were assessed by ECR measurements, with a bar-shaped body of single phase $La_{1.8}Sr_{0.2}Ni_{0.95}Mo_{0.05}O_{4+\delta}$. The sintered body with final dimensions of 1×5×20 mm presents a relative density of 95.34% measured by the

Archimedes' method, and an average grain size of 14.3±8 μm calculated from SEM micrographs by image analysis.

The oxygen pressure and temperature dependencies of $La_{1.8}Sr_{0.2}Ni_{0.95}Mo_{0.05}O_{4+\delta}$ compared with other compositions are shown in Figs. 3.19-3.20. The conductivity for all samples is seen to increase linearly with P_{O2} consistent with p-type conductivity, Eq. (3.6). Adding Sr to LN gives a significant increase in conductivity while the presence of dopants on the B-site as Mo, reduce the conductivity even below LN. According to the relationship given in Eq. (3.6), a 1/6-slope is predicted for LN, this behavior is reported by Jeon et al. [34] at low pO_2´s, however, at higher partial pressures they report a less pronounced dependency approaching 1/10. The reason for the deviation at higher pO_2´s may be due to formation of clusters and associates of point defects forming neutral point defects [35].

A defect model taking these phenomena into account is beyond the scope of the present work. It is evident from Figs. 3.19-3.20 that Mo reduce the electronic conductivity to some degree, the reasons for this may be twofold: The p-type conductivity is governed by a polaron hopping mechanism corresponding to electrons jumping between Ni-sites. 6- valent Mo- will occupy a Ni- site as $Mo_{Ni}^{\bullet\bullet\bullet\bullet}$ (Cf. Eq. (3.8)), and probably blocking the pathway for electronic charge carriers. Secondly, Mo may also reduce the average oxidation number of Ni corresponding to a lower fraction of Ni^{3+}/Ni^{2+}, that is, reduce the concentration of holes ($h^{\bullet}$). The overall effect will be a reduced electronic conductivity.

For the dopants in the composition $La_{1.8}Sr_{0.2}Ni_{0.95}Mo_{0.05}O_{4+\delta}$, the following point defects can be considered as the most probable: 1) Sr ions on La sites with one effective negative charge for the substitution of La^{+3} with Sr^{+2}; 2) interstitial oxygen ions with double negative effective charge; 3) Ni ions on regular positions with one effective positive charge for the increment of valence of Ni^{+2} to Ni^{+3}; 4) Mo ions on Ni sites with four effective positive charge for the substitution of Ni^{+2} with Mo^{+6}. Thus, the behavior is in agreement with the equilibrium in Eq. (3.8) and the conductivity trends.

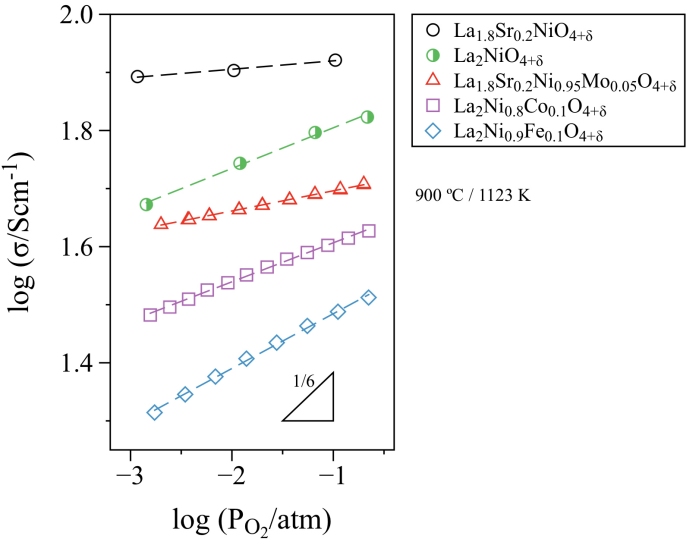

Fig. 3.19. Conductivity vs P_{O2} comparison at 900 ºC among LNO [39], and LNO doped with: Sr=0.1 Fe=0.1[11], Fe=0.1[21], Sr=0.2 [28], Co=0.1 [20].

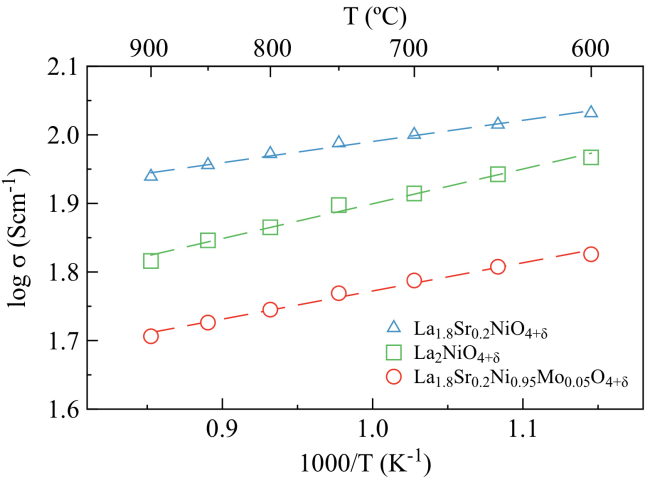

Fig. 3.20. $La_{1.8}Sr_{0.2}Ni_{0.95}Mo_{0.05}O_{4+\delta}$ conductivity vs. temperature in air compared with lanthanum nickelate compositions [28].

The conductivity-temperature behavior in Fig. 3.20 suggests that the concentration of electron holes decrease with increasing temperature, which leads to decreasing conductivity at high temperatures as shown by the present measurements and the defects model; oxygen interstitials and electron holes are the major defects in the material, charge compensating each other.

The oxygen transport properties resulting from ECR-analysis are given in Figs. 3.21-3.25. It is seen in Fig. 3.21 that k_{chem} is only marginally higher for a reduction step than an oxidation step, while D_{chem} is virtually independent of the type of step.

Both D_{chem} and k_{chem} increase with pO_2 and temperature. In Fig. 3.22 and 3.23 the temperature dependency of D_{chem} for LSNM is compared with LN and LSN reported in the literature. The D_{chem}–values are based on both oxidation and reduction steps, however, since the resulting D_{chem} should be independent of the type of step the data given in Fig. 3.22 and 3.23 is assumed to give a representative variation in D_{chem}, both with composition and temperature.

The activation energies for LSN and LSNM are rather similar, and adding Mo on B-site significantly increase the bulk-diffusion coefficient, this also seen by doping Al on B-site, probably due to increased population of mobile interstitial oxygen corresponding to substitution of divalent Ni with 6-valent Mo (Cf. Eq. (3.8)), also in agreement with the phase relations results. The activation energy for LN is about twice the activation energy observed for LSN and LSNM, while, at temperatures < 700^{o}C D_{chem} in LSNM is higher than D_{chem} for LN. Hence, substitution with Mo may give an advantage with respect to bulk diffusion at moderate temperatures.

This effect is also seen on oxygen diffusion coefficients extracted by tracers D^* in lanthanum nickelates based materials [13]. Conversely, Mo doping compensates the oxygen interstitials increases the D_{chem} values one order of magnitude, shifting the curve to LN range and showing higher diffusion coefficients at lower temperatures than 700ºC.

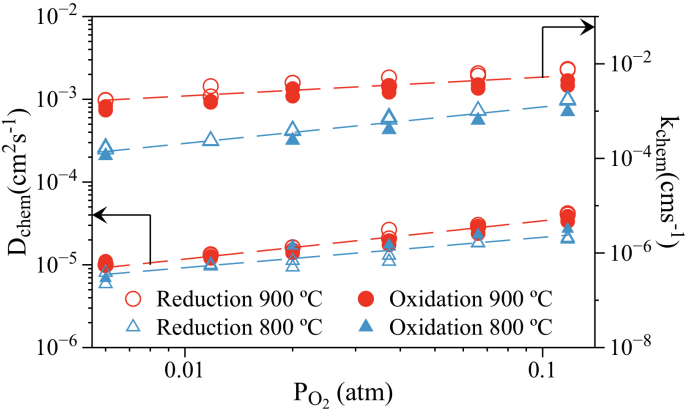

Fig. 3.21. Plot of D_{chem} and k_{chem} vs. Po_2 for 800 and 900 ºC. P_{O2}= 0.2/0.117, 0.117/0.066, 0.066/0.037, 0.037/0.02, 0.02/0.0117, 0.0117/0.0066 atm.

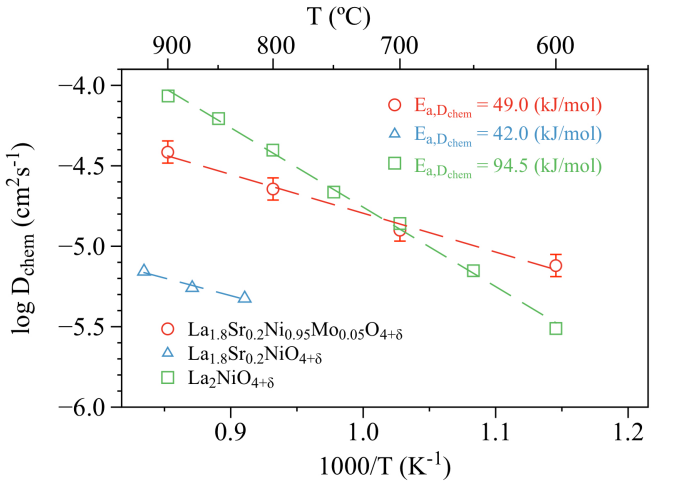

Fig. 3.22. Plot of D_{chem} vs. temperature and activation energies for $La_{1.8}Sr_{0.2}Ni_{0.95}Mo_{0.05}O_{4+\delta}$ (Po_2-step=0.2 to 0.117 atm), in comparison with $La_{1.8}Sr_{0.2}NiO_{4+\delta}$ [40] (Po_2-step=0.066 to 0.2 atm) and $La_2NiO_{4+\delta}$ [41] (Po_2-step=1.0 to 0.2 atm).

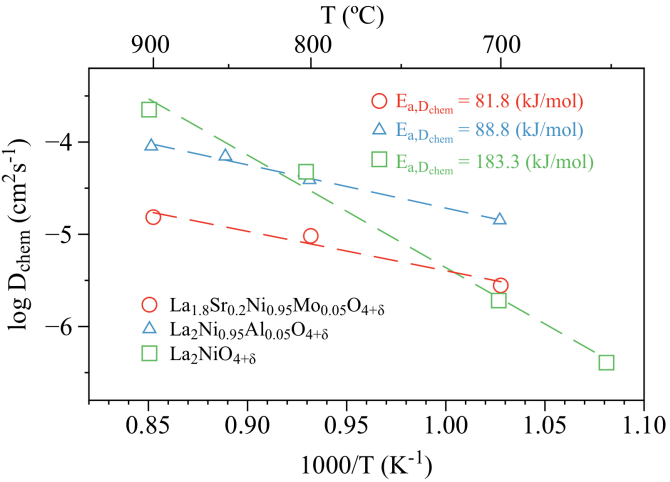

Fig. 3.23. Plot of D_{chem} vs. temperature and activation energies for $La_{1.8}Sr_{0.2}Ni_{0.95}Mo_{0.05}O_{4+\delta}$ (Po_2-step=0.037 to 0.02 atm), in comparison to $La_{1.8}Sr_{0.2}Ni_{0.95}Al_{0.05}O_{4+\delta}$ [24] (Po_2-step=0.066 to 0.02) and $La_2NiO_{4+\delta}$ [39] (Po_2-step=0.066 to 0.02 atm).

The D_{chem} data follow Arrhenius-type behaviors with activation energies of 49.0 and 81.8 kJ/mol for final P_{O2} 0.117 and 0.02 respectively. The process activation energies are lower for the doped series, as earlier discussed, the tetragonal K_2NiF_4 type structure doped with Mo has an elongated c-direction, leading to the assumption that oxygen mobility will be favored in the a-plane, diminishing the activation energy and leading the increase of interstitial oxygen, which is the case of the doped compounds, that trend to increase the a/c-axis ratio (Fig. 3.14). There have been a number of studies of the diffusion mechanism and results in the $La_2NiO_{4+\delta}$ and related compounds that supports the assumption [25, 38, 42, 43].

The behavior of surface exchange coefficients (k_{chem}) as function of the temperature compared with LN and LNA are summarized in Fig. 3.24. It is seen that surface exchange is enhanced with more than one order of magnitude when LN is substituted with Mo (0.05**)**. Skinner et al. [12] reported a diminution of 1 order of magnitude on the LN surface exchange coefficients k^* with the addition of Sr (0.2). Hence, doping the B-site of LN with higher valent compounds, as 6-valent Mo may increase the oxygen surface exchange in comparison with LN and LSN.

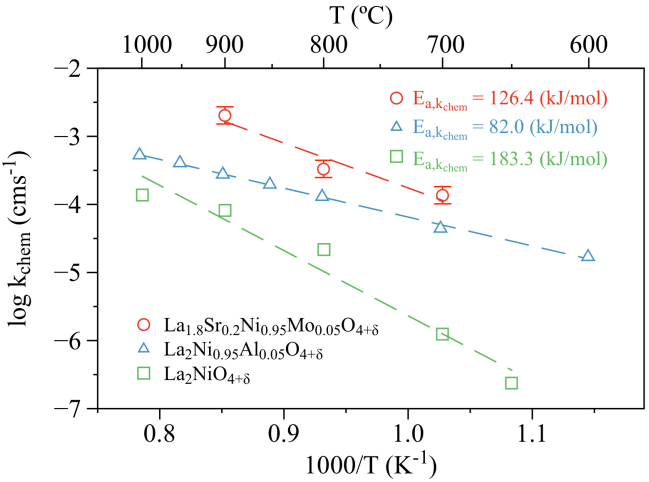

Fig. 3.24. Plot of k_{chem} vs. temperature and activation energies for $La_{1.8}Sr_{0.2}Ni_{0.95}Mo_{0.05}O_{4+\delta}$ (Po_2-step=0.037 to 0.02 atm), in comparison to $La_{1.8}Sr_{0.2}Ni_{0.95}Al_{0.05}O_{4+\delta}$ [24] (Po_2-step=0.066 to 0.02) and $La_2NiO_{4+\delta}$ [39] (Po_2-step=0.066 to 0.02).

Post-test analyses of samples subjected to ECR reveal the formation of a secondary phase rich in Sr and Mo on the surface, probably $SrMoO_4$ (Fig 3.25 and 3.26a-b). However, the bulk remains single phase LSNM, confirmed by SEM-backscatter micrographs (presence of darker zones represents another phase) and XRD-analysis (Fig 3.26c-d and 3.27). This suggests certain material instability in presence of oxygen at high temperatures (in this case 3 weeks of testing). Similar instability has been reported for $Sr_2Fe_{1.5}Mo_{0.5}O_{6-\delta}$ (SFM) which is unstable over time in air at temperatures above 400 °C, showing the formation of $SrMoO_4$ and $SrFeO_{3-x}$ [44, 45]. However, the transport coefficients resulting from ECR-analysis did not change during the 3 weeks of testing, indicating that the formation of a secondary phase at the surface did not affect the oxygen transport in the time interval investigated.

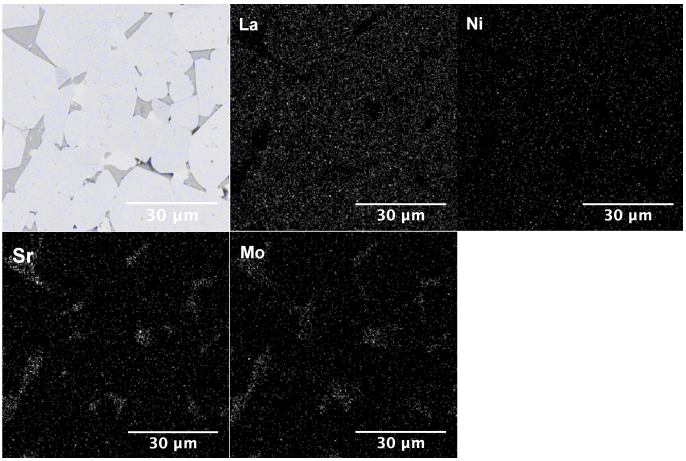

Fig. 3.25. EDS bar-shaped samples after ECR polished surface.

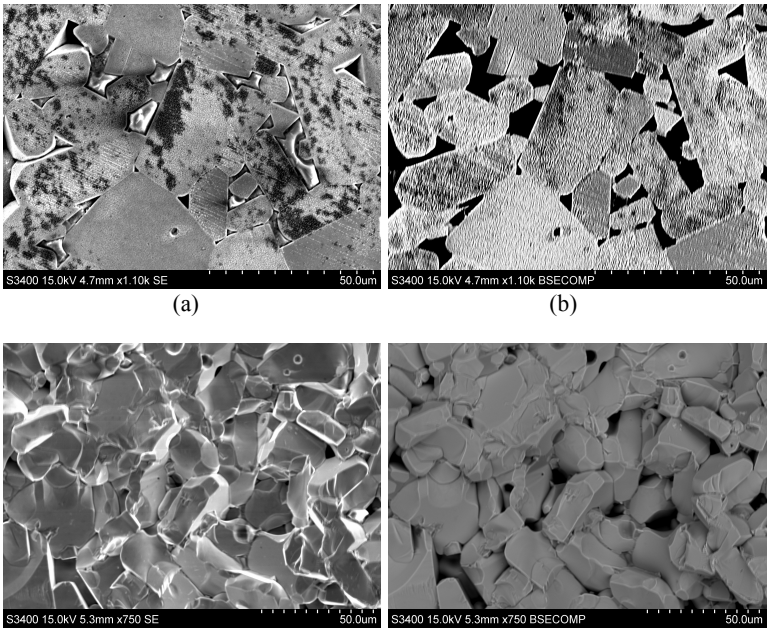

Fig. 3.26. SEM of bar-shaped samples after ECR: a) polished surface, b) backscatter of polished surface, c) fracture surface, d) backscatter fracture surface.

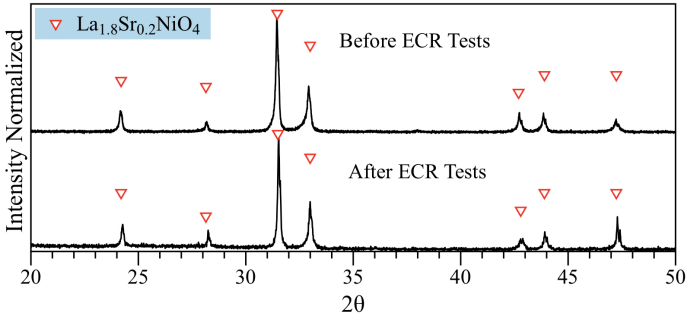

Fig. 3.27. XRD-data for $La_{1.8}Sr_{0.2}Ni_{0.95}Mo_{0.05}O_{4+\delta}$ –samples, before and after the electrical conductivity relaxation tests.

.

3.4. CONCLUSIONS

The system molybdenum-doped $La_{2-y}Sr_yNiO_{4+\delta}$ shows solubility, however, the limit is rapidly reached by small amounts of Mo, limited by Sr-substitution. Single-phase $La_{1.8}Sr_{0.2}Ni_{0.95}Mo_{0.05}O_{4+\delta}$ was successfully synthetized. The lattice parameters; result of the Sr-Mo doping, has an elongated c-direction, increasing oxygen mobility in the a-plane. The electrical conductivity and transport properties of single-phase of $La_{1.8}Sr_{0.2}Ni_{0.95}Mo_{0.05}O_{4+\delta}$ were assessed by electrical conductivity relaxation in the oxygen partial pressure range of 0.2 to 0.0066 atm at 600–900 ºC. The conductivity behaves p-type electronic on the studied range. Dependencies of electron-hole, oxygen interstitials, A-B-site doping and P_{O2} were explained by a simple defect model. Doping B-site with higher valence ions decrease the overall conductivity, but represents a favorable effect on ionic transport; the opposite effects by doping A-site with lower valence ions. Results disclose an enhancement on transport properties by partial substitution of nickel with molybdenum on the $La_{1.8}Sr_{0.2}NiO_{4+\delta}$. $La_2NiO_{4+\delta}$ surface exchange and bulk diffusion coefficients are surpassed at lower temperatures by $La_{1.8}Sr_{0.2}Ni_{0.95}Mo_{0.05}O_{4+\delta}$ transport data, with lower activation energy of both thermally activated processes D_{chem} and k_{chem}. $La_{1.8}Sr_{0.2}Ni_{0.95}Mo_{0.05}O_{4+\delta}$ presents instability in presence of oxygen and high temperature over time (>=600 ºC, 3 weeks), forming secondary phases, probably $SrMoO_4$ at the sample surface.

3.5. REFERENCES

[1] Mauvy F, Lalanne C, Bassat J-M, Grenier J-C, Zhao H, Huo L, et al. Electrode properties of Ln2NiO4 + δ (Ln = La , Nd , Pr) : AC Impedance and DC Polarization Studies. J Electrochem Soc. 2006;153:A1547-A53.
[2] Dailly J, Fourcade S, Largeteau A, Mauvy F, Grenier JC, Marrony M. Perovskite and A(2)MO(4)-type oxides as new cathode materials for protonic solid oxide fuel cells. Electrochim Acta. 2010;55:5847-53.
[3] Boehm E, Bassat JM, Dordor P, Mauvy F, Grenier JC, Stevens P. Oxygen diffusion and transport properties in non-stoichiometric Ln2−xNiO4+δ oxides. Solid State Ionics. 2005;176:2717-25.
[4] Sayers R, Liu J, Rustumji B, Skinner SJ. Novel K2NiF4-Type Materials for Solid Oxide Fuel Cells: Compatibility with Electrolytes in the Intermediate Temperature Range. Fuel Cells. 2008;8:338-43.
[5] Montenegro-Hernández A, Vega-Castillo J, Mogni L, Caneiro A. Thermal stability of Ln2NiO4+δ (Ln: La, Pr, Nd) and their chemical compatibility with YSZ and CGO solid electrolytes. Int J Hydrogen Energ. 2011;36:15704-14.
[6] Laguna-Bercero MA, Hanifi AR, Monzon H, Cunningham J, Etsell TH, Sarkar P. High performance of microtubular solid oxide fuel cells using Nd2NiO4+δ-based composite cathodes. Journal of Materials Chemistry A. 2014;2:9764-70.
[7] Zhao K, Wang Y-P, Chen M, Xu Q, Kim B-H, Huang D-P. Electrochemical evaluation of La2NiO4+δ as a cathode material for intermediate temperature solid oxide fuel cells. Int J Hydrogen Energ. 2014;39:7120-30.
[8] Zhang X, Zhang H, Liu X. High performance La2NiO4+δ-infiltrated (La0.6Sr0.4)0.995Co0.2Fe0.8O3−δ cathode for solid oxide fuel cells. J Power Sources. 2014;269:412-7.
[9] Kharton VV, Yaremchenko AA, Valente AA, Sobyanin VA, Belyaev VD, Semin GL, et al. Methane oxidation over Fe-, Co-, Ni- and V-containing mixed conductors. Solid State Ionics. 2005;176:781-91.
[10] Al Daroukh M, Vashook VV, Ullmann H, Tietz F, Arual Raj I. Oxides of the AMO3 and A2MO4-type: structural stability, electrical conductivity and thermal expansion. Solid State Ionics. 2003;158:141-50.
[11] V. Kharton V, P. Viskup A, N. Naumovich E, M. B. Marques F. Oxygen ion transport in La2NiO4-based ceramics. J Mater Chem. 1999;9:2623-9.
[12] Skinner SJ, Kilner JA. A comparison of the transport properties of La2−xSrxNi1−yFeyO4+δ where 0<x<0.2 and 0<y<0.2. Ionics. 1999;5:171-4.
[13] Skinner SJ, Kilner JA. Oxygen diffusion and surface exchange in La2−xSrxNiO4+δ. Solid State Ionics. 2000;135:709-12.

[14] Takeda Y, Kanno R, Sakano M, Yamamoto O, Takano M, Bando Y, et al. Crystal chemistry and physical properties of La2−xSrxNiO4 (0 ≤ x ≤ 1.6). Mater Res Bull. 1990;25:293-306.
[15] Singh KK, Ganguly P, Goodenough JB. Unusual effects of anisotropic bonding in Cu(II) and Ni(II) oxides with K2NiF4 structure. J Solid State Chem. 1984;52:254-73.
[16] James M, Attfield JP. Synthesis, crystal structure and magnetic properties of Ln2-SrNiO4 +/- δ solid solutions (Ln = La, Nd, Sm and Gd; 1.0 ≤x≤ 1.67). J Mater Chem. 1996;6:57-62.
[17] Tsipis EV, Naumovich EN, Patrakeev MV, Waerenborgh JC, Pivak YV, Gaczyński P, et al. Oxygen non-stoichiometry and defect thermodynamics in La2Ni0.9Fe0.1O4+δ. Journal of Physics and Chemistry of Solids. 2007;68:1443-55.
[18] Tarancon A, Burriel M, Santiso J, Skinner SJ, Kilner JA. Advances in layered oxide cathodes for intermediate temperature solid oxide fuel cells. J Mater Chem. 2010;20:3799-813.
[19] Aguadero A, Escudero MJ, Perez M, Alonso JA, Pomjakushin V, Daza L. Effect of Sr content on the crystal structure and electrical properties of the system La2-SrNiO4+ δ (0 ≤ x ≤ 1). Dalton Transactions. 2006:4377-83.
[20] Yaremchenko AA, Kharton VV, Patrakeev MV, Frade JR. p-Type electronic conductivity, oxygen permeability and stability of La2Ni0.9Co0.1O4+δ. J Mater Chem. 2003;13:1136-44.
[21] Kharton VV, Tsipis EV, Naumovich EN, Thursfield A, Patrakeev MV, Kolotygin VA, et al. Mixed conductivity, oxygen permeability and redox behavior of K2NiF4-type La2Ni0.9Fe0.1O4+δ. J Solid State Chem. 2008;181:1425-33.
[22] Li Z, Haugsrud R, Smith JB, Norby T. Transport properties and defect analysis of La1.9Sr0.1NiO4+δ. Solid State Ionics. 2009;180:1433-41.
[23] Kharton VV, Viskup AP, Kovalevsky AV, Naumovich EN, Marques FMB. Ionic transport in oxygen-hyperstoichiometric phases with K2NiF4-type structure. Solid State Ionics. 2001;143:337-53.
[24] Jeon S-Y, Singh B, Im H-N, Seong K-P, Song S-J. Charge and mass transport properties of La2Ni0.95Al0.05O4.025+δ. J Alloy Compd. 2014;589:572-8.
[25] Munnings CN, Skinner SJ, Amow G, Whitfield PS, Davidson IJ. Oxygen transport in the La2Ni1−xCoxO4+δ system. Solid State Ionics. 2005;176:1895-901.
[26] Kilner JA, Shaw CKM. Mass transport in La2Ni1−xCoxO4+δ oxides with the K2NiF4 structure. Solid State Ionics. 2002;154–155:523-7.
[27] Kammer K. An EIS study of La2 − x Sr x NiO4 + δ SOFC cathodes. Ionics. 2009;15:325-8.

[28] Nakamura T, Yashiro K, Sato K, Mizusaki J. Electronic state of oxygen nonstoichiometric La2-xSrxNiO4+[small delta] at high temperatures. Physical Chemistry Chemical Physics. 2009;11:3055-62.
[29] Bouwmeester HJM, Kruidhof H, Burggraaf AJ. Importance of the surface exchange kinetics as rate limiting step in oxygen permeation through mixed-conducting oxides. Solid State Ionics. 1994;72, Part 2:185-94.
[30] Maier J. Interaction of oxygen with oxides:: How to interpret measured effective rate constants? Solid State Ionics. 2000;135:575-88.
[31] Maier J. On the correlation of macroscopic and microscopic rate constants in solid state chemistry. Solid State Ionics. 1998;112:197-228.
[32] Eriksson A, Einarsrud M-A, Grande T. Materials Science Aspects Relevant for High-Temperature Electrochemistry. Solid State Electrochemistry II: Wiley-VCH Verlag GmbH & Co. KGaA; 2011. p. 415-65.
[33] Crank J. The mathematics of diffusion / by J. Crank. Oxford [England]: Clarendon Press; 1975.
[34] Mokkelbost T, Andersen Ø, Strøm RA, Wiik K, Grande T, Einarsrud M-A. High-Temperature Proton-Conducting LaNbO4-Based Materials: Powder Synthesis by Spray Pyrolysis. J Am Ceram Soc. 2007;90:3395-400.
[35] Lohne ØF, Søgaard M, Wiik K. The Significance of Gas-Phase Mass Transport in Assessment of kchem and Dchem. J Electrochem Soc. 2013;160:F1282-F92.
[36] den Otter MW, van der Haar LM, Bouwmeester HJM. Numerical evaluation of eigenvalues of the sheet diffusion problem in the surface/diffusion mixed regime. Solid State Ionics. 2000;134:259-64.
[37] Gopalakrishnan J, Colsmann G, Reuter B. Studies on the La2−xSrxNiO4 ($0 \leqslant x \leqslant 1$) system. J Solid State Chem. 1977;22:145-9.
[38] Bassat JM, Odier P, Villesuzanne A, Marin C, Pouchard M. Anisotropic ionic transport properties in La2NiO4+δ single crystals. Solid State Ionics. 2004;167:341-7.
[39] Jeon S-Y, Choi M-B, Hwang J-H, Wachsman ED, Song S-J. Electrical Conductivity and Thermoelectric Power of La2NiO4+δ. J Electrochem Soc. 2011;158:B476-B80.
[40] Syvertsen GE, Wiik K. Student project. DMSE. Trondheim, Norway: Norwegian University of Science and Technology - NTNU; 2011.
[41] Li Z, Haugsrud R. Effects of surface coatings on the determination of Dchem and kchem in La2NiO4+δ by conductivity relaxation. Solid State Ionics. 2012;206:67-71.
[42] Minervini L, Grimes RW, Kilner JA, Sickafus KE. Oxygen migration in LaNiO. J Mater Chem. 2000;10:2349-54.
[43] Bassat JM, Odier P, Loup JP. The Semiconductor-to-Metal Transition in Question in La2-xNiO4+δ. J Solid State Chem. 1994;110:124-35.

[44] Wright JH, Virkar AV, Liu Q, Chen F. Electrical characterization and water sensitivity of Sr2Fe1.5Mo0.5O6−δ as a possible solid oxide fuel cell electrode. J Power Sources. 2013;237:13-8.
[45] Son LH, Phuc NX, Phuc PV, Hong NM, Hong LV. Observation of phase decomposition of Sr2FeMoO6 by Raman spectroscopy. Journal of Raman Spectroscopy. 2001;32:817-20.

4. EXPERIMENTAL AND MODELING OF YTTRIA STABILIZED ZIRCONIA SINTERING

ABSTRACT

To enhance the materials ionic conductivity, is desirable to manufacture the electrolyte using powders with small particle size and plan the sintering technique with the time-temperature profile to obtain fine-grained microstructures. There is absence of accurate models to predict the compacts density during sintering. Here a densification model was developed to predict densification, as a function of temperature, time and particle size. The model was able to predicting the achieved density using different sintering conditions. Sintering of powders leads to simultaneous densification and grain growth, particularly for nanocrystalline materials. Currently, methods such as spark plasma sintering (SPS), hot pressing (HP), two-step sintering (TSS) and fast firing (FF) are employed to hinder grain growth while maintaining a high densification. In this work, FF consisting in thermal treatments with high heating rates (>500º/min) and conventional sintering (RH) approaches were experimentally compared for yttria-stabilized zirconia (3YSZ and 8YSZ) compacts. Experiments were carried out in a tube furnace with a heating rate of ~500 °C/min (FF) and 10 °C/min (RH), analyzing the continuous density change and the grain size distribution of the dense structure. RH-samples present grain size bigger by a factor of ~4 and ~2 in comparison to raw powder for 8YSZ and 3YSZ respectively. Conversely, FF method completely suppresses grain growth at the experimental conditions with a growth factor of ~1 for both materials. Those results and comparison with previous work indicated that high heat inputs minimize grain growth.

Keywords: Fast Firing, 3YSZ, 8YSZ, Sinterization, Sintering Model.

4.1. INTRODUCTION

Sintering can be defined as a thermal treatment used to transform a powder compact into a continuous densify solid. Sintering is still the most important process in making bulk ceramics and metal by powder metallurgy [1]. However, it is difficult to predict the densification achieved. There is a lack of tools or relationships for accurately design the thermal cycles rate and operation temperatures. Thus, normally experiments are held for each material and particle size to establish and

optimize the densification. Another issue associated to sintering is that a thermal treatment also promotes grain growth, even at low temperatures for nano-particle materials [2]. Increases in the grain size degrades the product properties, therefore, it is necessary to select a appropriate sintering procedure in order to achieve a high densification, avoiding microstructure coarsening [3-6].

When crystalline powder particles join, the junction is a grain boundary. During and after sintering, some grains grow consuming others. This process is known as grain growth and is essentially an Ostwald ripening process [1].

Fine-grained materials constitute a paramount research focus, stem from their enhanced electrical [7-9], mechanical [4, 10], optical [11] and thermal [12] properties. However, morphology's control during sintering is challenging, due to overlapped thermally activated phenomena, i.e. grain growth and densification. In addition, when using starting powders below the micrometer particle size range, the temperature-time profiles are more critical, since shorter time is needed to reach a particular density at a given temperature as predicted by Herring's scaling law [13-15], and undesirable grain growth can arise even at low temperatures [2, 3].

Regardless the use of dopants, spark plasma sintering (SPS) [11, 16] and hot pressing (HP) [16, 17] are currently appropriate adopted techniques for production of nanostructured ceramics. Nevertheless, the equipment involved is expensive and complex, limiting its widespread application. Alternative routes as two-step sintering (TSS) [18] and fast firing (FF) [19] have been proposed, where the morphology control criterion lays on alter the temperature-time profile, to exploit the difference in kinetics between grain boundary (grain growth) and lattice diffusion (densification), making the latter predominant, with the advantage of feasible implementation in conventional furnaces [13, 18-21].

Harmer and Brook proposed fast firing (FF), which consist in use a very rapid heating rate and a short holding time at high temperatures to bypass temperature regions that do not contribute to densification and promote grain growth [19, 22].

FF serves to enhance the densification rate hindering coarsening rate, resulting in high densification and fine-grained microstructures, paramount importance in the sintering of nanostructured ceramic and composite materials and apply to other sintering techniques as microwave sintering [19, 21, 23].

Solid state sintering is typically separated into three stages: initial, intermediate and final. Figure 4.1 schematically portrays the standard densification curve of a compact over the stages throughout sintering time. The initial stage is characterized by the development of necks among particles and its contribution to compact shrinkage is limited to 2–3%. During the intermediate stage, densification up to 93% of the relative density, occurs before isolation of the pores. The final stage comprises densification from the isolated pore state to the final densification [24, 25].

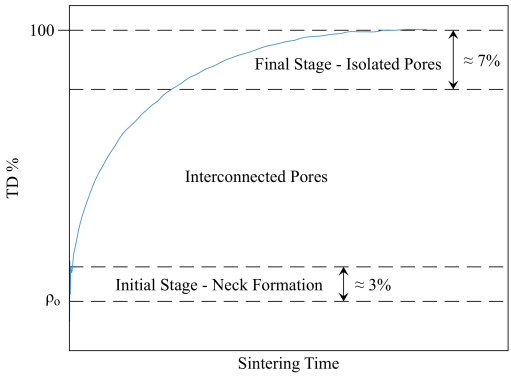

Fig. 4.1. Representation showing the densification curve of a powder compact and the three sintering stages. Adapted from [24].

For each stage, simplified models are typically used: the two-particle model for the initial stage, the channel pore model for the intermediate stage, and the isolated pore model for the final stage. Although all models ignore grain growth during sintering, the simplified geometries were considered for the sintering process to readily identify driving forces, mass transport paths, and geometric factors, but the

models practical applicability is restricted [5, 24-26]. Efforts made to extend the models have been of a limited success [26].

Another approach proposed by Su and Johnson [26], is the model of a master sintering curve (MSC) to characterize the sintering behavior of a given powder and green compact notwithstanding the heating profile [5, 26]. However, MSC approach presents the limitation of the powder particle size, as the apparent activation energy changes when comparing nanosized and microsized powder (Fig 4.2). Thus a new series of experiments must be conducted to describe the sintering behavior through this method, when the powder presents different particle size.

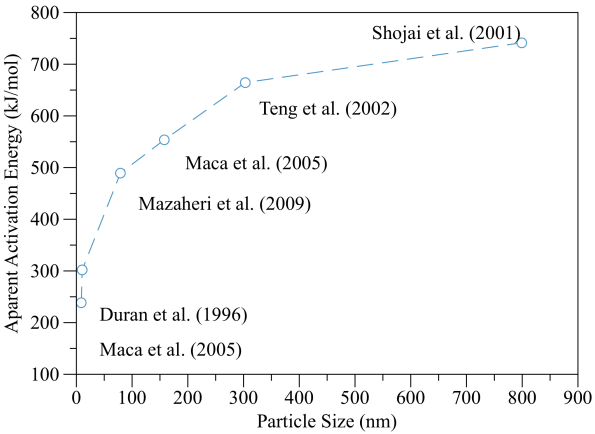

Fig 4.2. Activation Energy vs. Particle Size various authors [2, 5, 27, 28], adapted from [5] and references therein.

Another approach is the linear-viscous version of the Olevsky continuum theory of sintering; this provides the porosity kinetics during free sintering as [29, 30]:

$$\theta = \theta_0 e^{-\frac{3}{8}\tau_s} \tag{4.1}$$

where θ_0 is the initial porosity, θ is the porosity at any given time and τ_s is the specific dimensionless time of sintering, defined as:

$$\tau_s = 3\int_0^t \frac{\alpha}{\eta_0 G} dt \tag{4.2}$$

where t is the time of sintering: α the surface tension; η_0 the shear viscosity of the fully dense material; and G the average particle size. Thus, the porosity kinetics for free sintering is characterized by an exponential porosity decrease with an asymptotic approaching a fully dense state $\lim_{t\to\infty}\theta = 0$. If isothermal sintering conditions and negligible grain growth are assumed, all the parameters in Eq. (4.2) become time invariant and the integral can be numerically solved. Using Eq. (4.1) the specific time of sintering can be determined based on the dilatometry data for a given material through isothermal sintering experimentation as [31]:

$$\theta = \theta_0 e^{-\frac{9\alpha}{8\eta_0 G}t} \tag{4.3}$$

The drawback of this approach lies in the procedure of sintering itself. Normally an important part (in some cases more than 50%) of the densification occurs under non-isothermal conditions [2, 5], which make the relationship limited.

4.1.3. Chapter's Scope

The aim of this chapter was to analyze the sintering of ceramic materials in two simultaneous approaches. Firstly, fast firing was compared to conventional sintering in ceramic compacts of zirconia partially stabilized tetragonal phase (3YSZ) and the fully stabilized cubic phase (8YSZ). Secondly, a model was developed to predict the densification in powder compacts under different thermal cycles. The model intends to be more general and practical than the current approaches to serve as a tool for designing sintering schedules.

4.2. METHOD

4.2.1. Materials

Commercial, high purity yttria stabilized zirconia powders, ZrO_2 – 3 mol%Y_2O_3 powder (TZ-3Y-E) and ZrO_2–8 mol%Y_2O_3 (TZ-8Y) from Tosoh Co. (Tokyo, Japan) were used for the experiments. Particle size determination of the dispersion of the YSZ powders (0.5wt%) in de-

ionized water with dispersant were performed in a using Nano Zeta-sizer (ZEN 3600, Malvern). The mean particle size D_{50} is 188 nm and 342 nm for 3YSZ and 8YSZ respectively. The density and specific surface area of the powder, as reported by the supplier, is 6.05 and 5.95 g/cm3, respectively.

4.2.2. Experimental

Powders were compacted in a cylindrical die by uniaxial pressing (0.8kN) to produce green compacts with 19.05 mm diameter, and 0.5 and 2 mm height. No additives such as organic binders or dispersants were used to pellet forming. The green density was 45% of the theoretical density.

Sintering was performed in a tubular furnace (Thermolyne, F79335-70) using a heating rate of ~500 °C/min named FF (fast firing) and 10 °C/min named RH (ramp and hold conventional sintering) and cooled at ~500 °C/min. The maximum sintering temperature used was 1400 ºC and holding times of 1, 5, 10 and 100 min were used. The continuous density change of the YSZ compacts were measured in water using the Archimedes principle for 3 samples of each experimental condition.

SEM micrographs were use to analyze the grain sizes by image analysis, the micrographs in this part of the work were taken in a scanning electron microscope (SEM, Hitachi TM-3030). Voltage and magnification settings are visible in each micrograph. All samples previously coated with gold were placed on sample holders by tacky carbon tape.

4.3. RESULTS AND DISCUSSION

4.3.1. The Proposed Model of Densification

To extend to non-isothermal conditions in Eq. (4.1) and accurately fit on experimental isothermal data, here was proposed a phenomenological approach as:

$$\theta = \theta_0 e^{-F(T,t)} \tag{4.4}$$

where $F(T,t)$ is an unknown function depending on T and t, temperature and sintering time respectively. At isothermal conditions the sintering

process is a thermal activated process, thus, an Arrhenius type function is assumed. A power model for the sintering time was proposed to linearize the data. Thus, the isothermal function is set as:

$$F(t) = Ae^{-Q/RT}t^{1/n} \tag{4.5}$$

where A is a dimensionless preexponential factor which include the initial average grain size G_0 ($A=A'/G_0$ where A' is a material constant); Q the activation energy of the densification process; R is the gases constant (8.314 J/mol K); and n is a constant related with the sintering process. Taking natural logarithm both sides of Eq (4.5) for the isothermal case, Eq. (4.6) is obtained:

$$\ln\left(\frac{\theta}{\theta_0}\right) = Ae^{-Q/RT}t^{1/n} \tag{4.6}$$

To find n, a generalized reduced gradient algorithm was used to optimize the fitting on porosity isothermal data, maximizing the square root regression coefficient to Eq. (4.6) of the experimental data at different temperatures simultaneously. The results are shown in Fig. 4.3, where the coefficients for linear fit are in average >0.99. The outcome for both materials (3YSZ and 8YSZ) were similar with values of n_{3YSZ} = 2.375 n_{8YSZ} = 2.367.

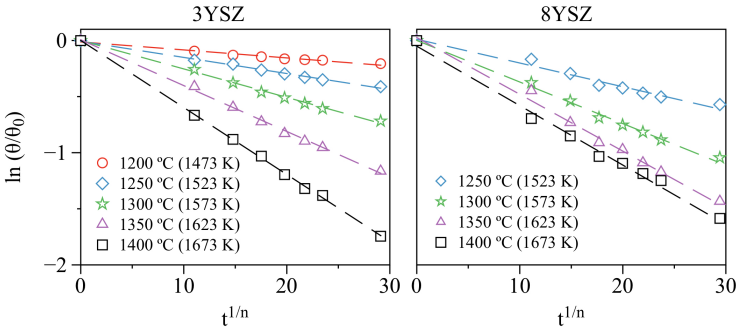

Fig 4.3. Isothermal sintering data for 3YSZ and 8YSZ with optimized fit. Eq. (4.6). n_{3YSZ} = 2.375 n_{8YSZ} = 2.367. Data from [32].

Thus, the slope (z) for each experiment, is function of the temperature as:

$$z = Ae^{-Q/RT} \tag{4.7}$$

The values of z are known from Fig 4.3. Taking natural logarithm in both sides of Eq. (4.7). Eq. (4.8) is obtained:

$$\ln z = \ln A - \frac{Q}{RT} \tag{4.8}$$

Now, it is possible to find the model parameters with a linear fitting of z vs 1/T showed in Fig. 4.4.

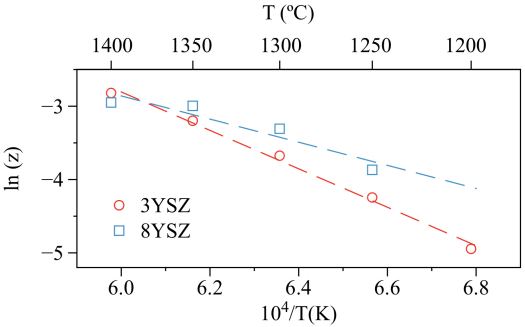

Fig 4.4. Slope from sintering z *vs.* 1/T data for 3YSZ and 8YSZ.

The fitting results in Fig 4.4 show that the proposed model describes the sintering from the data in [32], for a particle size of 600 nm and 530 nm for 3YSZ and 8YSZ respectively. The constants obtained for the studied materials are in Table 4.1.

Table 4.1. Parameters for the studied materials from model fit.

Parameter	**3YSZ**	**8YSZ**
A' (m)	2.45×10^{-1}	4.44×10^{-4}
Q (kJ/mol)	207.897	131.169
n	2.37	2.36

Up to now, the model parameters and the function works for isothermal evaluation. For the non-isothermal approach the function must be considered the sample thermal history. Fig 4.5 schematically depicts the sintering of a compact changing the temperature in each interval.

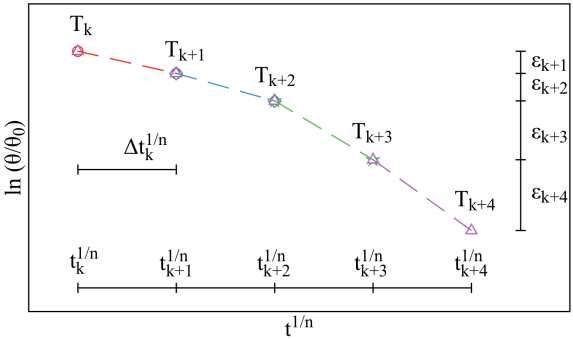

Fig 4.5. Schematic representation of the sintering phenomena.

The slope must change with every temperature change and accumulate the densification in each step. Analyzing the increments in Fig 4.5 the total interval is best described as:

$$\ln\left(\frac{\theta}{\theta_0}\right) = \varepsilon_{k+1} + \varepsilon_{k+2} + \varepsilon_{k+3} + \varepsilon_{k+4} = \varepsilon_{total} \tag{4.9}$$

where ε represent the interval step. The increment can be evaluated as:

$$\begin{aligned} \varepsilon_{total} &= \left(Ae^{-Q/RT_1}t_1^{1/n} - Ae^{-Q/RT_1}t_0^{1/n}\right) \\ &+\left(Ae^{-Q/RT_2}t_2^{1/n} - Ae^{-Q/RT_1}t_1^{1/n}\right)+ \\ &...+\left(Ae^{-Q/RT_j}t_j^{1/n} - Ae^{-Q/RT_j}t_{j-1}^{1/n}\right) \end{aligned} \tag{4.10}$$

where j is the total number of total steps. Generalizing Eq. (4.10) is possible to obtain:

$$\varepsilon_{total} = \sum_{k=1}^{j} Ae^{-Q/RT_k}(t_k^{1/n} - t_{k-1}^{1/n}) \tag{4.11}$$

where $\varepsilon_{total} = F(T,t)$ is the function that describe the non-isothermal behavior of the densification. Reorganizing the whole expression for the non-isothermal approach in Eq. (4.11), and replacing in Eq. (4.4), is obtained:

$$\theta = \theta_0 e^{-\sum_{k=1}^{j} \frac{A'}{G_0} \exp(-Q/RT_k)(t_k^{1/n} - t_{k-1}^{1/n})} \tag{4.12}$$

Making a variable change for time as:

$$\hat{t} = t^{1/n} \tag{4.13}$$

at time step constant for every k, and evaluating in the limit with change of time trend to zero, it is possible to obtain the continuous function as:

$$\theta = \theta_0 e^{-\int_0^{t^{1/n}} A \exp\left(\frac{Q}{R(HR)} \hat{t}^{-n}\right) d\hat{t}} = \theta_0 e^{\left[-\frac{A\left(\frac{Q}{R(HR)}\hat{t}^{-n}\right)^{1/n} \Gamma\left(-\frac{1}{n}, \frac{Q}{R(HR)}\hat{t}^{-n}\right)}{n} + c \right]_0^{t^{1/n}}} \tag{4.14}$$

where *HR* is the heating rate, *c* the integration constant and $\Gamma(a,x)$ is the incomplete gamma function that satisfies:

$$\Gamma(a,x) = \int_x^{\infty} t^{a-1} e^{-t}\, dt \tag{4.15}$$

The expression obtained in Eq. (4.14) is mathematically difficult to evaluate. However, the discrete version of the same equation, Eq. (4.12), is easy to compute. Since the relative density is related with the porosity with the relationship:

$$\theta = 1 - \rho_{rel} \tag{4.16}$$

Replacing Eq. (4.16) in (4.12), Eq. (4.17) is obtained:

$$\rho_{rel} = 1 - \theta_0 e^{-\sum_{k=1}^{j} \frac{A'}{G_0} \exp(-q/RT_k)(t_k^{1/n} - t_{k-1}^{1/n})} \quad (4.17)$$

This relationship is called here "*densification function*" for convenience. The relative density denotes the fraction between 0 and 1 of the material theoretical density.

4.3.2. Fast Firing

Fig. 4.6 shows the theoretical density achieved by 3YSZ and 8YSZ compacts as function of holding time at maximum temperature, for conventional sintering (RH) and fast firing (FF). An initial difference of ~30% in densification is observed at holding time 1 min. Such variance between methods, is attributed to the densification occurred during the heating procedure before reaching maximum temperature. The difference in density gets smaller with time, due to higher densification rate of FF samples at the holding temperature. The differences in relative density are negligible after holding time equal to 10 min.

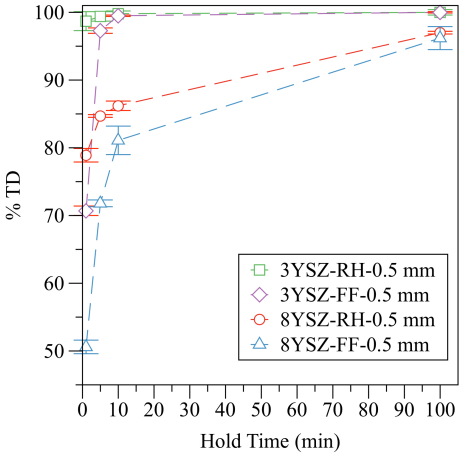

Fig 4.6. 3YSZ and 8YSZ density versus holding time at maximum temperature of 1400ºC. Compacts sintered by conventional sintering (RH) and fast firing (FF).

There is no evidence, whether one of the procedures encourages higher densities than the other, but evidently the FF procedure saves energy and time reaching similar results in density with higher heating rates, avoiding above 2 hours of sintering procedure.

Densification results of FF samples for the YSZ powders with different thickness (0.5 mm and 2 mm) are in Fig. 4.7. There are small differences in density for the 3YSZ. In previous work, while some authors report high densification through high heating rates [33], others report virtually no effect on the densification among different heating rates (2°-200°C min), and in addition, it is claimed that the application of high heating rates to powder compacts produces low densities caused by heat transfer problems [34].

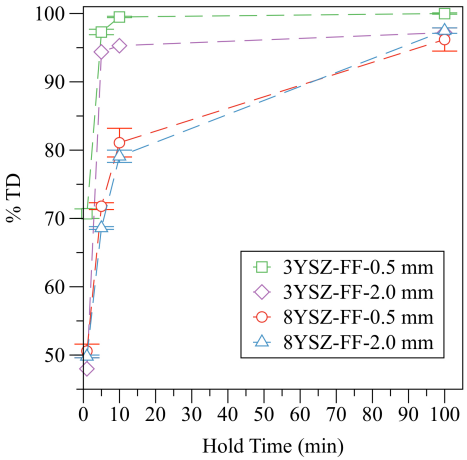

Fig 4.7. 3YSZ and 8YSZ density versus holding time at maximum temperature of 1400ºC. Compacts sintered by fast firing (FF) with different sample thickness (0.5, 2.0 mm).

The reported drawbacks are debatable, since the authors present a similar density detriment effect even at low rates as 5ºC/min. This effect can be instead due to pores separated from the grain boundary and irregular grain growth caused by heating schedules that promotes larger grain coarsening, probably by boundary migration velocity higher than

the pore migration velocity. The pores entrapped within grains cannot be eliminated by sintering or even by hot isostatic pressing [35]. Other reason for the residual porosity after sintering, can be due entrapped gas into the compacts during sintering, this effect disappear applying a calcination procedure [36].

The differences in density for the experiments presented here, might be attributed to entrapped gas, when more material-gas is available, more accentuated should be the effect. This is also supported by the experiments with 8YSZ that reflects negligible differences in the achieved density, where the available porosity presented in the samples at holding time 1 min, may let scape the remaining gas. However, the marginal effect presented in the experiments is not clarified by the micrographs.

Figs. 4.8 and 4.9 shows the SEM micrographs of 3YSZ after sintering under FF and RH sintering process (holding time 100 min). A reduction in grain growth was observed. The grain size distribution was measured from the micrographs by image analysis and the results together with the particle size distribution are in the Fig 4.10.

The grain size distribution of FF-3YSZ compacts is narrower and with an average 63% lower than the RH-3YSZ samples. The average values are 210 nm and 342 nm for FF and RH procedures respectively. The distribution of the powder is right-skewed with an average of 187.8 nm, for a growth factor of 1.11 and 1.82 for FF and RH respectively.

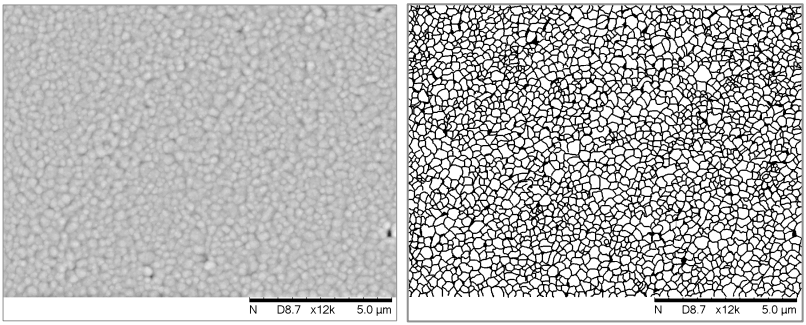

Fig 4.8. FF-3YSZ Sample, Holding Time 100 min.

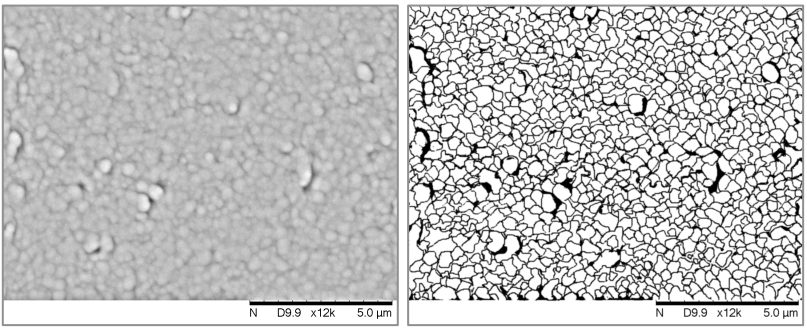

Fig 4.9. RH-3YSZ Sample, Holding Time 100 min.

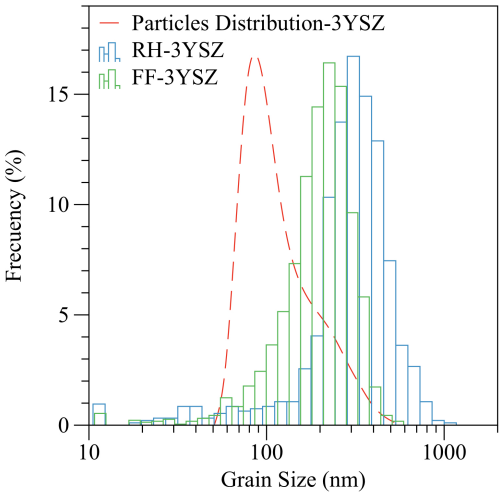

Fig 4.10. 3YSZ grain size distribution and average grain size for conventional and fast fired samples, holding time 100 mins.

Figs. 4.11 and 4.12 shows the SEM micrographs of 8YSZ after FF and RH sintering process (holding time 100 min). A reduction in grain growth was observed. The grain size distribution was measured from the micrographs by image analysis and the results together with the particle size distribution are shown in the Fig 4.13.

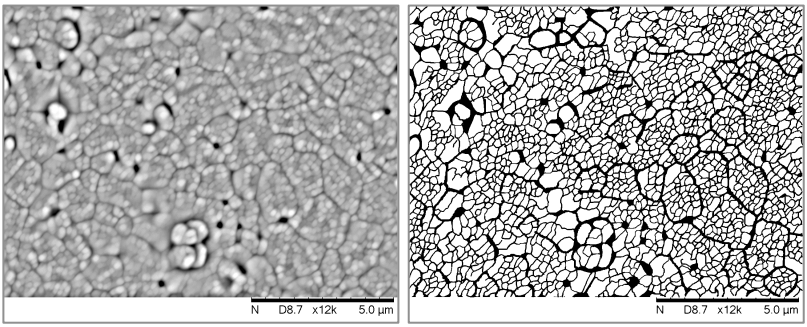

Fig 4.11. FF-8YSZ Sample, Holding Time 100 min.

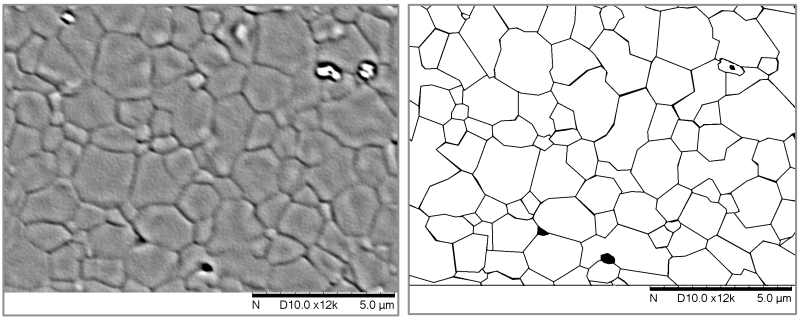

Fig 4.12. RH-8YSZ Sample, Holding Time 100 min.

The grain size distribution of FF-8YSZ compacts is narrower and with an average under one order of magnitude of difference comparing with RH-8YSZ samples. The average values are 243 nm and 1103 nm for FF and RH procedures, respectively. The normal distribution of the powder has an average of 342.2 nm.

The results of the distribution of the precursor powder and FF samples seem to be of the same order, which is contradictory. However, analyzing another samples it is clearer that are two orders of grain sizes (see Fig. 4.14), which reveals a grain coarsening restrain due to the high heating rate. This shows that the use of high heating rates, decrease the grain growth kinetics, regardless the holding time period. Hence, avoiding the earlier coarsening stages the fast firing sintering benefits persist even for longer holding times as 100 min, if the material is not fully dense.

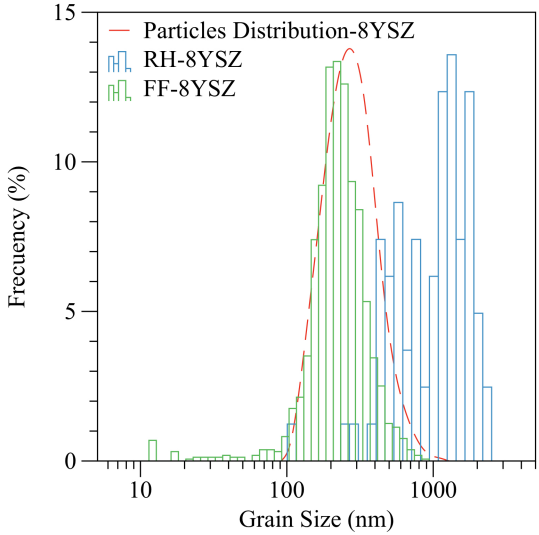

Fig 4.13. 8YSZ grain size distribution and average grain size for conventional and fast fired samples, holding time 100 mins.

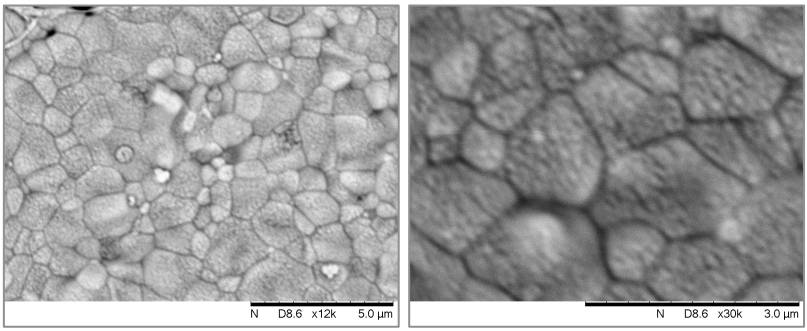

Fig 4.14. FF-8YSZ Sample, Holding Time 100 min.

The results indicate that high heating rates diminish the coarsening mechanism achieving high densities. Similar results were found in a previous work for nanosized 8YSZ experiments (24 nm), comparing low heating rate microwave sintering (5 ºC/min), high heating rate microwave sintering (50 ºC/min), conventional sintering (5 ºC/min) and two-step sintering (TSS) [3]. For heating rate of 5 ºC/ min no difference

was noticeable (Fig 4.15 a and b). For 50 ºC/min heating rate, the microstructural difference is evident on the micrograph in comparison with the 5 ºC/min schedules, with a difference factor of 3 on the grain size (Fig 4.15 c vs a, b). For TSS method the grain size is even smaller (Fig 4.15d). However, comparing the FF samples of the experiments presented here (Figs 4.11 and 4.14), the grain sizes are smaller with a submicrometer precursor 1200% bigger.

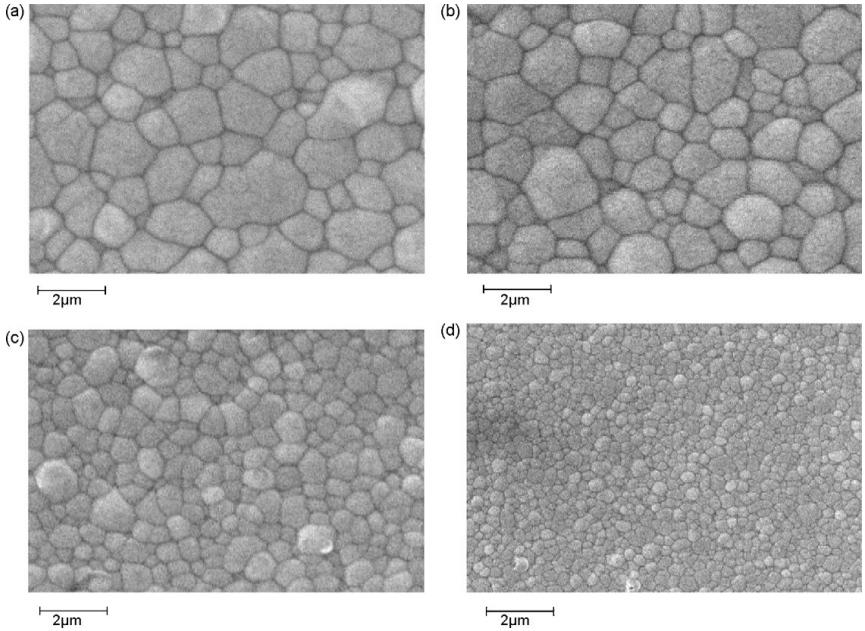

Fig 4.15. SEM micrographs of near full dense specimens sintered by (a) Conventional Sintering 5ºC/min, (b) Low Heating Rate Microwave Sintering 5ºC/min, (c) High Heating Rate Microwave Sintering 50ºC/min, (d) Two-Step Sintering method. Reproduced from [3].

Recall that the average grain size of the FF-8YSZ samples is 243 nm, from submicrometer raw particles with similar average value. The grain size values of 8YSZ-FF samples are in the order of typical sizes achieved from raw particles below 50 nm for the same material with different techniques; 295 nm (TSS), 210 nm (SPS), 370 (HP), [4, 16].

Overall results and the comparison with work on other techniques, shows that FF procedure is advantageous for grain growth suppress during sintering. This effect is less pronounced for 3YSZ samples as

expected, since 3YSZ is known to has slow grain growth kinetics. However, ~200 nm of grain size has been reported for conventional sintering under similar conditions, for powder compacts with 75 nm of particle size, showing that FF-3YSZ also yields comparable results as obtained with nanopowders [5].

As previously mentioned, TSS and FF methods are feasible in conventional furnaces with comparable results as more complex techniques as SPS and HP. In addition, FF and TSS have been reported for several materials offering a favorable method for bulk ceramics manufacture. Regarding the results and previous work, here is suggested a mixture of both methods TSS and FF; performing TSS with high heat inputs as FF method may surpass the results of current techniques.

4.3.2. Model Validation

The results of the densification function were compared with different sintering schedules for 3YSZ and 8YSZ; comparison among the experiments presented here and another founded in the literature. The results are presented in the Figs 4.16 to 4.18 for 3YSZ and Figs 4.19 and 4.20 for 8YSZ.

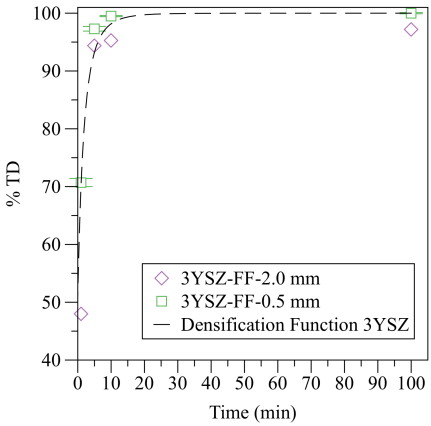

Fig 4.16. FF-3YSZ experiments. Precursor powder average particle size 188 nm. Heating rate 500ºC/min. Sintered by fast firing. The dashed line represents the densities predicted by the densification function. Maximum temperature 1400ºC, holding time shown on the graph.

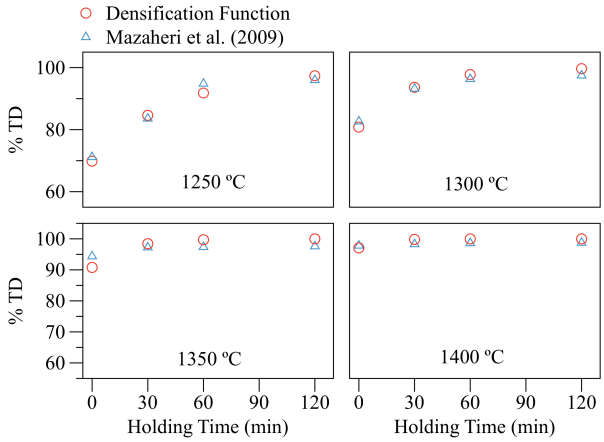

Fig 4.17. Material 3YSZ. Precursor powder average particle size 50 nm. Heating rate 5ºC/min. Sintered by conventional sintering. The densification function prediction is represented by circle symbols. Results reported by Mazaheri et al. (2009) [5], represented by triangle symbols. The maximum temperature and holding times are shown on the graph.

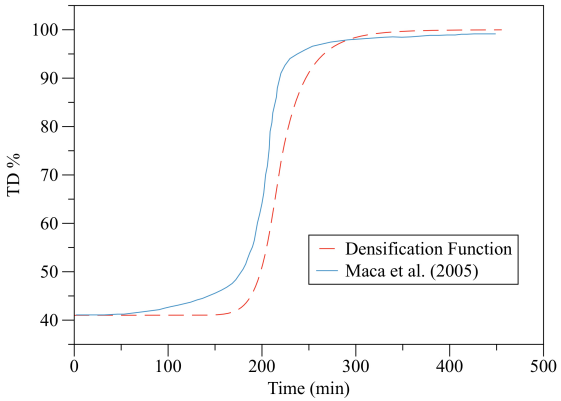

Fig 4.18. Material 3YSZ. Precursor powder average particle size 8 nm. Heating rate 5ºC/min. Sintered by conventional sintering. The dashed line represents the densification function prediction. Results reported by Maca et al. (2005) in [2], represented by the solid line. The maximum temperature is 1100ºC. Time also represent non-isothermal conditions.

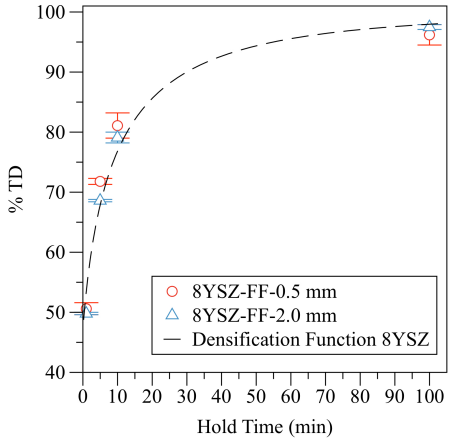

Fig 4.19. FF-8YSZ experiments. Precursor powder average particle size 342 nm. Heating rate 500ºC/min. Sintered by fast firing. The dashed line represents the densities predicted by the densification function. Maximum temperature 1400ºC, holding time shown on the graph.

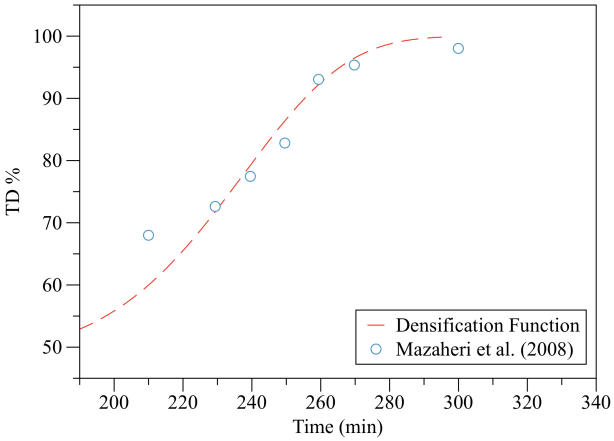

Fig 4.20. Material 3YSZ. Precursor powder average particle size 25 nm. Heating rate 5ºC/min. Sintered by conventional sintering. The dashed line represent the densification function prediction. Results reported by Mazaheri et al. (2008) [3], represented by circle symbols. The maximum temperature is 1500ºC. Time also represent non-isothermal conditions.

The densification function describes with an error of ± 3% the behavior of the materials even at different heating rates and different particle sizes on the higher density region. The highest error (for instance Fig 4.20 %TD<70) was found for the samples with nanosized particle precursors, on the initial schedule, where the densification is underestimated. This is attributed to the particle distribution. Since the model works with the average particle size, the smallest particles under the average size in the sample densify earlier giving an error. As the coarser particles larger than average densify later, and compensate the densification, achieving the values on the model.

4. CONCLUSION

This study examines the microstructure evolution compacts of yttria stabilized zirconia performed by different techniques, comparing fast firing with conventional sintering, and discussing previous work on other techniques employed in nanocrystalline solids. A model is also developed, validated and compared with other approaches.

Fast firing method saves energy and time in ceramic processing maintaining density values after sintering similar to those in conventional process. Fast firing promotes lower grain coarsening and narrower grain size distribution than conventional sintering and the results are comparable to nowadays widely adopted techniques as spark plasma sintering, hot pressing and two-step sintering.

The model developed, predict the densification on 3YSZ and 8YSZ compacts, describing times and temperatures for the high densification zone, for different particle sizes by means 3 experimental constants: This model may be a valuable tool to plan sintering schedules and optimize thermal cycles regardless the particle size of the material and seems more general than the mater sintering curve approach.

5. REFERENCES

[1] Carter CB, Norton G. Ceramic Materials: Science and Engineering: Springer; 2013.

[2] Maca K, Trunec M, Dobsak P. Bulk zirconia nanoceramics prepared by cold isostatic pressing and pressureless sintering. Reviews on Advanced Materials Science. 2005;10:84-8.

[3] Mazaheri M, Zahedi AM, Hejazi MM. Processing of nanocrystalline 8 mol% yttria-stabilized zirconia by conventional, microwave-assisted and two-step sintering. Materials Science and Engineering: A. 2008;492:261-7.
[4] Mazaheri M, Valefi M, Hesabi ZR, Sadrnezhaad SK. Two-step sintering of nanocrystalline 8Y2O3 stabilized ZrO2 synthesized by glycine nitrate process. Ceramics International. 2009;35:13-20.
[5] Mazaheri M, Simchi A, Dourandish M, Golestani-Fard F. Master sintering curves of a nanoscale 3Y-TZP powder compacts. Ceramics International. 2009;35:547-54.
[6] Chu M-Y, Rahaman MN, De Jonghe LC, Brook RJ. Effect of Heating Rate on Sintering and Coarsening. J Am Ceram Soc. 1991;74:1217-25.
[7] Bellino MG, Lamas DG, Walsoe de Reca NE. Preparation and ionic transport properties of YDC-YSZ nanocomposites. J Mater Chem. 2008;18:4537-42.
[8] Suzuki T, Kosacki I, Anderson HU. Microstructure–electrical conductivity relationships in nanocrystalline ceria thin films. Solid State Ionics. 2002;151:111-21.
[9] Han M, Tang X, Yin H, Peng S. Fabrication, microstructure and properties of a YSZ electrolyte for SOFCs. J Power Sources. 2007;165:757-63.
[10] Razavi Hesabi Z, Mazaheri M, Ebadzadeh T. Enhanced electrical conductivity of ultrafine-grained 8Y2O3 stabilized ZrO2 produced by two-step sintering technique. J Alloy Compd. 2010;494:362-5.
[11] Tran TB, Hayun S, Navrotsky A, Castro RHR. Transparent Nanocrystalline Pure and Ca-Doped MgO by Spark Plasma Sintering of Anhydrous Nanoparticles. J Am Ceram Soc. 2012;95:1185-8.
[12] Yang H-S, Bai GR, Thompson LJ, Eastman JA. Interfacial thermal resistance in nanocrystalline yttria-stabilized zirconia. Acta Materialia. 2002;50:2309-17.
[13] Esposito V, Traversa E. Design of Electroceramics for Solid Oxides Fuel Cell Applications: Playing with Ceria. J Am Ceram Soc. 2008;91:1037-51.
[14] Pereira GJ, Castro RHR, de Florio DZ, Muccillo ENS, Gouvêa D. Densification and electrical conductivity of fast fired manganese-doped ceria ceramics. Materials Letters. 2005;59:1195-9.
[15] Herring C. Effect of Change of Scale on Sintering Phenomena. Journal of Applied Physics. 1950;21:301-3.
[16] Dahl P, Kaus I, Zhao Z, Johnsson M, Nygren M, Wiik K, et al. Densification and properties of zirconia prepared by three different sintering techniques. Ceramics International. 2007;33:1603-10.
[17] Weibel A, Bouchet R, Denoyel R, Knauth P. Hot pressing of nanocrystalline TiO2 (anatase) ceramics with controlled microstructure. J Eur Ceram Soc. 2007;27:2641-6.

[18] Chen IW, Wang XH. Sintering dense nanocrystalline ceramics without final-stage grain growth. Nature. 2000;404:168-71.
[19] Harmer MP, Brook RJ. Fast Firing-Microstructural Benefits. Trans J Brit Ceram Soc. 1981;5:147-8.
[20] Chiang YM, Birnie DP, Kingery WD. Physical Ceramics: Principles for Ceramic Science and Engineering: Wiley; 1996.
[21] Garcia DE, Klein AN, Hotza D. Advanced ceramics with dense and fine-grained microstructures through fast firing. Reviews on Advanced Materials Science. 2012;30:273-81.
[22] Landin SM, Schulze WA. Rapid Sintering of Stoichiometric Zinc-Modified Lead Magnesium Niobate. J Am Ceram Soc. 1990;73:913-8.
[23] Menezes RR, Souto PM, Kiminami RHGA. Microwave fast sintering of submicrometer alumina. Materials Research. 2010;13:345-50.
[24] Kang S-JL. 4 - Initial Stage Sintering. In: Kang S-JL, editor. Sintering. Oxford: Butterworth-Heinemann; 2005. p. 39-55.
[25] Kang S-JL. 5 - Intermediate and Final Stage Sintering. In: Kang S-JL, editor. Sintering. Oxford: Butterworth-Heinemann; 2005. p. 57-87.
[26] Su H, Johnson DL. Master Sintering Curve: A Practical Approach to Sintering. J Am Ceram Soc. 1996;79:3211-7.
[27] Durán P, Villegas M, Capel F, Recio P, Moure C. Low-temperature sintering and microstructural development of nanocrystalline Y-TZP powders. J Eur Ceram Soc. 1996;16:945-52.
[28] Shojai F, Mantyla TA. Effect of sintering temperature and holding time on the properties of 3Y-ZrO2 microfiltration membranes. J Mater Sci. 2001;36:3437-46.
[29] Olevsky EA. Theory of sintering: from discrete to continuum. Materials Science and Engineering: R: Reports. 1998;23:41-100.
[30] Olevsky E, Molla TT, Frandsen HL, Bjørk R, Esposito V, Ni DW, et al. Sintering of Multilayered Porous Structures: Part I-Constitutive Models. J Am Ceram Soc. 2013;96:2657-65.
[31] Ni DW, Olevsky E, Esposito V, Molla TT, Foghmoes SPV, Bjørk R, et al. Sintering of Multilayered Porous Structures: Part II–Experiments and Model Applications. J Am Ceram Soc. 2013;96:2666-73.
[32] Suarez G, Rendtorff NM, Scian AN, Aglietti EF. Isothermal sintering kinetic of 3YTZ and 8YSZ: Cation diffusion. Ceramics International. 2013;39:261-8.
[33] Feng C, Qiu H, Guo J, Yan D, Schulze WA. Fast -Firing of Nanoscale Zr02 + 2.8 mol% Y2O3 Ceramic Powder Synthesized by the Sol-Gel Process. Journal of Materials Synthesis and Processing. 1995;3:5.
[34] Chen D-J, Mayo MJ. Rapid Rate Sintering of Nanocrystalline ZrO2−3 mol% Y2O3. J Am Ceram Soc. 1996;79:906-12.

[35] Kwon S-T, Kim D-Y, Kang T-K, Yoon DN. Effect of Sintering Temperature on the Densification of Al2O3. J Am Ceram Soc. 1987;70:C-69-C-70.
[36] Kim D-H, Kim CH. Entrapped Gas Effect in the Fast Firing of Yttria-Doped Zirconia. J Am Ceram Soc. 1992;75:716-8.

5. FINAL REMARKS

Reversible solid oxide fuel cells (RSOFC) were presented as a feasible alternative for energy storage using hydrogen as energy carrier. The current state of development of electrolyte, hydrogen and oxygen electrode materials has been reviewed in detail showing the potential of materials as Perovskites, Ruddlesden-Popper series and Double Perovskites, materials that have shown to have lower resistance, therefore, potentially more efficiency than the state-of-art oxygen electrode, lanthanum strontium manganite (LSM). A fine-grained microstructure can enhance key properties as ionic and electrical conductivity. RSOFCs technology has potential and the advancements in RSOFCs are growing by following the progress in SOFC/SOEC technology. However, it is required to address critical issues specific to the RSOFC.

Hydrogen and oxygen electrode performance and reversibility which mostly result in delamination of the oxygen electrode at high current densities, due to O_2 evolution reaction on the oxygen electrodes, which causes electrode structural and chemical changes.

Although it is indicated the possibility of stable operation of RSOFC at low currents, cells operating above 1 A.cm-2 show continuous degradation, which diminished decreasing cycle duration. However, switching and degradation mechanisms are not fully understood.

The stacks design, long-term tests and improvements are strongly focused on Ni/YSZ/(LSM or LSCF). Less attention has been dedicated to configurations regarding other materials with different structures, where key research features are scarce, as: degradation, stability and microstructural optimizations.

In addition, the development of novel materials and new processing techniques are required to overcome the known drawbacks and improve the performance and economic feasibility for further commercialization of RSOFC technology.

Novel Ruddlesden-Popper series as the system molybdenum-doped $La_{2-y}Sr_yNiO_{4+\delta}$ were developed. It shows solubility, however, the limit is rapidly reached by small amounts of Mo, limited by Sr-substitution. Single-phase $La_{1.8}Sr_{0.2}Ni_{0.95}Mo_{0.05}O_{4+\delta}$ was successfully synthetized. The lattice parameters; result of the Sr-Mo doping, has an elongated c-direction, increasing oxygen mobility in the a-plane. The electrical conductivity and transport properties of single-phase of $La_{1.8}Sr_{0.2}Ni_{0.95}Mo_{0.05}O_{4+\delta}$ were assessed by electrical conductivity

relaxation in the oxygen partial pressure range of 0.2 to 0.0066 atm at 600–900 ºC. The conductivity behaves p-type electronic on the studied range. Dependencies of electron-hole, oxygen interstitials, A-B-site doping and P_{O2} were explained by a simple defect model. Doping B-site with higher valence ions decrease the overall conductivity, but represents a favorable effect on ionic transport; the opposite effects by doping A-site with lower valence ions. Results disclose an enhancement on transport properties by partial substitution of nickel with molybdenum on the $La_{1.8}Sr_{0.2}NiO_{4+\delta}$. $La_2NiO_{4+\delta}$ surface exchange and bulk diffusion coefficients are surpassed at lower temperatures by $La_{1.8}Sr_{0.2}Ni_{0.95}Mo_{0.05}O_{4+\delta}$ transport data, with lower activation energy of both thermally activated processes D_{chem} and k_{chem}. $La_{1.8}Sr_{0.2}Ni_{0.95}Mo_{0.05}O_{4+\delta}$ presents instability in presence of oxygen and high temperature over time (>=600 ºC, 3 weeks), forming secondary phases, probably $SrMoO_4$ at the sample surface.

Fast firing method saves energy and time in ceramic processing maintaining density values after sintering similar to those in conventional process. Fast firing promotes lower grain coarsening and narrower grain size distribution than conventional sintering and the results are comparable to nowadays widely adopted techniques as spark plasma sintering, hot pressing and two-step sintering.

The developed model predicts the densification on 3YSZ and 8YSZ compacts, and describes times and temperatures for the high densification zone with different particle sizes by means 3 experimental constants: This model may be a valuable tool to plan sintering schedules and optimize thermal cycles regardless of the particle size of the material and seems more general than the mater sintering curve approach.